Atmospheric Boundary Layer Impacts on Wind Farms

Jonathan Stephen Pennells

School of Earth and Environment

University of Leeds

Submitted in accordance with the requirements for the degree of

Doctor of Philosophy

March 2018

Declaration of Authorship

The candidate confirms that the work submitted is his and that appropriate credit has been given where reference has been made to the work of others.

The copy has been supplied on the understanding that it is copyright material and that no quotation from the thesis may be published without proper acknowledgement.

Acknowledgements

I would firstly like to thank Andrew Ross. As my primary supervisor, he has provided valuable academic support throughout the last four years. The majority of my contact has been with Andrew and he was always there to provide guidance when lines of enquiry fell short of their expectations. I would also like to thank Andrew for suggesting and encouraging me to take on additional roles during this process. A thank you must also be given to my secondary supervisors Simon Vosper and Ian Brooks.

A mention must also be given to the presenters of Chatmosphere, especially in the early years of my time in ICAS. It was from those people that I learnt a wider understanding of meteorological processes, giving context to the literature. Peer support has been crucial during that process and for that I thank the regular attendees of ICAS coffee. A special mention goes to Tom, Tim, Kamalika and Stewart who have shared this experience with me.

I would also like the thank my close friend Tom who has been my verbal stress ball during this process. Personally, I would like to thank my wife Emma and daughter Matilda. Emma has supported me for the entirety of this process, from the decision to apply to now. On many an occasion I have enlisted her list making skills to help with the challenge at the time. Without their support I would not have got to the end of this process.

Abstract

Increasing demand for renewable energy sources has meant that wind power is becoming a more crucial source of energy, leading to larger wind farms. It is currently unknown whether wind farms impact the boundary layer. This thesis aims to improve our understanding of the impact from wind farms. To do this, numerical simulations are carried out in BLASIUS and WRF with an existing Wind Farm Parametrisation (WFP) being implemented in BLASIUS. Neutral boundary layer simulations are carried out in BLASIUS, with different velocities, height and capping inversion strengths. It is found that decreases in boundary layer height increase the impact from the wind farm, where the height is between 715 m and 992 m for turbines with a hub height of 95 m. Increases in velocity increase the vertical advection of horizontal momentum upstream of the turbines and greater deceleration of momentum in the wind farm. Non-dimensional analysis found jumps in the inversion layer above the wind farm for $Fr < 1$, and increases in the pressure perturbations for low Z flows. Comparisons are made between BLASIUS and a linear model for wind farms in neutral boundary layers. The drag term in the linear model is overestimated and should be modified to account for the logarithmic velocity profile near the surface. The assumptions made in the linear model do not inhibit its representation of the velocity and pressure perturbations within the boundary layer. The impact of a wind farm on a sea breeze is investigated using WRF simulations. It is found that a wind farm at the coast does not impact the propagation of the sea breeze but does impact the land breeze. This is due to the turbulent boundary layer which the wake is in, causing a fast decay of the wake. The land breeze propagates through the wind farms and is directly impacted.

Abbreviations

ARW	Advanced Research WRF
BLASIUS	Boundary Layer Above Stationary, Inhomogeneous Uneven Surface
CWEX	Crop Wind Energy Experiment
LES	Large Eddy Simulations
LIDAR	Light Detection and Ranging
RANS	Reynolds Averaged Navier-Stokes
RRMT	Rapid and Radiative Transfer Model
SAR	Synthetic Aperture Radar
TKE	Turbulent Kinetic Energy
VD	Velocity Deficit
WFP	Wind Farm Parametrisation
WRF	Weather, Research and Forecast

Contents

List of Figures

List of Tables

Chapter 1

Introduction

In recent years, the reliance on fossil fuels has been scrutinised, leading to an increase in the demand for energy derived from renewable sources. Wind power has played a significant part in reducing our need for non-renewable energy and wind power will play a major role in further increasing our renewable energy sources.

Within the European Union, wind power accounts for a third of all electricity from renewable sources (COMM, 2017). Of all renewable energy sources, wind power has seen the greatest increase in recent years, increasing four fold in the years 2004 to 2015 (COMM, 2017), with an increase of 13.8% from 2014 to 2015. These statistics combine onshore and offshore wind power and a large contributor to these increases has been the onshore wind farms. From an economical stance, onshore have had many advantages over offshore wind turbines, although recent investment in offshore has brought production cost down (Arwas *et al.*, 2012). Offshore wind energy increased ten times between 2009 and 2015 in the EU from 352 ktoe to 3,783 ktoe (Öko-Institut, 2017).

Renewable energy projections see wind energy becoming a more important energy source within the EU. Wind energy projections produced by the European Wind Energy Association estimate that by the year 2030, 320 GW of power will come from wind, double the 2014 wind power total of 129 GW (Öko-Institut, 2017). To meet these targets, there will need to be an increase in wind farms, with a large proportion coming from offshore wind farms (Öko-Institut, 2017). Although many

effects are considered before the deployment of a wind farm, such as ecological and environmental, their impact on the atmosphere remains unknown.

On 8th February 2008, the rare spectacle of wind farm wake clouds were photographed in the Horns Rev wind farm (Emeis, 2010). The Horns Rev wind farm is located between 14 km and 20 km off the coast of Jutland in Denmark. The Horns Rev wind farm is an 80 turbine wind farm, arranged in an 8×10 grid, with each row of 10 turbines on the east-west axis. The formation of the wind turbine wake clouds has been summarised in Emeis (2010). On the day the photograph was taken, there was an approximately $5\,\mathrm{m\,s^{-1}}$ south-easterly wind over the Horns Rev wind farm. According to radiosonde profiles, this advocated cool saturated air of 1.5°C. Meteorological measurements at the Horns Rev wind farm show that the air around the wind farm was warmer at approximately 5°C, and also saturated. The boundary between these two layer was in and around the bottom of the turbine blades, with the rotation from the turbines mixing the two layers of air. The result of mixing two saturated layers of air of different temperatures is condensation and hence the wind turbine wake clouds occur.

The occurrence of wind turbine wake clouds bring to life the normally invisible effect that wind turbines are having on their surrounding atmosphere, and raises questions as to their wider impact. This work aims to improve our understanding of the impact that wind farms have on their surrounding atmosphere. To do this, idealised numerical simulations of wind turbines will be used to understand the dynamical impact on the boundary layer and test whether wind farms are likely to impact local meteorology.

Chapter 2 gives an overview of the literature on wind farms and what is known about their impact. Beginning with a general summary of boundary layer theory, this chapter looks at the dynamics associated with both individual wind turbines and groups of turbines in wind farms. A range of observational data, wind tunnel measurements and numerical modelling studies are used, ranging from small scale turbulence around the wind turbine blades to studies which look at the impact of wind farms on climate.

The numerical models used in this study are summarised in chapter 3. This includes the Met Office Boundary Layer Above Stationary, Inhomogeneous Uneven Surface (BLASIUS) model and the Weather, Research and Forecast (WRF)

model. Included in this chapter is a description of the Wind Farm Parametrisation (WFP) used in both of these models and an investigation into the sensitivity of the parametrisation.

The impact of a wind farm in a Reynolds Averaged Navier-Stokes (RANS) model is investigated in chapter 4. This chapter aims to: (1) Investigate how wind farm wakes are affected by different boundary layer structures, (2) Determine the key dynamics which change the impact of a wind farm on the boundary layer and (3) Observe how wind farm impacts on the boundary layer change with different sized wind farms.

Chapter 5 makes a comparison between the BLASIUS WFP from chapter 4 and a simplistic linear model of wind farms in a boundary layer. Different boundary layer profiles are studied to assess the validity of the linear model. The phenomenon of wind farm stalling, whereby the velocity in the wind farm reduces sufficiently that down stream wind turbine can no longer operate, is investigated.

The impact of a wind farm in a meteorological phenomenon is investigated in chapter 6. This chapter looks at the impact of a wind farm on a simulated sea breeze and land breeze. Idealised numerical simulations are once again used, with wind farms of differing turbine density being the area of interest, to see what the likely impact is of a wind farm in a more realistic setting.

The final chapter gives a summary of the work in this study and suggests additional areas which could be investigated.

Chapter 2

Literature Review

2.1 The Atmospheric Boundary Layer

The Earth's atmosphere is split into multiple characteristic layers, each with different defining properties. The lowest layer of the atmosphere is the troposphere. The troposphere typically extends up to approximately 11 km (Stull, 1988) and due to adiabatic cooling, is characterised by temperature decreases with height. The interaction of the troposphere with the Earth's surface causes the formation of a boundary layer. The extent of the atmospheric boundary layer varies in magnitude, ranging between 100 m to 3000 m (Stull, 1988), with the interaction with the Earth surface impacting the flow dynamics of the boundary layer.

The atmospheric boundary layer can be divided into multiple sections, with each layer increasing in height above the Earth's surface. The lowest 10 % of the boundary layer is classed as the surface layer, where wind shear and turbulent fluxes deviate by no more than 10 % of the mean values (Stull, 1988, p.10). Above the surface layer sits the mixed layer. This is the dominant layer in the boundary layer and features nearly constant potential temperature with height. Small fluctuations to the mixed layer have a short time-scale due to the limited buoyancy force. At the top of the boundary layer there is a stable layer of air, referred to as an inversion layer. The inversion layer restricts the continual increase of the mixed layer. These layers can be seen in a schematic of the boundary layer in figure 2.1. In 2.1, potential temperature is used. This is a

useful metric to use as potential temperature is a conserved quantity with height and at pressure p is defined as

$$\theta = \mathrm{T}\frac{p_0}{p}^{R/c_p} \tag{2.1}$$

where T is the absolute temperature, p_0 is a reference pressure, R is the gas constant and c_p is the specific heat capacity of air at a constant pressure.

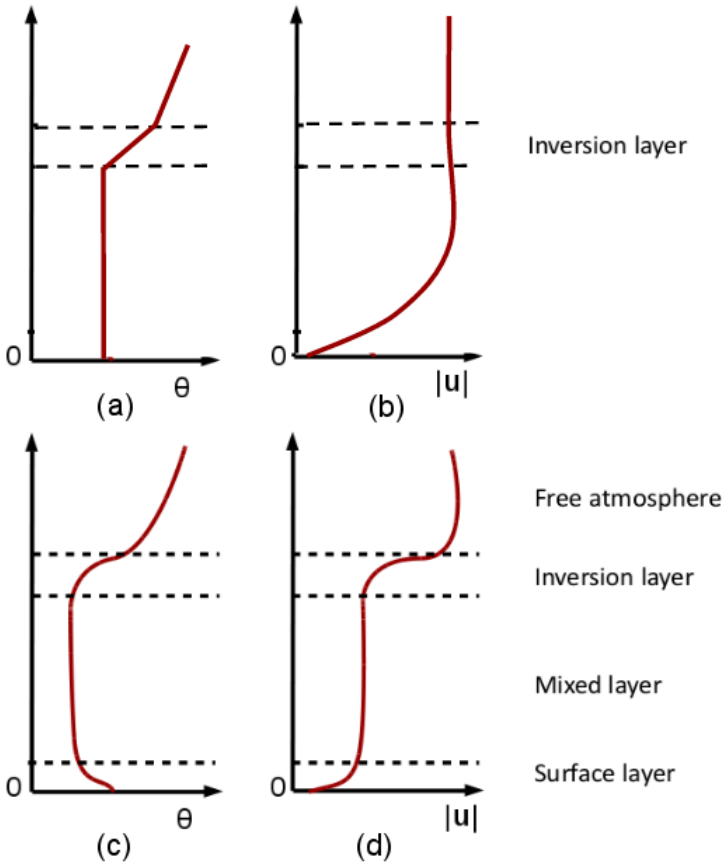

Figure 2.1: *Boundary layer profile of both potential temperature θ and wind speed $|\mathbf{u}| = \sqrt{u^2 + v^2 + w^2}$. A neutral potential temperature profile is shown in (a), with the velocity profile for a neutral boundary layer shown in (b). A convective potential temperature profile is shown in (c) with the velocity profile for a convective boundary layer shown in (d).*

As a parcel of air from the surface rises it cools at an adiabatic lapse rate (this can either be the dry adiabatic lapse rate or wet adiabatic lapse rate). This study only focusses on dry boundary layers. If the surroundings are cooler than

the air parcel then the air is said to be unstable. When the air temperature is warmer than the air parcel temperature then the air is stable. If the parcel rises through air of the same temperature then the boundary layer is said to be neutral, shown in figure 2.1(a). In a neutral boundary layer, the velocity profile is controlled by the friction at the surface and the geostrophic wind speed in the free atmosphere, as shown in figure 2.1(b). Potential temperature is used as an indicator of stability. Increasing θ with height indicates stable, decreasing θ with height means unstable and equal θ with height shows a neutral layer.

The boundary layer can be broken down into additional layers, each with different stability characteristics. Figures 2.1(c) and (d) show the potential temperature and velocity profile in a convective boundary layer, typical of the day time boundary layer. Near the surface, a warm layer is created due to surface heating. This is known as the surface layer and is associated by high turbulence from the surface friction and thermal eddies. Above this is the mixed layer, which is largely caused by the convection of thermal eddies from the surface layer. Above the mixed layer is a small stable layer, known as an inversion layer. This layer acts as an entrainment layer, restraining the growth of turbulence from the mixed layer. The boundary layer grows from the entrainment of less turbulent air above the mixed layer.

2.1.1 Reynolds averaged Navier-Stokes equations

In order to model the atmospheric boundary layer, approximations to the Navier-Stokes equations are used. These assumptions enable the Navier-Stokes equations to be simplified and hence become more mathematically pliable. The continuity equation 2.2 can be reduced to the incompressibility equation 2.3 with the assumption that time dependent density changes are of a smaller magnitude than spatial velocity deviations. This is a valid assumption to make for the atmospheric boundary layer (Stull, 1988).

$$\frac{\mathrm{d}\rho}{\mathrm{d}t} + \rho\frac{\partial u_i}{\partial x_i} = 0 \tag{2.2}$$

$$\frac{\partial u_i}{\partial x_i} = 0 \tag{2.3}$$

Equation 2.3 is also referred to as mass conservation. This is a useful property in explaining acceleration and deceleration of flow in the boundary layer, where the boundary layer height is changed due to dynamical processes. From Newton's second law the conservation of momentum equation is

$$\frac{\partial u_i}{\partial t} + u_j \frac{\partial u_i}{\partial x_j} = -\delta_{i3} g + f \epsilon_{ij3} u_j - \frac{1}{\rho} \frac{\partial p}{\partial x_i} + \nu \frac{\partial^2 u_i}{\partial x_j^2}. \tag{2.4}$$

Equation 2.4 is displayed in index notation where $\delta_{ij} = 1 \iff i = j$, otherwise $\delta_{ij} = 0$, and ϵ_{ij3} is the alternating tensor. The velocity vector is given by $\mathbf{u} = (u_1, u_2, u_3) = (u, v, w)$, ρ is the fluid density, p is the pressure term, g is the gravity scaler and ν is the kinematic viscosity. Starting from the left hand side of equation 2.4 we have the inertia term of the fluid momentum, advection, gravity in the vertical direction, Coriolis effects, the fluid's pressure gradient and finally viscous stresses. A useful technique for simplifying equation 2.4 is that of Reynolds averaging. This assumes that each flow variable can be described by a mean term plus a turbulent term, such as $u_i = \bar{u}_i + u_i'$. This is an appropriate assumption for the boundary layer as the well mixed nature of the flow implies that turbulent eddies have a fast decay rate, reducing the flow back to its mean state. Reynolds averaging looks at the time-averaged boundary layer flow. The Reynolds averaged boundary layer variables are therefore of the form $\bar{u}_i = \overline{\bar{u}_i + u_i'} = \bar{u}_i + \overline{u'}$. This implies that $\overline{u'} = 0$. Carrying out Reynolds averaging to equation 2.4 leads to

$$\frac{\partial \bar{u}_i}{\partial t} + \bar{u}_j \frac{\partial \bar{u}_i}{\partial x_j} = -\delta_{13} g + f \epsilon_{ij3} \bar{u}_j - \frac{1}{\bar{\rho}} \frac{\partial \bar{p}}{\partial x_i} + \nu \frac{\partial^2 \bar{u}_i}{\partial x_j^2} - \frac{1}{\rho} \left(\frac{\partial \tau_{ij}^{Rey}}{\partial x_j} \right). \tag{2.5}$$

The non-linear advection terms lead to the inclusion of the Reynolds stress $\tau_{ij}^{Rey} \equiv -\rho \overline{u_i' u_j'}$. The Reynolds stress represents the deformation of flow parcels as a result of turbulent eddies. The kinematic stress term $\nu(\partial^2 \bar{u}_i)/(\partial x_j^2)$ can be neglected for high Reynolds number flow where $Re = VL/\nu \gg 1$. Here V and L are the velocity scales and length scales of the flow.

2.1.2 Velocity profiles

As previously stated, the interaction of the boundary layer flow with the Earth's surface is a crucial dynamic of the boundary layer. In order to mathematically

model this impact, the surface friction velocity (u^*) is defined, where

$$u_*^2 = \left(\overline{u'w'}_s^2 + \overline{v'w'}_s^2\right)^{1/2} = \frac{1}{\rho}\left|\tau^{Rey}\right|. \tag{2.6}$$

We can see that the friction velocity is represented in terms of the flow Reynolds stress vector τ^{Rey} at the surface. In a neutral, homogeneous boundary layer, the the velocity increases with height from the surface according to the logarithmic profile. This occurs in the surface layer and is calculated as

$$u(z) = \frac{u^*}{\kappa}\ln\left(\frac{z}{z_0}\right) \tag{2.7}$$

where $\kappa = 0.04$ is the von Karman constant and z_0 is an aerodynamic roughness length. The latter can be empirically calculated from velocity observations. The logarithmic velocity profile within the surface layer is an important feature in the study of wind farms. The rotor area from a wind turbine is usually located within this layer and thus the velocity changes throughout the extent of the turbines.

2.2 Wind turbine description

All the work in this study will focus on horizontal axis wind turbines. These will be referenced as individual turbines or part of wind farm arrays, both onshore and offshore. There are a few key features of a wind turbine which will be used throughout.

There are two key measurements associated with a turbine: hub height and rotor diameter. As the name suggest, the hub height is the height above the ground of the hub, or nacelle, which contains the generator components of the turbine. The nacelle is positioned on top of the tower and determines the height of the wind turbine. Attached to the nacelle are the rotating blades. The nacelle contains a yaw mechanism which rotates the hub on the vertical axis, keeping the turbine blades aligned with the mean wind.

The power output from a turbine is dependent on the specific turbine and mean wind speed. Figure 2.2 shows a schematic of the power curve associated with a turbine. The blades require a minimal wind speed in order to rotate. This is

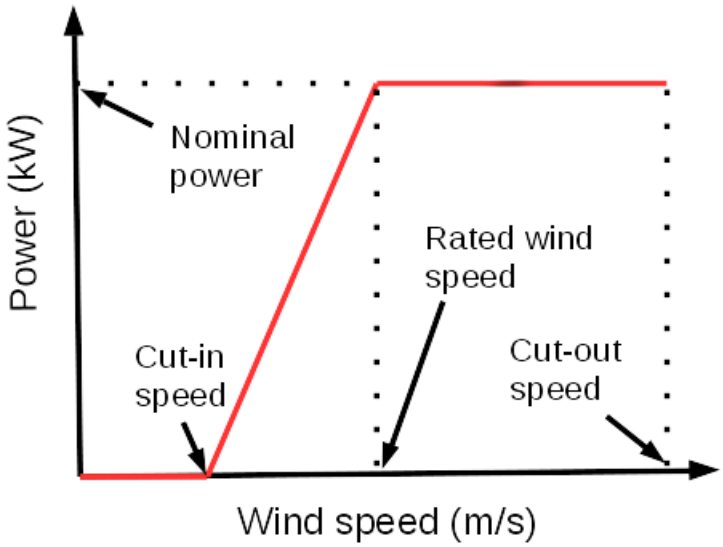

Figure 2.2: *Plot showing the changes to the turbine power as the wind speed changes. The power from the turbine is shown as the red line with the cut-in, cut-out and rated wind speed highlighted along with the nominal power.*

called the cut-in speed. Above the cut-in speed, the gearing within the hub with convert the kinetic energy from the wind into usable electrical energy. There will be an increase in the power output as the wind speed increases, until the rated wind speed is reached. This is the wind speed where the nominal power of the turbine is output, i.e. the maximum power which can be output from the turbine. Above the rated wind speed, there are no further increases in output power. There always exists a cut-out speed. This is the wind speed where an automatic brake is applied within the turbine, stopping the rotating blades. This is due to the forces which occur within the turbine at higher wind speeds, which will be above the tolerances of that turbine.

The specifics of these values differ between each turbine. The efficiency of a turbine changes with wind speed, although the details are commercially sensitive. This makes the modelling of real turbines difficult as it requires information from wind turbine manufacturers.

2.3 Methods of analysing wind turbine wake dynamics and their impacts

In this section we explore the various methods of measuring wind turbine wakes from both single turbines and turbine arrays. The techniques described are used for a range of atmospheric scales, from turbulent eddies within wind turbine wakes to their impact on local meteorology.

2.3.1 Field measurements and remote sensing

The most direct method of measuring wind turbine wakes is with field measurements. This is mainly carried out by using satellite data and lidar measurements which look at the impacts of wind turbine wakes.

Satellite data have been used in multiple studies primarily with the focus of looking at surface temperature changes. Zhou *et al.* (2012) used Moderate Resolution Imaging Spectroratiometer (MODIS) to analyse the change in land surface temperature (LST) over a region in Texas occupied by wind turbines. The outcome from this study can be seen in section 2.5.1. Wind speed changes over the sea can also be determined from satellite data, namely Synthetic Aperture Radar (SAR), a method used in Christiansen & Hasager (2005).

Another technique employed in the study of wind turbine wakes is Light Detection and Ranging (LIDAR). LIDAR's work by emitting a pulse of light at a predetermined wavelength along a beam. The scattering of the light is then measured by sensors within the LIDAR, which can be used to calculate the wind speed of the fluid along the beam. Most LIDAR measurements takes place with a surface LIDAR however more recent studies use nacelle position LIDAR's (Machefaux *et al.*, 2015; Wagner *et al.*, 2014). Nacelle mounted LIDARs have the advantage of producing a detailed analysis of the velocity changes within a wind turbine wake compared to the velocity upstream of the turbine. Unfortunately, this is sensitive information from the wind turbine manufacturer's perspective and hence in studies with a nacelle mounted LIDAR there is little information as to the exact location of the study and the type of turbine used.

In some studies, large field campaigns have been carried out employing multiple measurement methods (Rajewski *et al.*, 2014; Vanderwende & Lundquist, 2016).

In addition to LIDARs, there are meteorological masts to measure the surrounding meteorological conditions both inside and outside of wind turbine arrays. Flux measurements have also been used to assess changes in heat, H_2O and CO_2 fluxes (Rajewski *et al.*, 2014).

2.3.2 Wind tunnel

Wind tunnels are another useful method for assessing wind turbine wakes. The specific details of each wind tunnel experiment are different, however they all use miniature wind turbines with rotating blades in a simulated atmospheric boundary layer. The turbines occupy the lowest portion of the boundary layer with the rotors confined to the lowest 1/3 of the boundary layer. Wind tunnel experiments provide useful information as to the change in turbine wakes for different stability profiles. By controlling the temperature gradient between the surface and air temperatures, neutral (Chamorro & Porté-Agel, 2011), stable (Chamorro & Porte-Agel, 2010) and convective (Zhang *et al.*, 2013) boundary layers can be simulated. In addition to the effects of stability, wind tunnel experiments provide useful information as to the effect from changing a wind turbine array structure. Turbulent boundary layers can also be generated by a tripping mechanism, as used in Chamorro & Porte-Agel (2010); Chamorro & Porté-Agel (2009); Chamorro *et al.* (2011, 2012) The two main structures that are used in wind tunnel investigations (and numerical simulations) are aligned wind turbines and staggered turbine arrays (Chamorro & Porté-Agel, 2011). A limitation to wind tunnel simulations is their scaling issues with respect to Reynolds number. Chamorro *et al.* (2011) investigated the sensitivity of wind turbine wakes to Reynolds number, $Re = \bar{u}_h D/\nu$, where $\bar{u}_h$ is the hub height wind speed, D is the rotor diameter and ν is the kinematic viscosity. Using a range of boundary layer conditions, with $Re \approx 1.66 \times 10^4 - 1.73 \times 10^5$ it was found that the velocity deficit within the turbine wake converges for $Re > 4.8 \times 10^4$ and that the near wake was more sensitive to changes in Re. This is due to the turbine blades generating small eddies within the near wake region. Using wind tunnel data is therefore an appropriate tool for the analysis of wind turbine wakes, however caution must be used when quantitatively interpreting near wake impacts.

2.3.3 Numerical models

The most prevalent methodology for studying wind turbine wakes is with numerical models. There are two types of numerical models: the first uses Reynolds averaged Navier-Stokes equations (RANS) and the second are large eddy simulations (LES). LES have been used extensively to study the formation and evolution of wind turbine wakes (Abkar & Porte-Agel, 2015; Allaerts & Meyers, 2015; Calaf *et al.*, 2010, 2014; Wu & Porté-Agel, 2012). Rather than time averaging the flow, as in the case of RANS, turbulent eddies larger than the grid resolution are instead resolved. This can increase the accuracy of such models, however with an increase in computational time. Due to the eddies being resolved in LES, the wind turbines are modelled by a method known as an *actuator disk*. The drag forces associated with the wind turbine are distributed along the turbine blades, which in turn rotate within the model. This means that tip vortices and turbine wake rotation are included in the model. On the other hand, RANS have been used to look at the larger scale impact from wind farms on the meteorology (Baidya Roy, 2011; Baidya Roy *et al.*, 2004; Fiedler & Bukovsky, 2011; Vautard *et al.*, 2014). RANS are used at a coarser resolution than LES and hence wider reaching effects can be modelled. Each wind turbine is instead parametrised as a sink of momentum, with recent studies also including a source of turbulent kinetic energy from each turbine. This parametrisation is explained in detail in section 3. A final method of modelling wind farms was proposed by Smith (2010). A linear model was developed to assess the velocity and pressure perturbations associated with a wind farm within a neutral boundary layer. The mathematics of this model are described in chapter 5.

2.4 Wind turbine wake dynamics

The first stage in the understanding of wind turbines is to analyse the structure of the turbine wake. This section includes a description of the internal statistics of a turbine wake, including the velocity and turbulence profiles. The 3D structure of the wake will also be discussed, in particular the effect of rotation from the turbine blades and changes to surface fluxes. The way in which a wind turbine interacts with boundary layers of different stability will also be considered. In

order to be consistent with current research, the measurements associated with wind turbine wakes are normalised with the turbine rotor diameter D.

2.4.1 Wake geometry

A wind turbine wake is a patch of air that starts from the turbine blade and propagates downstream. One feature of a turbine wake is enhanced turbulence which is caused by the aerodynamic drag and the physical rotation of the turbine blades. The extraction of kinetic energy from the flow causes the velocity to significantly decrease from upstream of the wind turbine. The wake from a single turbine is evident up to $20D$ downstream (Wu & Porte-Agel, 2011). When multiple turbines are part of a larger wind turbine array, the combined wake effects can be seen up to 20 km down wind (Christiansen & Hasager, 2005). The exact distance it takes for a wake to decay is dependant on the surrounding atmospheric conditions, most notably the surrounding stability. Fitch *et al.* (2013) showed that the wake from a wind farm can be up to 3 times longer in stable conditions compared to unstable daytime conditions. The wake characteristics change depending on the position from the blades. The area up to $2D$ is classed as the near wake. Within this area the wake is dominated by the rotation of the blades and the instantaneous loss of kinetic energy. After $2D$ the wake is fully developed (Barthelmie *et al.*, 2013; Sanderse *et al.*, 2011) and is referred to as the far wake. Here turbulent interactions between the wake and the ambient air cause the wake to expand (Barthelmie *et al.*, 2013). The growth of the width of the wake, $w(x)$, follows a power law

$$w(x) = w_0 \left(\frac{x}{D}\right)^m \tag{2.8}$$

where $m = 1/3$ and w_0 is the wake width at $x/D = 1$. By using a large collection of observations, Aitken *et al.* (2014) showed that $w_0 = 1.3D$. This power law assumes a uniform boundary layer profile throughout the length of the wake. The height of the wake also increases downstream from the turbine, however, due to interactions with surface friction and differences in stability, it does not follow the same power law. The vertical growth rate of the wake in neutral conditions has been shown to begin breaking down at $7D$ downstream (Wu & Porté-Agel, 2012).

The differences in wake expansion in the horizontal and vertical directions are an example of anisotropic properties in the wake. The rotation from the turbines mixes low velocity air from near the surface higher into the wake on one side and the reverse on the opposite side of the wake where faster flow is mixed to lower levels. The latter can cause an acceleration of up to 11 % (Fitch *et al.*, 2013). The change in ambient flow velocity throughout the height of the wake causes a stretching of the helicodial vortices in the upper part of the wake (Lu & Porte-Agel, 2011). This results in the wake being tilted towards the ground, as shown by Lu & Porte-Agel (2011).

2.4.2 Velocity deficit

One of the concerns from wind turbines and their wakes is the reduction in velocity downwind. With the majority of wind turbines being installed in larger wind farm arrays, wind turbines are often positioned within an upwind turbine wake. This impacts the power that can be generated due to the reduction in velocity. Understanding the magnitude and extent of reductions in velocity is of importance to the wind energy community to optimally position wind turbines in a wind farm array.

The reduction in velocity within the wake is called a velocity deficit (VD)

$$\mathrm{VD} = \frac{U_{free} - U_{hub}}{U_{free}} \times 100 \tag{2.9}$$

where U_{free} is the freestream velocity at hub height and U_{hub} is the hub height velocity. LIDAR observations from Wang & Barthelmie (2015) showed that at a distance of $1D$, $\mathrm{VD} = 56\,\% \pm 4\,\%$. The velocity deficit continuously decreases throughout the wind farm wake, reaching $15\% - 25\%$ at $x = 6.5D$ (Aitken *et al.*, 2014). The maximum velocity deficit occurs below the hub height. This is an effect of the downward tilt and also drag associated from the turbine tower (Crespo *et al.*, 1988). Large deficits, $VD \approx 70\%$, have also been shown in Iungo *et al.* (2013) and Smalikho *et al.* (2013) at a distance of $\approx 0.5D$. Hogstrom et al. (1988) empirically showed that the velocity deficit follows a power law. This has been confirmed by Aitken *et al.* (2014) who verified the power law against historical wind turbine wake data. At a distance x from the turbine, the velocity deficit is

$$\mathrm{VD}(x) = \mathrm{VD}_0 \left(\frac{x}{D}\right)^n \tag{2.10}$$

with $\mathrm{VD}_0 = 56\%$ being the initial velocity deficit at $x/D = 1$ and $n = -0.57$ is the wake decay coefficient. The velocity deficit applies only to the streamwise velocity component. The wake effects on vertical velocity are negligible (Iungo *et al.*, 2013). The recovery of the velocity within the wake is due to kinetic energy entrainment from the air aloft. This means that there is a negative momentum flux at the top of the turbine wake (Abkar & Porte-Agel, 2015).

2.4.3 Turbulent kinetic energy (TKE)

The second key feature of wind turbine wakes is an increase in turbulence. The large scale effects from an increase in turbulence is minimal. Smith *et al.* (2013) used LIDAR observations to show the effect of wind turbines on turbulence intensity (TI), which is the ratio of the standard deviation horizontal velocity to the mean wind in the sampling area

$$\mathrm{TI} = \frac{\sigma}{u}. \tag{2.11}$$

Although TI in the near wake can increase by $\approx 25\%$, the large scale TI in the wind farm wake increases by $< 2\%$ (Smith *et al.*, 2013) compared to unwaked regions. This is not to say that is it irrelevant to understand wind turbine turbulent effects.

The turbulence within the wake is not uniform. The upper half of the wake has greater turbulence with the maximum value at top tip height (Calaf *et al.*, 2011; Markfort *et al.*, 2012; Wu & Porté-Agel, 2012; Zhang *et al.*, 2012), with the exact location of the maximum turbulence being within $2D - 5D$ downstream (Iungo *et al.*, 2013; Wu & Porté-Agel, 2012). There is a secondary peak in turbulence just below hub height; a result of the negative turbulent advection in the upper half of the wake.

By looking at the turbulent momentum budget, studies have shown the dominant physics in the wind turbine wake. The wake at the top tip height has the greatest turbulent vertical momentum flux, showing that the wake acts by advecting the undisturbed air above. Wu & Porté-Agel (2012) showed that the TKE is generated by

$$-\overline{\widetilde{u}'\widetilde{v}'}\frac{\partial\overline{\widetilde{u}}}{\partial y} \text{ and } -\overline{\widetilde{u}'\widetilde{w}'}\frac{\partial\overline{\widetilde{u}}}{\partial z}. \tag{2.12}$$

This is due to the high radial shear that occurs in the turbine wake. The mean velocity in the streamwise direction, $\bar{\tilde{u}}$, is also the dominant term in the advection of TKE (Wu & Porte-Agel, 2011).

The above values associated with turbine wake turbulence have been shown through numerical models. The statistics of turbulence from real turbines are dependent on the background conditions, although it must be noted that the impact from the increased turbulence is small when compared to the background conditions (Smith *et al.*, 2013). Smalikho *et al.* (2013) used LIDAR measurements from a single turbine and observed changes to the wind farm wake from different atmospheric stabilities. With a hub height of 80 m and a rotor diameter of 101 m, the turbine wake extended between 120 m and 1180 m downstream. Although changes in the boundary layer wind speed caused changes in the wake length throughout the observation period, it was observed that halving the wake led to an increase in turbulence intensity by a factor of 1.7. This highlights the importance of understanding how turbine wakes change in different ambient conditions.

2.4.4 Boundary layer stability impacts

The previous sections have implied that the magnitude of a wind turbine wake is dependent on the surrounding stability. It is therefore appropriate to look at different stability situations and assess the characteristics of the wake. The largest impact on the structure of a wake is in an unstable boundary layer (Abkar & Porte-Agel, 2015). An unstable boundary layer occurs during the day where there is strong surface heating causing a negative lapse rate of temperature throughout the surface layer, with a well mixed layer above. Convective plumes can then occur within the boundary layer which are associated with greater ambient turbulent kinetic energy. The addition of wind turbines produces strong turbulence within the wakes, of the magnitude $4.6\mathrm{m}^2\,\mathrm{s}^{-2} - 3.9\mathrm{m}^2\,\mathrm{s}^{-2}$, where the mean flow velocity is $7\,\mathrm{m\,s}^{-1}$ (Lu & Porte-Agel, 2015). This increase in turbulence manifests itself as higher turbulent transport towards the centre of the wake (Abkar & Porte-Agel, 2015). The peak in turbulence which occurs at the centre of the wake is therefore greater in an unstable boundary layer compared to stable or neutral, of the order 15% at $x/D = 2$ and 20% at $x/D = 3$ greater. The addition of more background turbulence in the unstable boundary layer induces stronger vertical

mixing which results in a faster wake recovery compared to a neutral boundary layer (Zhang *et al.*, 2012). Zhang *et al.* (2012) used a wind tunnel with a heated floor of $\theta = 346\,\mathrm{K}$ and air temperature of $\theta = 283\,\mathrm{K}$. The Reynolds number was small meaning there are possible scaling issues with the results, hence the specific values are not included. The study does however provide useful evidence for the impact from additional ambient turbulence. RANS have shown the same trend with Fitch *et al.* (2013) finding that the TKE in the upper part of the wake, which is dominated by wind shear, was 33% larger in an unstable boundary layer compared to a stable boundary layer.

The additional turbulence in an unstable boundary layer means that the velocity deficit is smaller. Zhang *et al.* (2012) found that the VD at the wake centre is 15% less compared to stable conditions. Christiansen & Hasager (2005) observed that at 1 km downstream of the Horns Rev and Nysted wind farm, the velocity deficit peaked at 8% and quickly reduced to 2% after a further 3 km. The increase in vertical mixing means that the effects from the turbine wake are dispersed further, up to a height of $300\,\mathrm{m} - 400\,\mathrm{m}$ (Vanderwende & Lundquist, 2016). By using LES, Lu & Porte-Agel (2015) simulated an infinitely large wind farm in an unstable boundary layer. It was found that the boundary layer height increased by 16% with the addition of the wind turbines. Furthermore, it was found that the surface temperature increased by 0.5 K. In an unstable boundary layer this is due to the increase entrainment flux at the top of the boundary layer mixing slightly warmer air into the boundary layer from the air aloft. The increase in boundary layer mixing induces the surface temperature change. Details of the latter two impacts will be described in 2.5.1.

A neutral boundary layer shows similar effects on the wind turbine wake as an unstable boundary layer. The near wake region shows the same properties because this region is dominated by mechanical shear from the turbines (Zhang *et al.*, 2012). The neutral boundary layer is already a well mixed layer, but without the additional surface heating. Zhang *et al.* (2012) showed that the turbulence intensity between a neutral and unstable boundary layer differs at the surface, the region where the thermal effects in the unstable boundary layer are of a greater magnitude.

On the other hand, a stable boundary layer exhibits different properties. The impact from the wind turbine wake is greater in stable conditions with an increase

in velocity deficit and increase in TKE (Lu & Porte-Agel, 2011). Abkar & Porte-Agel (2015) showed through LES that the velocity deficit can be up to 50% larger in a stable boundary layer compared to neutral and unstable conditions. This is due to the negative buoyancy flux in the stable boundary layer which inhibits the wake turbulence and thus produces a longer turbine wake, with the wake still being present at $x/D = 20$. Whereas in the neutral and unstable cases the wake effects at this distance are negligible (Abkar & Porte-Agel, 2015).

2.4.5 Wind farm efficiency

The information above on velocity deficits and turbulence only describes numerical values. These changes impact the efficiency of the wind farms, with a decrease in efficiency results in less power output. The research of Barthelmie *et al.* (2013) looked at the meteorological impact on wind farm efficiency. It was found that in general, lower input wind speeds reduce the efficiency by up to 60%. This is due to the greater drag coefficients which occur at low wind speeds above the cut in speed. Within the wind speed range of 5 $\mathrm{m\,s^{-1}}$ to 15 $\mathrm{m\,s^{-1}}$ the power loss from turbines within an upstream turbine wake was lower in neutral conditions, with a greater power loss in stable conditions. By contrast, in a convective boundary layer a wind farm is $5\% - 9\%$ more efficient than in a stable boundary layer for the same wind farm layout (Barthemlie & Jensen, 2010). This is a result of the stable conditions inhibiting mixing leading to longer lasting turbine wakes. Assuming that the atmospheric conditions remain constant, higher wind speeds result in more efficient turbines. With an increase in wind speed comes a greater power output. The turbines are also more efficient, with the greatest efficiency occurring above the rated wind speed. For this reason, wind turbines produce more power at night, even though the stability does not suit it. This is due to the greater wind speeds which occur at night with a lower boundary layer compared to the day time boundary layer, and the formation of a low level jet at the top of the rotor area (Fitch *et al.*, 2013).

2.4.6 Wind turbine arrays

Up to this point wind turbine wakes have been described for both individual turbines and multiple turbines in arrays without detailed understanding of the

dynamics of wind farms. From the literature, it can be seen that there are two concerns from wind farms: the first being power output from turbines within upstream turbine wakes and the second being the larger scale impact on the atmosphere from a larger area of drag and increased turbulence. One method of representing the large scale effect from a wind farm is to treat it as a single patch of drag. Frandsen (2007) postulated that the drag coefficient from a wind turbine array is

$$C_{Ta} = \frac{1}{8}\frac{ND^2\pi}{A}C_T \tag{2.13}$$

where the drag from an individual turbine is C_T, A is the area of the array and N is the number of turbines. This method fails to include the associated turbulence and the effect from turbine wakes mixing within the array. It does however assist with the idea that a wind turbine array creates a large scale wake, referred to as a wind farm wake. The wind farm wake has been shown to have a greater velocity deficit than the velocity deficits observed over the wind farm area. At 10 km − 20 km downwind the combination of drag from each turbine creates a larger VD than over the wind farm area (Fitch *et al.*, 2013). Other studies, Christiansen & Hasager (2005), have shown that the velocity deficit is reduced to 2% close to the wind farm area, implying a small wind farm wake. These contrasting results hint at uncertainty in the size of a wind farm wake and hence uncertainty as to the large scale impact.

With multiple turbines the issue of turbine layout is an important area of understanding. Each wind farm site will have specific constraints to the possible layout, with the main issue for offshore farms being sea depth. This makes it difficult to extrapolate research on wind farm layout to a specific site, however it is possible to understand the general impact of different layouts. The main two layouts which have been research are aligned, where the turbines are positioned behind one-another in the stream wise direction, and the second being staggered where downwind turbines are offset by half the distance between a turbine and the neighbouring turbine in the span-wise direction. A staggered wind farm means that downwind turbines are not directly in the wake. There is then a greater distance between turbines downwind which results in more effective mixing of the wakes (Zhang *et al.*, 2013). With the wakes decaying at a greater rate there is therefore an increase in the velocity being input into each turbine in the array. This increases the power output however, with a result of increasing the impact from the wind farm on the surroundings (Lu & Porte-Agel, 2015).

2.5 Meteorological impacts

The previous section highlighted the key dynamics associated with wind turbines and wind farms. In this section we aim to understand what is known about their impact on the meteorology. Although presented in term of the meteorological impact from wind turbines, most of the literature aims to understand the impact from the meteorology on the wind farm efficiency.

2.5.1 Temperature changes

The most coherent evidence for wind farm impacts is on temperature. Smith *et al.* (2013) found that during the night time stable boundary layer, a wind farm increased the 2.5 m temperature by between $1.6 - 1.9\,\mathrm{K}$. The increase in temperature results is an increase in temperature lapse rate through the wind farm, in the range of $0.022\,\mathrm{K\,m^{-1}} - 0.026\,\mathrm{K\,m^{-1}}$, depending on the proximity to a turbine (Smith *et al.*, 2013). This data is taken from the average of 46 days thus limiting the variation from mesoscale activity. Increasing the surface temperature has a statistically significant positive correlation with an increase in the lapse rate, shown by Baidya Roy (2011), through numerical models. It should be observed that Baidya Roy (2011) used a fixed thrust coefficient $C_T = 0.4$ which for most wind turbines assumes an input velocity near the rated wind speed. The increase in surface temperature impacts the regional climate. Zhou *et al.* (2012) used satellite data and observed that the addition of $2,358$ turbines in Texas increases the temperature in JJA by $0.72\,\mathrm{K}$ per decade and $0.46\,\mathrm{K}$ per decade in DJF. This is calulated by looking at the annual land surface temperature difference between areas of land that contain a wind turbine and areas that are within close proximity to a wind turbine. The land surface temperature differences are stronger at night, with greater interannual variability present during the day. These increases occur downstream of the wind turbines, with stronger winds in JJA inducing a larger temperate increases. The increases in temperature are not noticed outside the vicinity of the wind farms and hence there are no large scale impacts. On the other hand, the majority of these turbines are within agricultural fields which raises questions of the impact on the crops. Fitch *et al.* (2013) showed, by simulating a diurnal cycle, that when the TKE in a wind farm doubles it corresponds to a temperature increase at 2 m; halving the TKE

also decreases the temperature. The temperature changes initially occur within the rotor area with a large increase below the rotor area, of the order 1 K (Fitch *et al.*, 2013), which reduces in magnitude by the time it is advected to the surface. The turbine wake also mixes cooler air from the surface to the top of the wake, reducing the temperature; with a 0.3 K decrease observed in Fitch *et al.* (2013). This shows that the increases in surface temperature are due to the turbine mixing within a boundary layer with positive temperature lapse rate. Warmer air is mixed down to the cooler air at the surface. Baidya Roy & Traiteur (2010) found that during the day, when there is negative lapse rate, cooling occurs at the surface. Although this is possible, the increase in background boundary layer mixing within an unstable boundary layer implies that any temperature decreases caused by the wind turbines are negligible (Zhou *et al.*, 2012).

Changes in surface temperature have been found through wind farm observations and numerical models. Although the dynamics involved are the same between the two methods, caution should be used with numerical values, especially from the numerical models. Cervarich *et al.* (2013) used numerical models with different wind farm parametrisations, with each parametrisation using different thrust and power coefficients. The parametrisations used theoretical coefficients which have high power and thrust coefficients and two other parametrisations based upon wind turbine observations. All parametrisations yielded a night-time surface warming with the theoretical parametrisation yielding greater increases than the other two parametrisations.

An interesting question from this is how will the temperature changes impact the wider climate in the future? Within Europe, the use of renewable energy sources is expected to rise to 20% by the year 2020 (The European Wind Energy Association, 2014). This means there will be an increase in wind turbines, along with other renewable energy devices. Vautard *et al.* (2014) simulated the impact of increasing the renewable energy power solely from wind power, distributed in possible locations throughout Europe. It was found that large-scale temperature changes would occur, with the Baltic sea region temperature amplitude increasing by 0.3 K and the temperature amplitude decreasing by 0.1 K in south-west Europe. Also, density increases enhance the turbulence. It was argued that within stable boundary layers, this would result in clearer skies and hence more incoming shortwave radiation (0.15 $\mathrm{W\,m^2}$) and less long wave radiation (0.8 $\mathrm{W\,m^2}$) (Vautard *et al.*, 2014). There is, however, no recorded evidence of the latter effect

occurring. As shown in Cervarich *et al.* (2013), temperature change values from RANS should be treated with caution as there is dependence on the wind farm parametrisation. Furthermore, Vautard *et al.* (2014) used theoretical drag and power coefficients for additional turbines that would be needed to meet the 2020 renewable energy target; this is another source of error as shown in Cervarich *et al.* (2013).

2.5.2 Precipitation

The effect of wind farms on precipitation has also been studied. In addition to temperature changes, Vautard *et al.* (2014) assessed the impact of wind farms on precipitation with an increase in wind farms. It was found that precipitation would reduce by $\approx 5\%$ over Western Europe. Further changes to precipitation from wind farms have been found in Fiedler & Bukovsky (2011). This study simulated a large wind farm consisting of $228,375$ turbines covering an area of $182,700$ km^2 in the Great Plains region of America. A 62 year simulation was carried out, resulting in fluctuations to the precipitation of up to 1%, depending on the location inside or outside of the wind farm. Although the set up for this study is unrealistic in size, it does highlight that even a very large wind farm has a small impact on precipitation, an impact which would be challenging to observe over general precipitation variation. Both of these studies provide little credible evidence that wind farms can impact the precipitation within a region.

2.5.3 Boundary layer profile

The studies described so far focus on changes within the wind farm area, but not the wider impacts. The purpose of a wind farm is to generate electrical energy from the kinetic energy in the ambient wind. The power extracted is directly correlated to the vertical fluxes of kinetic energy above the wind farm area (Calaf *et al.*, 2010). This implies that the reduction of kinetic energy from the turbines is compensated for by the addition of kinetic energy from the air flow above the wind farm (Calaf *et al.*, 2010). This results in a growth in the boundary layer height. Lu & Porte-Agel (2011) used LES with a stable boundary layer with wind turbines spaced either $8D$ or $5D$ apart. The $8D$ wind farm increased the boundary layer by $\approx$ 28%, with an $\approx 43\%$ increase in the $5D$ case. Unsurprisingly, a denser

wind farm has a greater impact, although the LES had an initial boundary layer height of 175 m hence the turbines occupied a large portion of the boundary layer. Further studies have shown the same affect. Lu & Porte-Agel (2015) modelled LES with aligned wind farm and a staggered wind farms and found that both arrangements led to a 16% increase in the boundary layer height. This included boundary layers of height 600 m to 800 m. Moreover, Allaerts & Meyers (2015) simulated a neutral boundary layer with a capping inversion. LES's with no wind farms were carried out until the inversion height growth rate became steady ($\approx 12\,\mathrm{m\,s^{-1}}$) at which point wind farms were added into the simulation. The results show that the boundary layer height is an import factor for boundary layer growth. Csanady (1974) derived an empirical equilibrium height for the boundary layer (h_e),

$$h_e = A\frac{\theta_0}{g\Delta\theta}u_*^2 \tag{2.14}$$

where u_*^2 is the surface friction, θ_0 is the boundary layer temperature, $\Delta\theta$ is the capping inversion strength and $A \approx 500$ in an empirical parameter. For boundary layer heights initialised above h_e, there is a slower growth rate compared to those simulations with a smaller boundary layer. There are also decreases in the growth rate for increasing $\Delta\theta$ and boundary layer height (Allaerts & Meyers, 2015). The effects of changing the inversion strength are reduced above the Ekman layer. The similarity parameter, $h_* = |f|h/u_*$, can be defined, with negligible effects from inversion strength when the boundary layer height, z_i, satisfies $h_* > 0.15$ (Hess, 2004).

Increases in the boundary layer height from a wind farm show that the signal from a wind farm has a greater scope than just the wind farm wake. These studies have been centred around the efficiency of wind farms, altering wind turbine spacing within the wind farm. The wider impacts on the boundary layer from the wind farm have been neglected, and this was mainly due to the use of LES whereby further reaching impacts cannot be simulated.

Further changes to the boundary layer profile have been shown. The reduction in wind speed within the wind farm induces a change in the Ekman spiral, with a clockwise rotation in the upper rotor area and anti-clockwise rotation in the lower half (in the Northern Hemisphere) (Fitch *et al.*, 2013). The momentum loss from the turbines also causes the disappearance of the low level jet which occurs at night (Fitch *et al.*, 2013; Lu & Porte-Agel, 2011).

2.5.4 Wind turbine and surface interactions

A final area of interest with wind farms is their interaction with surface features. The first interaction is with crops. This is a two way interaction; the dynamics of the wind farm impact crop yield and the second being the crop impact on power output. Vanderwende & Lundquist (2016) looked at the second effect, assessing how a change in crop can affect the wind turbines. Two crop types were used: soybeans with $z_0 = 0.1\,\mathrm{m}$ and maize with $z_0 = 0.25\,\mathrm{m}$. The soybean with small surface roughness increased the median wind speed within the rotor area compared to the maize, with increases in the range $0.21\,\mathrm{m\,s^{-1}}$ to $0.35\,\mathrm{m\,s^{-1}}$ (Vanderwende & Lundquist, 2016). The decrease in surface roughness from the soybeans means that the shear within the rotor area decreases, with a decrease of 23% in unstable conditions and 13% in neutral conditions (Vanderwende & Lundquist, 2016). This translates to an increase in power output for the same atmospheric conditions. By changing the surrounding crops, the soybeans increased energy production by 14% (Vanderwende & Lundquist, 2016).

Boundary layer flux differences have been observed in the Crop Wind Energy Experiment (CWEX) Rajewski *et al.* (2014). Daytime latent heat fluxes and CO_2 increases were observed downstream of a row of wind farms. Clear differences in the latent heat flux were not observed in upstream and downstream measurements, however at $3-5D$ downstream there was an increase of $5-15\%$ (Rajewski *et al.*, 2014). Similarly, at $5.5D$ downstream, CO_2 increased by $8-12\%$ (Rajewski *et al.*, 2014). Rajewski *et al.* (2014) observed that these differences are less than between different crop irrigation methods in Suyker *et al.* (2004). Night time increases in CO_2 flux within the wind turbine wake occur by $1.5-2$ times reference values, attributed to the wind speed increase above the boundary layer and thus enhanced mixing within the turbine wakes. Over a diurnal cycle, there are negligible changes to the CO_2 within the turbine wake.

Not only can surface roughness change the power output, but so can surface orography. If a turbine is downwind of a hill then the wind speed at hub height can be altered. This effect occurs when the hill is greater than $z_h - 0.5D$ in height, where z_h in the hub height, and located less than $6D$ upstream (Yang *et al.*, 2015). The disturbance to the air created by the hill increases turbulence and hence reduces the wind speed for downwind turbines. However, the increase

in turbulence increases the wake recovery, meaning there can be a greater turbine density which in turn increases power output. This once again shows it is challenging to describe general wake interactions and power output for real wind farms. Each situation must be treated independently.

2.6 Summary

Having summarised the literature, it can be seen that, although there is research involving wind farms, wind farm efficiency and power output are the areas of interest. Field measurements are challenging to obtain for wind farms, both from an operational and commercial point which means numerical simulations are the tool of choice. The LES that have been used provide a useful insight into the dynamics around a wind turbine and wind farms, but fail to give a detailed understanding of the larger impacts on the boundary layer. LES are limited in this area as there is a high computational expense in doing such simulations. To look at the wider impacts, RANS should be used. Fitch *et al.* (2013) touched on this area by looking at the diurnal effects on a wind farm, however these simulations were once again centred around wind farm power.

A key area missing from the literature is the wider reaching effect of wind farms on the boundary layer. LES studies have been used to look at the impact of wind farms on the boundary layer height. Lu & Porte-Agel (2015) found that the boundary layer height increases by 16% with the inclusion of a wind farm, however with a domain size of $3\,\mathrm{km} \times 3\,\mathrm{km}$ and boundary layer heights of $600 - 800\,\mathrm{m}$, the larger scale impact from the wind turbines was not investigated. The use of periodic boundary conditions, and hence infinitely large wind farm, meant that the transition of undisturbed flow to flow through wind farms was not studied. Allaerts & Meyers (2015) also used LES with wind farms in a neutral boundary layer however once again the smaller domain size in the LES limited the ability to investigate the impact of wind farms on the boundary layer. The research in this thesis aims to identify the impact from wind farms on the boundary layer using larger domain sizes than previous work. The ability to run larger domains means that boundary layer perturbations can be analysed upstream and downstream of a wind farm. Furthermore, wind farms in RANS have previously been used to look at large long term impacts from wind farms, such as in Fiedler & Bukovsky (2011)

and Vautard *et al.* (2014), however these studies were carried out without a full understanding of the dynamics of wind farm models in RANS. When wind farms have been used in RANS, different boundary layer scenarios have been used to identify changes in power output from the wind farms. This study will not focus on the power output from the wind farms, but instead look at the feedback from the wind farm back into the boundary layer. This approach exploits the ability of RANS to model the boundary layer, rather than be used as a wind farm power model. The impact from wind farms on small scale meteorological features, such as gravity currents, has not been studied in the literature. This includes studies using both LES and RANS simulations. Once the impacts from wind farms in the boundary layer have been understood then the impact on meteorological features can begin to be investigated. This idea will be explored in chapter 6 where the idea of wind farm in a sea breeze is considered.

Chapter 3

Numerical models and the wind farm parametrisation

In the subsequent chapters, numerical models will be used to assess the impact of wind farms in various circumstances. Two numerical models will be used: BLASIUS and WRF. In this chapter BLASIUS and WRF will be described. Both models will use a wind farm parametrisation (WFP). The details of the WFP will also be described. Details of the set up for the BLASIUS and WRF simulation will be left until chapters 4 and 6 respectively.

3.1 Met Office BLASIUS model

The primary model for this work is the Met Office BLASIUS (Boundary Layer Above Stationary, Inhomogeneous Uneven Surfaces) model. BLASIUS was initially developed by Wood & Mason (1993) and Wood (1995) to investigate flow over hills. In recent years, BLASIUS has been extended to model flow through forest canopies (Ross & Vosper, 2005). BLASIUS is therefore the perfect model to model wind farms in the atmospheric boundary layer.

BLASIUS solves the time dependent Boussinesq equations. The velocity vector is given by $\mathbf{U} \equiv (U, V, W)$. All variables are Reynolds averaged. This means representing them in terms of a mean component and a perturbation from the averaged flow, for example $U = u_0 + u'$. The 3-d momentum equations are then

$$\rho_0 \frac{DU}{Dt} - \rho_0 fV = -\frac{\partial P'}{\partial x} + \frac{\partial \tau_{11}}{\partial x} + \frac{\partial \tau_{12}}{\partial y} + \frac{\partial \tau_{13}}{\partial z} \tag{3.1}$$

$$\rho_0 \frac{DV}{Dt} - \rho_0 fU = -\frac{\partial P'}{\partial y} + \frac{\partial \tau_{21}}{\partial x} + \frac{\partial \tau_{22}}{\partial y} + \frac{\partial \tau_{23}}{\partial z} \tag{3.2}$$

$$\rho_0 \frac{DW}{Dt} = -\frac{\partial P}{\partial z} - \rho' g + \frac{\partial \tau_{31}}{\partial x} + \frac{\partial \tau_{32}}{\partial y} + \frac{\partial \tau_{33}}{\partial z} \tag{3.3}$$

with the material derivative defined as

$$\frac{D}{Dt} \equiv \frac{\partial}{\partial t} + U\frac{\partial}{\partial x} + V\frac{\partial}{\partial y} + W\frac{\partial}{\partial z}. \tag{3.4}$$

Additional terms given here are density ρ, pressure P, Coriolis parameter f, gravity g and Reynolds stress $\tau \equiv \tau_{ij}$. The mass conservation equation is

$$\frac{\partial \rho_0 U}{\partial x} + \frac{\partial \rho_0 V}{\partial y} + \frac{\partial \rho_0 W}{\partial z} = 0. \tag{3.5}$$

From Newton's 2nd law, the thermodynamic equation (with potential temperature Θ) is

$$\rho_0 \frac{D\Theta}{Dt} = \frac{\partial H_x}{\partial x} + \frac{\partial H_y}{\partial y} + \frac{\partial H_z}{\partial z}. \tag{3.6}$$

The turbulent flux of potential temperature in the ith direction is given by H_i. Finally, the turbulent kinetic energy (TKE) is defined as $k = (1/2)(u'^2 + v'^2 + w'^2)$. Using the eddy viscosity ν and a kinetic energy dispersion rate ϵ, k can be expressed as

$$\rho_0 \frac{Dk}{Dt} = \frac{\partial}{\partial x}\left(\rho_0 \nu \frac{\partial k}{\partial x}\right) + \frac{\partial}{\partial y}\left(\rho_0 \nu \frac{\partial k}{\partial y}\right) + \frac{\partial}{\partial z}\left(\rho_0 \nu \frac{\partial k}{\partial z}\right) + \tau_{ij}\frac{\partial U_i}{\partial x_j} - \frac{2}{3}\rho_0 k \nabla \cdot \mathbf{U} - \rho_0 \epsilon - \frac{H_z g}{\Theta} + \mathrm{A}. \tag{3.7}$$

The term A is a place-holder for any additional TKE terms which may be added as part of the model parametrisations. In BLASIUS simulations with no additional parametrisations A = 0. In addition, BLASIUS can model water vapour leading to a further equation and modifications to equation 3.7. The work presented solely uses dry air and thus the water vapour equation is neglected.

The largest challenge in modelling these equations lies with the TKE. Turbulence can vary in magnitude, which results in turbulent eddies being smaller than the smallest grid cell. Turbulence closure schemes are used to represent turbulence in BLASIUS, as is done in most RANS models.

3.1.1 Boundary conditions

Simulations in BLASIUS can either have a free-slip or no-slip lower boundary condition. All simulations presented in this study will use the no-slip boundary condition, which is described below.

The coordinate system in BLASIUS positions the lowest horizontal velocity components below the surface layer. The lower velocity boundary conditions are then

$$u_{ij1} = -u_{ij2} \quad v_{ij1} = -v_{ij2} \quad w_{ij1} = 0 \tag{3.8}$$

To complete the lower boundary conditions, similarity theory is used between the surface layer and the lower velocity level. This enables the surface stress terms to be calculated.

For simulations with a flat surface, the surface stresses are given as:

$$\tau_x = \rho u_*^2 \frac{U}{\mathbf{U}} \tag{3.9}$$

$$\tau_y = \rho u_*^2 \frac{V}{\mathbf{U}} \tag{3.10}$$

At the upper boundary there is zero vertical mass flux. The velocity at the upper boundary is then prescribed during model set up. This is true for the horizontal terms and also with $w = 0$.

3.1.2 Turbulence closure scheme

Turbulence in BLASIUS can be modelled in one of three ways: neglect turbulence by setting ν to be constant, parametrising ν in a 1st order closure scheme and

finally carry TKE with a 1.5 order closure scheme. All BLASIUS simulations will be run with the latter.

In order to close the equations, equations for H_i, ν and ϵ are required. The Reynolds stress is given by $\tau_{ij} = \rho\nu S_{ij}$ where S_{ij} is double the non-isotropic part of the rate of strain tenor

$$S_{ij} = \frac{\partial U_i}{\partial x_j} + \frac{\partial U_j}{\partial x_i}. \tag{3.11}$$

The turbulent fluxes of Θ are given by

$$H_i = \rho_0 K \frac{\Theta_0}{g} \frac{\partial T}{\partial x_i} \tag{3.12}$$

where K is the temperature diffusivity. The Richardson flux number, Ri_f, which is the ratio of the buoyancy and the negative shear term from the TKE budget equation. The stress energy ratio Λ can be calculated by

$$\Lambda(Ri_f) = \Lambda(Ri_f = 0)(1 - Ri_f)^{-1/2}, \tag{3.13}$$

with $\Lambda_0 = \Lambda(Ri_f = 0)$. In the 1.5 order closure, the eddy viscosity and dispersion rate are given by

$$\nu = \Lambda_0^{\frac{1}{2}} k^{\frac{1}{2}} L_m \tag{3.14}$$

$$\epsilon = k^{\frac{3}{2}} L_T^{-1}. \tag{3.15}$$

L_T is the turbulent length scale and is assumed to be

$$L_T = \frac{L_m}{\Lambda_0^{\frac{3}{2}}} \tag{3.16}$$

where L_m is the mixing length scale of the dispersion rate

$$\frac{1}{L_m} = \frac{1}{L_0} + \frac{1}{\kappa z}. \tag{3.17}$$

This gives equations for ν and ϵ, thus closing the system of equations. BLASIUS has the capability to run in LES, however this is not done and will not be covered.

3.2 Weather, Research and Forecast model

The Weather, Research and Forecast (WRF) model is a numerical weather predication model used operationally and in research. This description focusses on the

Advanced Research WRF (ARW) version 3.6 Skamarock *et al.* (2008). The WRF ARW solves the fully compressible, non-hydrostatic Euler equations, using the conserved forms of the flux equations. The vertical grid used is a mass based grid system. Each vertical point is prescribed in relation to the hydrostatic pressure at the bottom surface of the model. These points can either be user defined or defined using a stretched grid. A stretched grid gives a greater number of model levels near the lower surface. The vertical coordinate system is a terrain following coordinate system, although all WRF simulations model a flat surface. The WRF ARW employs a Runge-Kutta time integration scheme. Atmospheric turbulence is simulated with a 1.5 order turbulence closure scheme.

The WFP parametrisation described in the following section is implemented in WRF. WRF is used in chapter 6, where a description of the set up in WRF and the parametrisations used will be presented.

3.3 Wind farm parametrisation

It was shown in chapter 2 that the effect from a wind turbine is two-fold: a reduction of wind speed and an increase in turbulence. These two effects can be used to parametrise an individual turbine. The WFP described below is from Katic *et al.* (1986) with the improvements from Fitch *et al.* (2012).

Each wind turbine exerts an aerodynamic drag F^T given by

$$F^T = \frac{1}{2}\rho C_D u^2 A. \tag{3.18}$$

The wind farm area is A and the drag coefficient is C_D. The drag coefficient is dependent on the wind speed and is unique for individual turbines. Figure 3.1 shows a schematic of a turbine in BLASIUS. Notice that the turbine rotor area spans multiple model levels. To allow for this, the turbine area per grid cell, A_{ijk}, must be calculated, where

$$A = \int A_{ijk}\,\mathrm{d}z. \tag{3.19}$$

Each grid cell has volume $\mathrm{d}x\,\mathrm{d}y\,\mathrm{d}z$ and velocity U_{ijk}. Using these, the turbine drag per cell is therefore

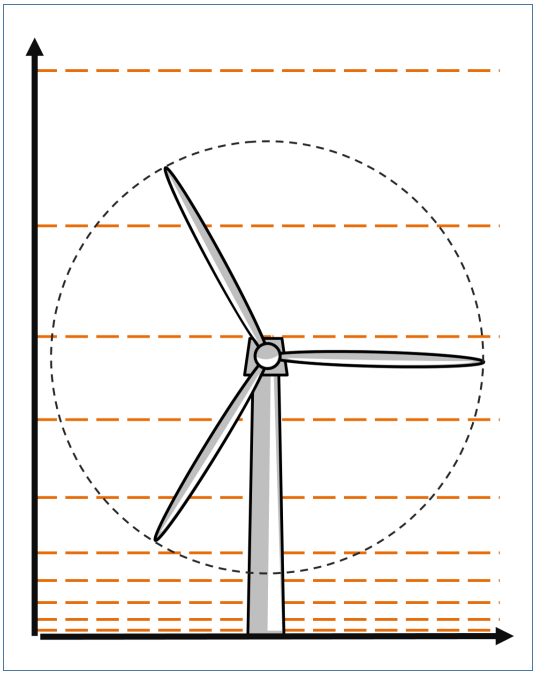

Figure 3.1: *Schematic of a simulated wind turbine in BLASIUS. The horizontal lines depict the model levels.*

$$F^d_{ijk} = \frac{1}{2}\rho C_D(U_{ijk})|U_{ijk}|U_{ijk}\frac{A_{ijk}}{\mathrm{d}x\,\mathrm{d}y\,\mathrm{d}z}. \tag{3.20}$$

Equation 3.20 is then subtracted from the source term of velocity in the model. In a similar way, the rate of change of turbine induced TKE is

$$\frac{\partial TKE_{ijk}}{\partial t} = \frac{1}{2}\rho(C_D - C_P)|U^3_{ijk}|\frac{A_{ijk}}{\mathrm{d}x\,\mathrm{d}y\,\mathrm{d}z}. \tag{3.21}$$

C_P is the power coefficient, and hence $C_D - C_P$ is the proportion of the flow is affected by the turbine drag but not converted into usable power by the turbine. Equation 3.21 is the set to be A in equation 3.7. Missing from this parametrisation is the effect from rotor tip vortices and the larger scale flow rotation caused by the turbine blades. These effects have the greatest impacts in the nearest $2D$ from the turbine. Beyond a distance of $2D$ the wake is fully developed and the rotation is a less significant factor Sanderse *et al.* (2011). This restricts the domain resolution to greater than this. Wu & Porte-Agel (2011) showed that grid spacings greater than $5D$ are required for parametrisations that do not include turbine rotation; this will be enforced in using the BLASIUS WFP.

The described WFP has been implemented into BLASIUS. The parametrisation allows a user defined number of turbines to be positioned anywhere in the domain. The drag and power coefficients can be controlled by the user, with the set up being that all turbines have the same characteristics. Although 3-dimensional wind farms can be modelled in BLASIUS, only 2-dimensional wind farms will be presented.

3.4 BLASIUS sensitivity to WFP

In order to test the BLASIUS WFP, 2-d idealised simulations are carried out. Prior to the 2-d run, a 1-d run with no wind farm is carried out. This is driven by a pressure gradient aloft resulting in a $12\,\mathrm{m\,s^{-1}}$ geostrophic wind. The run is initialised with a stable atmosphere with $N = 0.01\,\mathrm{s^{-1}}$. When running the 1-d simulation, a boundary layer is formed. This consists of a well mixed layer up to a height of 600 m, capped by a 1 K inversion layer. This run is then used to initialise the 2-d run with the wind turbine.

Simulations with different resolutions are tested. Both have a horizontal domain width of 200 km with the resolution being 500 m and 1 km. The wind turbine has a modelled hub height of 80 m and rotor radius of 40 m. This means that the higher resolution case is just above the limit suggested by Wu & Porte-Agel (2011) and Fitch *et al.* (2012). The vertical domain consists of 60 model levels with a stretched grid, starting at $z = 5\,\mathrm{m}$ with a stretched grid factor of 1.05, resulting in 6 model levels through the rotor blade area. Using this set up, different wind farms are tested. The first is a single turbine located in the centre of the domain and the second is a 10 turbine wind farm, also positioned in the centre of the domain.

The velocity perturbations shown in figure 3.2 show that the turbine wakes are similar between the two resolutions. The magnitude of the velocity perturbation is the same, however the wake is longer in the 1 km case. Similarly, the small oscillatory perturbations upstream are more prominent with $\mathrm{d}\,x = 1\,\mathrm{km}$. These perturbations are small scale grid noise and not relevant to this comparison.

The boundary layer TKE contours are shown in figure 3.3. They show a similar trend, with more elongated TKE perturbations when the resolution is 1 km.

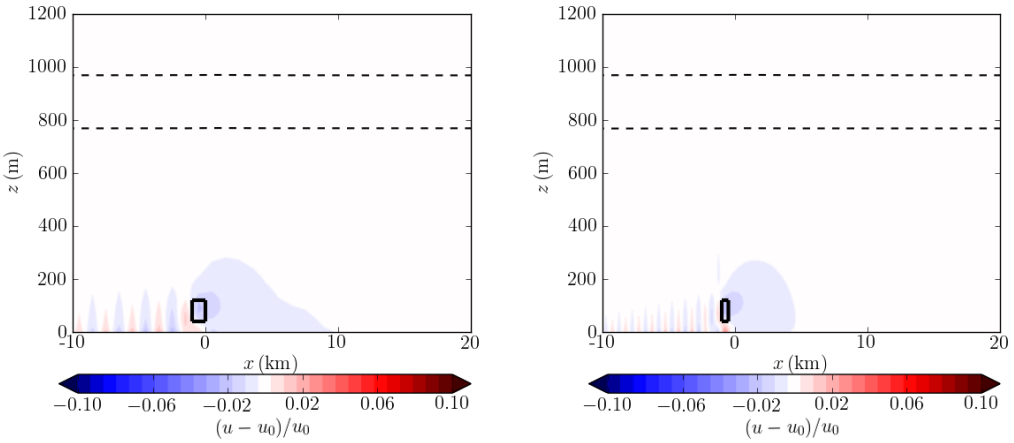

(a) **(b)**

Figure 3.2: *Velocity perturbations from a single wind turbine with (a)* $\mathrm{d}\,x = 1\,\mathrm{km}$ *and (b)* $\mathrm{d}\,x = 500\,\mathrm{m}$. *The dashed lines show potential temperature, with* $\mathrm{d}\,\theta = 1\,\mathrm{K}$ *between each line.*

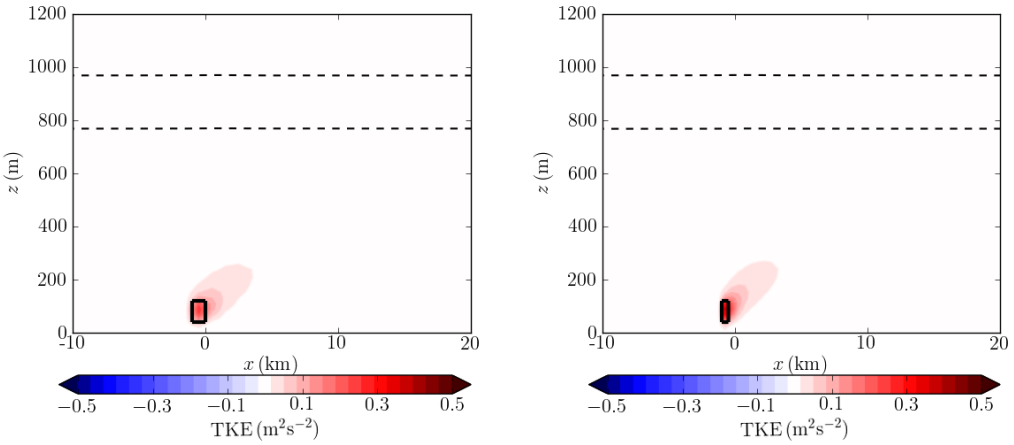

(a) **(b)**

Figure 3.3: *As described in figure 3.3 except the coloured contours show TKE perturbations.*

When a wind farm consisting of 10 wind turbines is modelled, there are once again differences from the resolution. The velocity perturbations in figure 3.4 show that there is more grid scale noise with $\mathrm{d}\,x = 500\,\mathrm{m}$. This extends 30 km upstream

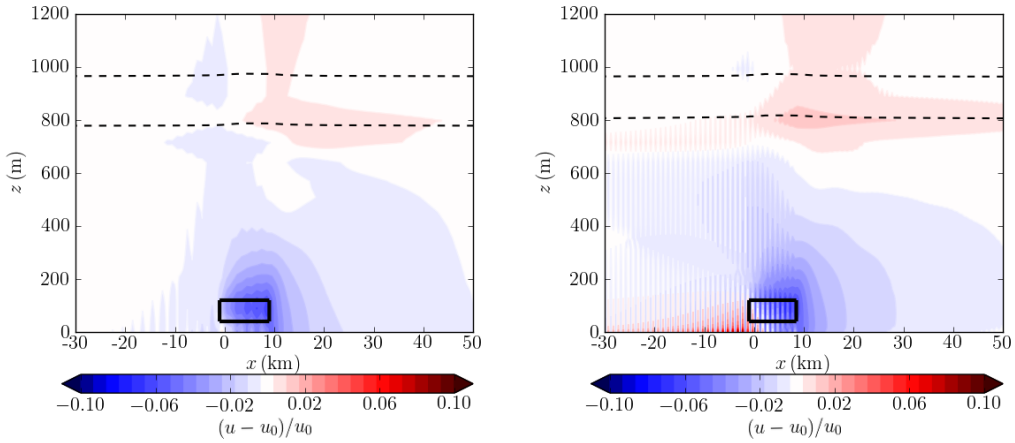

(a) **(b)**

Figure 3.4: *The velocity perturbations caused by a wind farm consisting of* 10 *wind turbines. As before, the black lines show potential temperature.*

of the wind farm throughout the boundary layer. Excluding the noise, however, there are similarites between the two plots. Resolution is therefore important when grid scale perturbations are present, however the larger scale perturbations show a coherent pattern. This is once again observed in the TKE perturbations in figure 3.5. The TKE perturbations show an increase in TKE around the wind farm in the wind farm wake. Below the wind farm rotor area there is a decrease in TKE. This is due to the lower velocity reducing surface friction and is consistent with Fitch *et al.* (2012).

The velocity perturbations shown here are similar to those derived from wind farm observations (Christiansen & Hasager, 2005; Iungo *et al.*, 2013). The velocity and TKE peturbations are also on par with those shown in Fitch *et al.* (2012). If anything, these perturbations are on the smaller side compared to the latter. This can be explained by the turbine differences; Fitch *et al.* (2012) modelled a 5 MW turbine whereas these simulations have turbine coefficients based on 2 MW turbine.

Horizontal resolution is an important factor to consider when running the BLASIUS WFP. This is due to the distribution of drag. Considering the turbine drag is distributed throughout the entire grid cell, smaller resolutions result in an increase in drag density. This is the reason behind the grid scale perturbations

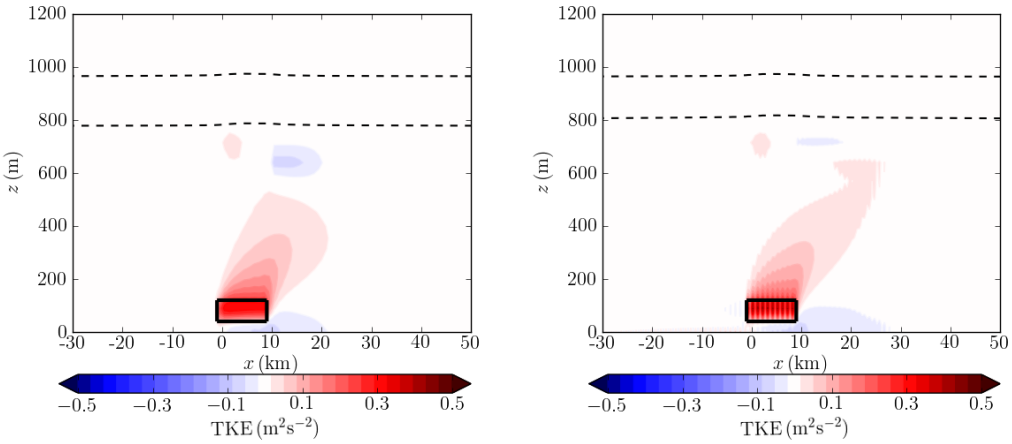

Figure 3.5: *As in figure 3.4 except plotting TKE perturbation contours.*

when $\mathrm{d}\,x = 500\,\mathrm{m}$. The reduction in noise for $\mathrm{d}\,x = 1\,\mathrm{km}$ shows that in order to model a wind farm with smooth perturbations, the horizontal resolutions need to match the spacing between the turbines. Decreasing the resolution to $\mathrm{d}\,x = 1\,\mathrm{km}$ decreases the grid scale noise shown in figures 3.2(b) and 3.4(b). The magnitude of both velocity and TKE perturbations is decreased when using a lower resolution, shown by the higher negative velocity in figure 3.4(b) compared to 3.4(a), and also the higher TKE shown in figure 3.5(b) compared to 3.5(a). This change in magnitude should be considered when running the WFP with $\mathrm{d}\,x = 1\,\mathrm{km}$.

To look at the effect of vertical resolution, two further simulations have been carried out. These have been set up in a similar way to the 10 turbine simulations with horizontal resolution of 1 km, except they have different model levels. The first simulation has 30 model levels and a stretched grid factor of 1.15. The lowest model level is once again at 5 m and there are 4 model levels throughout the rotor area. The lowest 1 km contains 13 model levels. The additional simulation has 45 model levels and a stretched grid factor of 1.1, with 5 levels being within the rotor area and 17 levels in the lowest 1 km. As a reminder, the simulation with 60 model levels has 6 levels within the rotor area, and it also has 26 model levels in the lowest 1 km.

Figure 3.6 shows the velocity contours in the 30 and 45 model level simulations. With the addition of figure 3.4, it can be seen that there is little change to the

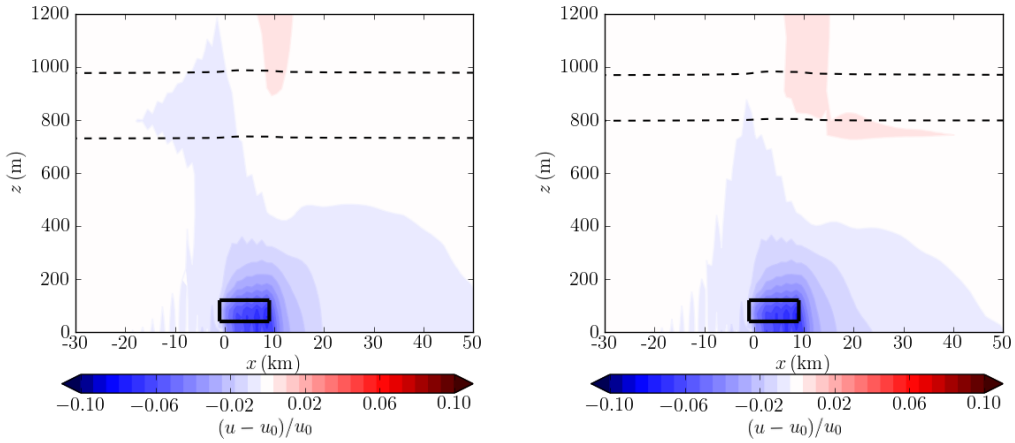

Figure 3.6: *Velocity difference contours for two 10 turbine simulations with different vertical resolutions. Plot (a) has* 30 *model levels and plot (b) has* 45 *model levels. In both cases, the black box represents the wind farm rotor area.*

velocity around the wind farm area. There is a subtle increase in the velocity deficit at 20 km as the resolution increases. This is caused by the increase in resolution in the upper part of the rotor area. Upstream of the wind farm there is still grid scale noise and the velocity deficit downstream extends to 50 km.

Changes in the velocity deficit can be observed above the wind farm and around the top of the boundary layer, found at 800 m. The higher resolution simulations have a greater increase in velocity along the boundary layer. The vertical resolution in the lowest 1 km is doubled between the 30 and 60 model level simulations. This leads to an increase in resolution around the boundary layer top. A lack of velocity increase in this area in the 30 model level simulation does not mean the velocity change does not occur, just that it cannot be observed. In order to look at the impacts on the boundary layer from wind farms, a higher vertical resolution should be used. This is so that there is sufficient resolution within the entire boundary layer.

3.5 Summary

The boundary layer model BLASIUS has been described, along with the turbulent closure scheme that will be used in subsequent simulations. BLASIUS simulations will include a wind farm parametrisation, based upon a turbine drag and turbulence increase. All work will involve this wind farm parametrisation. Furthermore, the BLASIUS WFP has been shown for both a single turbine and 10 turbine wind farm. Differences in horizontal resolution were observed in both simulations. In was concluded that the horizontal resolution should be considered when using the WFP, ideally matching the resolution with the turbine spacing. Vertical resolution does not make a big difference to the velocity deficits around the wind farm, although the simulations run only differ by 1 model level in the rotor area. Vertical resolution should however be considered for the entirety of the boundary layer to ensure any impacts from the wind farm can be observed.

Chapter 4

BLASIUS simulations of a wind farm in neutral boundary layers

4.1 Introduction

The literature in chapter 2 gave an overview of numerical modelling work showing the impact of wind farms. The literature can be divided into two categories: large eddy simulations (LES) of turbine wakes which includes their impact on the boundary layer and Reynolds averaged Navier-Stokes equations (RANS) for the larger scale impacts of wind farms, for example in climate modelling.

The stability of the atmospheric boundary layer changes during the day, with stable and neutral being two of the states it can be in. Disturbances to the boundary layer flow have the potential to propagate large distances from their source, especially in stable conditions. These disturbances can have a significant impact on the boundary layer, producing interesting meteorological features such as downslope winds on the lee side of hills. The inclusion of a wind farm in the atmospheric boundary layer decreases the velocity whilst increasing the turbulence. It is not currently known what impact this has on the atmospheric boundary layer.

The majority of work aimed at understanding this has been conducted in LES. This has the advantage of accurately simulating the small-scale turbulence from the turbines. The main focus of these studies has been looking at the boundary layer impact on the wind farm, and more importantly the power output. It is

important to understand these impacts, especially for wind power engineering, however this is missing half of the story. Calaf *et al.* (2010) used LES with a finite wind farm and found that the vertical fluxes of kinetic energy are proportional to the power extracted by the turbines. The wider scale impacts of these changes were not observed. Further large eddy simulations have looked at how different neutral boundary layers impact the power production. Allaerts & Meyers (2015) modelled a neutral boundary layer in an LES with varying boundary layer height and capping inversion strength. It was found that increasing the boundary layer height from 500 m to 1500 m led to a $31\% \pm 0.4\%$ increase in power. Similarly, a $13\% \pm 0.2\%$ power increase occurred when the inversion layer strength increased from 2.5 K to 10 K. Some work has looked at the wind farm impacts, but only within the wind farm area. The effects of boundary layer stability on wind farm velocity deficits and 3-d wake structure was carried out in Abkar & Porte-Agel (2015), although this was once again focussed on wind farm power.

Although some work has been done to quantify the impact of wind farms on the boundary layer in RANS, lacking from the literature is a comprehensive summary of wind farm effects on the boundary layer. Fitch *et al.* (2013) used mesoscale models to assess the impact of wind farms throughout a diurnal cycle, and hence different atmospheric stability. The increased turbulence in the convective boundary layer suppresses the wind farm wake, caused by the increased mixing. Interestingly, nocturnal low level jets (LLJ's) have the potential to form within the wind farm rotor area. The inclusion of a wind farm eliminates the LLJ's, making a significant change to the boundary layer. Once again, the wider reaching impact from the wind farms were not discussed.

This chapter looks at quantifying the impact from wind farms for different boundary layer structures. This is essential if larger scale impacts are to be derived from RANS. A suite of numerical simulations in BLASIUS are conducted for different boundary layer profiles. These are then used to understand the feedback and response of wind farms on the atmospheric boundary layer. This will be done by looking at dynamical changes around the wind farm and also throughout the rest of the boundary layer. The simulations used cover a range of neutral boundary layer parameters, and the boundary layer response from changing all parameters will be discussed. There will also be a discussion on the effect of changing the size of the wind farm in the boundary layer.

4.2 BLASIUS simulations

Idealised simulations have been carried out in BLASIUS with three key boundary layer parameters altered: the velocity of the air aloft (U), the initialised height of the boundary layer (z_i) and the strength of the capping inversion (θ_i). This produces an idealised boundary layer profile with moist air processes and surface heat fluxes excluded. Other parameters such as surface roughness, z_0, and buoyancy frequency above the boundary layer, N, affect the structure of the boundary layer however these three have been chosen as they have the greatest impact on the formation of the boundary layer and will provide a general understanding of boundary layer effects from a wind farm.

Simulations are limited to 2-d with periodic lateral boundary conditions. To avoid wrap around effects a large 400 km domain with 1 km horizontal resolution is used. The vertical domain spans 15 km with the resolution determined by a stretched grid, with $\mathrm{d}z = 10.5\,\mathrm{m}$ at the surface and increasing to $\mathrm{d}z = 567\,\mathrm{m}$ at 6488 m height, at which point $\mathrm{d}z$ remains constant. A 6 km Rayleigh damping layer is prescribed at the top of the domain with a damping coefficient of $k = 0.002$. The damping coefficients $R(z)$ are dependent on the domain height, and are calculated by

$$R(z) = k\left(1 - \pi\left[\frac{z - z_b}{z_t - z_b}\right]\right)^{\frac{1}{5}}$$

where z_b and z_t are the bottom and top heights of the damping layer. Model variables are then adjusted according to the damping coefficient R. This is a necessary step to avoid the reflection of upward propagating waves back in the domain. The flow is driven by a geostrophic wind U and corresponding pressure gradient in the y direction. The Coriolis parameter $f = 0.0001\,\mathrm{s}^{-1}$ and the lower surface uses no-slip boundary conditions. Turbulence is parametrised by a $1\frac{1}{2}$ closure scheme as described in section 3.1.

The simulations are initialised with a neutral boundary layer up to height z_i and capped by a temperature inversion θ_i. Above the boundary layer is a stable layer with $N = 0.01\,\mathrm{s}^{-1}$, an example of which is shown in figure 4.1. The initialisation occurs in a 1-d BLASIUS simulation with the output used to setup the 2-d simulation. The 1-d run is also used to determine the boundary layer statistics which will be described later.

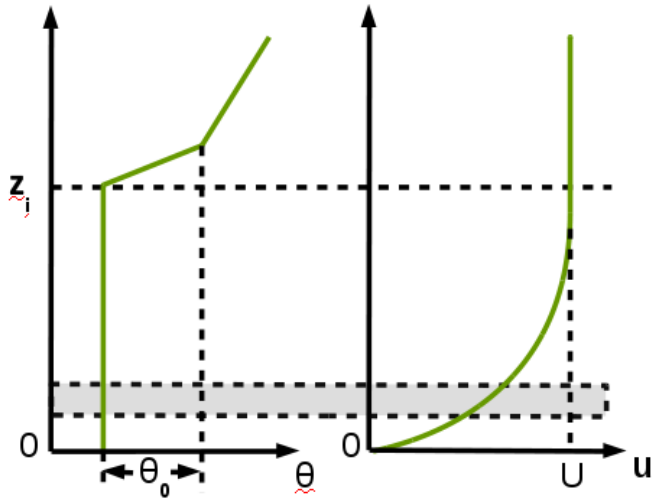

Figure 4.1: *Schematics of the potential temperature and horizontal velocity profiles from the 1-d BLASIUS simulations. The boundary layer height is shown by z_i with the strength of the inversion given by θ_i. The velocity profiles follow a logarithmic profile until the geostrophic wind speed U is reached. The grey shaded area represents the turbine rotor area.*

Wind turbines are parametrised in the 2-d BLASIUS simulation by the scheme in section 3.3. Each simulation contains a wind farm consisting of 20 turbines located in consecutive grid cells in the centre of the domain. The wind farm simulated is therefore on the larger side compared to modern wind farms however with a lower turbine density. The periodic boundary condition implies that an infinite wind farm is modelled in the y direction. Each turbine has a hub height of 95 m and a rotor diameter $D = 100$ m. A deviation from the parametrisation in section 3.3 is that the drag coefficient of the turbines is constant with $C_D = 0.5$. This is done so there is some consistency in the turbine drag between simulations. The value is representative of the drag coefficient from turbines with an upstream velocity of $\approx 7\,\mathrm{m\,s^{-1}}$, which test simulations showed was the average velocity at turbine hub height.

The parameters of interest, U, z_i and θ_i, are altered between simulations. All are initialised in the 1-d run with z_i and θ_i recalculated from the 1-d run in order to allow for changes due to the model spin up. This analysis used both the boundary velocity and that of the air aloft. Using both velocities allows a comparison between simulations where the boundary layer velocities differ but the air aloft is of a similar velocity.

$$\bar{u}_0 = \frac{1}{z_i} \int_0^{z_i} u_0(z) \mathrm{d}z. \tag{4.1}$$

Using these statistics the non-dimensional parameters used in the study can be defined as:

$$Fr = \frac{\bar{u}_0}{\sqrt{z_i g'}}, \qquad Z = \frac{N z_i}{U}, \tag{4.2}$$

where $g' = g\theta_i/\theta_0$ is the reduced gravity term. Both of these non-dimensional parameters quantify independent dynamical properties of the flow. Fr is the ratio of the upstream flow velocity to the speed of propagating waves on the inversion. Z is the ratio of inversion height to the wavelength of vertically propagating waves in the air aloft. These parameters have been used in Vosper (2004) to investigate mountain lee waves in BLASIUS. The boundary layer height is defined as the bottom of the inversion layer. This is set to a model level, even though the initialised boundary layer height could be higher. The value of θ_i is then the change in θ over the same model level. The full set of BLASIUS simulations are shown in table 4.1. A range of geostrophic wind speeds, temperature inversions and initialised boundary layer heights are used in order to capture a variety of boundary layer scenarios. The lowest boundary layer height simulated is $z_i = 452\,\mathrm{m}$. Two simulations use this boundary layer height, $Fr = 1.071$ and $Fr = 1.65$ and in both cases the simulations are limited by the numerical modelling. This was a result of some wrap around effects in the simulations. Efforts were made to minimise this by running a larger horizontal domain and adding in Rayleigh damping into the horizontal boundary conditions. Neither changes removed the wrap around effects, and instead compromised simulation performance. For this reason, lower boundary layer heights are not simulated. Some simulations in table 4.1 are not covered in detail in this chapter, although they are used in chapter 5. During this analysis, the Froude number will be used to identify each BLASIUS simulation. This is done due to the uniqueness of Fr.

Each 2-d simulation is run for $75,000$ seconds, at which point the flow has advected through 1.5 domain widths. Although the wind farm wake has reached a steady state, there are small velocity fluctuations within the boundary layer. Figure 4.2 shows the evolution of the velocity perturbation within the wind farm area for selected simulations. Most simulations, notably cases $Fr = 0.6$ and $Fr = 0.74$, show velocity increases within the boundary layer at $t = 45,000$

Fr	Z	$\bar{u}_0\,(\mathrm{m\,s^{-1}})$	$\theta_i\,(\mathrm{K})$	$z_i\,(\mathrm{m})$	$U\,(\mathrm{m\,s^{-1}})$	$u_*\,(\mathrm{m\,s^{-1}})$
0.6	1.71	7.1	3.04	1364	8	0.32
0.74	1.36	8.8	3.04	1364	10	0.38
0.8	0.60	8.9	5.1	715	12	0.44
0.87	1.14	10.4	3.04	1364	12	0.44
0.92	0.83	9.7	3.31	992	12	0.44
1.02	0.60	8.9	3.1	715	12	0.44
1.06	1.14	10.4	2.04	1364	12	0.44
1.07	0.91	12.7	3.04	1364	15	0.53
1.071	0.38	7.3	3.02	452	12	0.43
1.26	1.36	8.8	1.04	1364	10	0.38
1.46	0.72	7.7	1.14	715	10	0.38
1.49	1.14	10.4	1.04	1364	12	0.44
1.65	0.45	6.4	0.99	452	10	0.37
1.69	0.60	8.9	1.14	715	12	0.44

Table 4.1: *Key parameters from the 1-d BLASIUS simulations. Fr is used throughout this analysis to identify each model simulation.*

seconds. This then decreases by the end of the simulation time. To reduce any time dependency on the flow statistics, the simulations are time averaged between $t = 60,000$ seconds and $t = 75,000$ seconds. Within this time frame there is little change in the velocity in most cases and hence this captures the fully evolved wind farm impacts. It should be noted that the case $Fr = 1.071$ displays an increase in the boundary layer height, figure 4.2(d), within this time average period.

4.3 Dynamics from a fixed wind farm

4.3.1 Hub height velocity

The velocity deficits for each simulation, calculated by eqn. 2.9, are shown in figure 4.3. Plotted also is the velocity deficit power law in eqn 2.10 from Aitken *et al.* (2014). Within the wind farms a maximum velocity deficit of 11% is observed

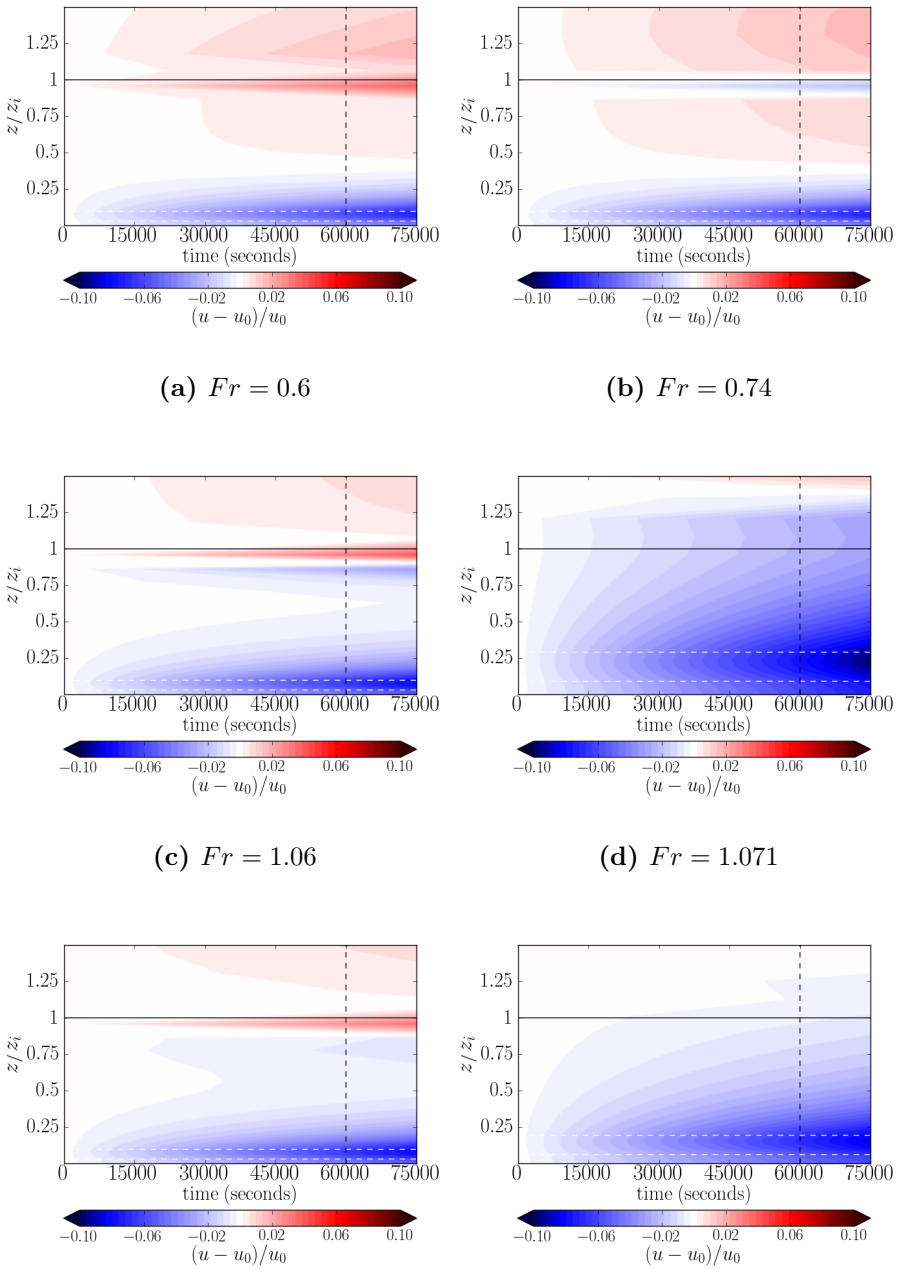

(a) $Fr = 0.6$ **(b)** $Fr = 0.74$

(c) $Fr = 1.06$ **(d)** $Fr = 1.071$

(e) $Fr = 1.49$ **(f)** $Fr = 1.69$

Figure 4.2: *The evolution of the space average velocity within the wind farm is shown for the full* $75,000$ *seconds BLASIUS simulation time. The wind farm rotor area is shown by the horizontal dotted lines and the initialised boundary layer height is given by the solid black line. The time average in the analysis is taken from the final* $15,000$ *seconds, represented by the dotted vertical line.*

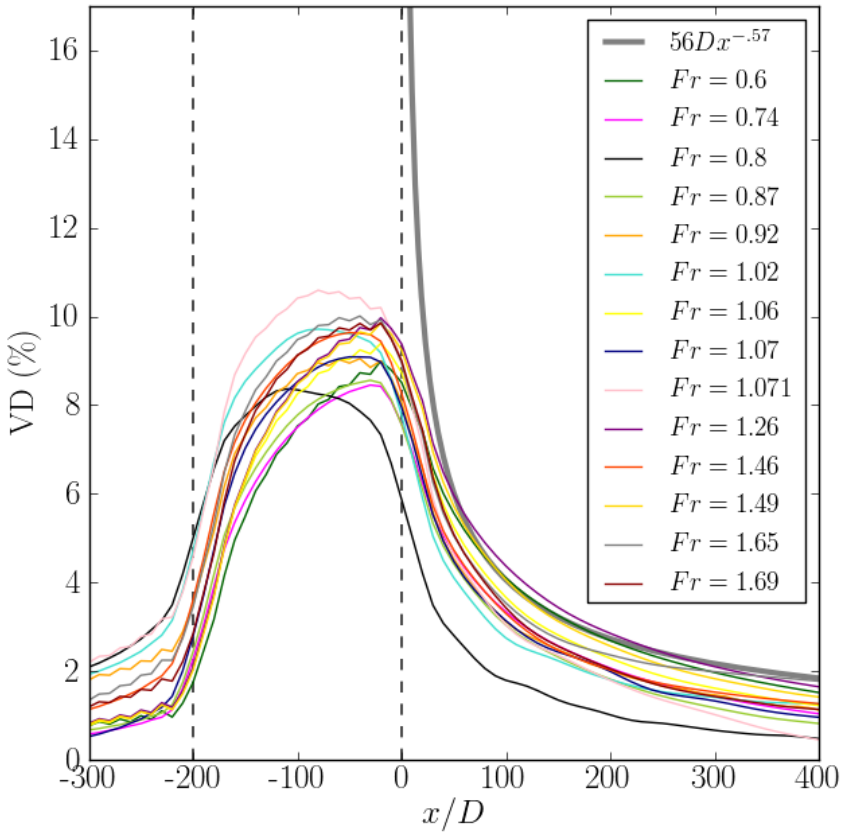

Figure 4.3: *For each BLASIUS simulation the hub height velocity deficit is calculated. The dotted lines show the wind farm area. Also plotted is the velocity deficit power law, represented as the bold grey line. The x-axis is normalised with the rotor diameter D, with $x/D = 0$ being the downstream edge of the wind farm.*

in $Fr = 1.071$, with a range of $8\% - 11\%$, similar to the results in Christiansen & Hasager (2005). This simulation $Fr = 1.071$ was initialised with the lowest z_i and greatest u_0. Of interest in figure 4.3 is the downstream wind farm wake. With the exception of $Fr = 0.8$, all simulations show the same velocity deficit decay. Comparing to the power law, on the downstream edge of the wind farm there is a large difference with the BLASIUS data. Although not plotted, at 100 m downstream the velocity deficit is estimated to be 56%. At a distance of $50D$ downstream, the BLASIUS hub height velocity deficit and the power law converge, evidence that the power law is an accurate measure for hub height velocity. The large difference between the two on the downstream edge of the

wind farm is a result of the resolution in BLASIUS. Furthermore the power law is calculated at a distance of $1D$ downstream of a turbine. Here we assume that the final turbine in the array is on the downward edge, whereas the BLASIUS parametrisation is distributing the same drag force over the final 1 km of the array. Taking that into account, any changes in the position that the power law is calculated at would still fall within the range of velocity deficits from BLASIUS.

4.3.2 Boundary layer displacement

Another impact from the wind farm on the boundary layer is a displacement of the inversion layer. In order to compensate for the velocity reduction caused by the wind farm, mass conservation dictates that the height of the flow must increase and thus the boundary layer is displaced. To measure the boundary layer displacement, an isentrope is plotted at the point where the potential temperature increases from the boundary layer reference value, which in these simulations is $\theta_0 = 288.15\,\mathrm{K}$. The isentrope is calculated from the time averaged flow and hence captures the steady state of the inversion layer. From this, the boundary layer displacement, η, can be calculated. This is done by taking the difference between the maximum height of the boundary layer over the wind farm area and the average boundary layer height from the most westerly 50 km of the domain. At 50 km the boundary layer heights have stabilised from the growth caused by the wind farms. The boundary layer change is then normalised with the initialised z_i. Table 4.2 shows the values of η/z_i, referenced by Fr.

Fr	0.6	0.74	0.8	0.87	0.92	1.02	1.06
η/z_i	0.0013	0.0035	0.0027	0.0062	0.0058	0.0064	0.0076
Fr	1.07	1.071	1.26	1.46	1.49	1.65	1.69
η/z_i	0.0080	0.12	0.0064	0.013	0.0064	0.0040	0.0080

Table 4.2: *The average boundary layer inversion displacement, η/z_i, from the final $15,000$ seconds of the simulation.*

The changes of η/z_i with Fr (figure 4.4a) show that for subcritical flow there is an increase in displacement as Fr increases. There is some sign that this continues with the supercritical flow, however simulations $Fr = 1.69$, $Fr = 1.65$ and $Fr = 1.49$ show smaller than expected η/z_i. This is due to the weaker inversion layer, where $\theta_i \approx 1\,\mathrm{K}$. The subcritical simulations have $\theta_i > 2\,\mathrm{K}$ which

shows that for consistent changes in η/z_i, the inversion layer must be at least 2 K. For inversion strengths less than this, the inversion layer is less robust and more sensitive to flow perturbations.

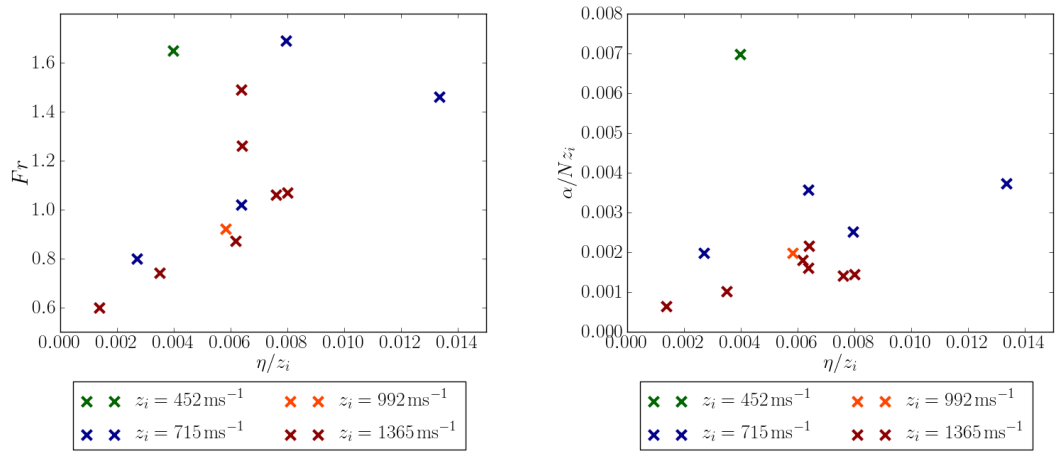

(a) **(b)**

Figure 4.4: *Boundary layer displacement is plotted in relation to (a) Fr and (b) the amplitude of wave aloft (α/Nz_i). The plots are divided according to z_i. These plots do not contain the displacement from the simulation $Fr = 1.071$.*

By treating the displacement from $\theta_i \approx 1$ K with caution, it can be seen that for a fixed z_i, η/z_i increases linearly with Fr. This is expected as these increases in Fr are a result of increasing $\bar{u}_0$ and thus the stronger flow results in a greater inversion displacement. Although there are issues with $\theta_i \approx 1$ K, it is still appropriate to use Fr.

A consequence of the inversion displacement is the generation of waves in the stable air aloft. The amplitude of these waves is calculated by $\alpha = (w_{max} + |w_{min}|)/2$ where w_{max} and w_{min} are the maximum and minimum velocities at the first peak and trough. Figure 4.4(b) shows that an increase in inversion displacement results in a larger amplitude. Considering the stratification is the same between these simulations this is not surprising. A further feature of these waves is the wavelength λ. To calculate λ, the locations of the maximum and minimum vertical velocity values in the air aloft are found. The non-dimensional parameter Z is proportional to z_i/λ, as shown in figure 4.5. Z is the ratio of inversion height with the wavelength of waves, approximated here as U/N. This

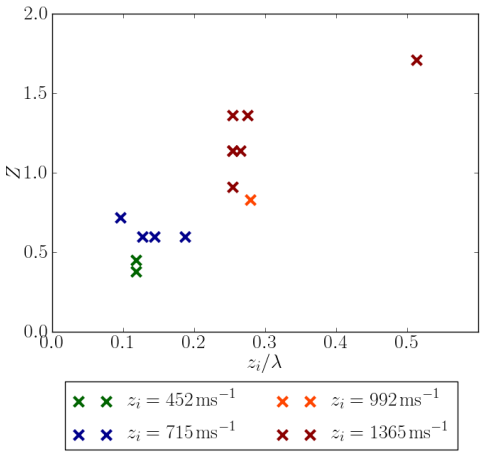

Figure 4.5: *The wavelength of waves in the air aloft (λ) is compared against the non-dimensional parameter $Z = Nz_i/U$. The wavelength is normalised by z_i so that it can be compared to Z.*

shows that Z is a suitable parameter to assess the impact of these waves on the flow.

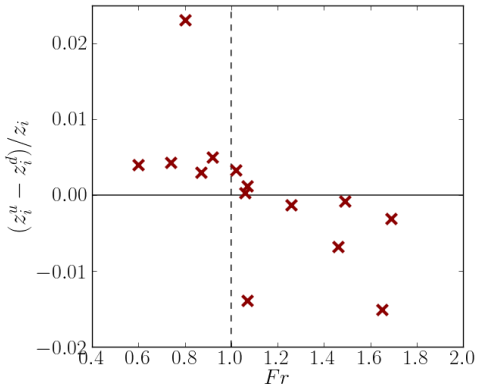

Figure 4.6: *Difference in boundary layer height along the length of the wind farm. The upstream boundary layer height is given as z_i^u and z_i^d is the downstream boundary layer height. The dotted line is at $Fr = 1$, showing the change from subcritical flow to supercritical flow.*

One detail of the boundary layer not captured by η is the change in boundary layer height over the length of the wind farm. The boundary layer height level with the upstream edge of the wind farm is given by z_i^u and the height at the downstream edge if z_i^d. Figure 4.6 shows the difference with respect to Fr. It

shows that for $Fr < 1$ there is a decrease in boundary layer height over the wind farm. This is similar to hydraulic jumps associated with orographic flow, however of a smaller magnitude. When $Fr \gg 1$ there is an increase in the boundary layer. Simulations $Fr = 1.02$, $Fr = 1.06$ and $Fr = 1.07$ have a decrease in boundary layer height, showing some uncertainty in the definition of Fr around $Fr = 1$. When $Fr = 1.071$ there is an increase in boundary layer height. It has already been mentioned that this simulation showed large variability in the boundary layer height. The transition from sub-critical flow to supercritical flow causes changes to the boundary layer height over the wind farm. This is caused by the stronger supercritical flow producing a larger inversion displacement, compared to the relatively weaker flow associated with sub-critical flow.

It would be expected that flow over an obstacle in a neutral boundary layer would produce gravity waves along the inversion layer. This analysis is concerned with the steady state flow so only standing waves are possible. By analysing the boundary layer displacement, downstream waves were only observed in $Fr = 0.8$, $Fr = 1.06$ and $Fr = 1.07$ simulations. Even though simulations were conducted with the aim of waves being generated, their lack of occurrence means it is not possible to understand their formation and statistics. One thing that can be determined is that the waves have a small amplitude and are unlikely to be large enough to be observed in the real atmosphere.

4.3.3 Wind farm induced pressure perturbations

The velocity decrease caused by a wind farm results in a pressure increase on the upstream edge. To assess the range of any pressure changes, the wind farm induced pressure perturbation is plotted in figure 4.7. BLASIUS outputs a pressure perturbation p where the total pressure is given by $p_{tot} = p_0 + p$. Here p_0 is the steady state hydrostatic pressure which is derived from the 1-d run. During the simulations, the boundary layer height evolves, resulting in changes to p. This work is concerned with the changes from wind farms, hence it is important to remove these boundary layer height pressure perturbations. The wind farm induced pressure perturbation, p' is defined as

$$p'(x,z) = p(x,z) - \tilde{p}(z) \quad \text{where } \tilde{p}(z) = \frac{1}{X}\int_X p(x,z)\,\mathrm{d}x. \tag{4.3}$$

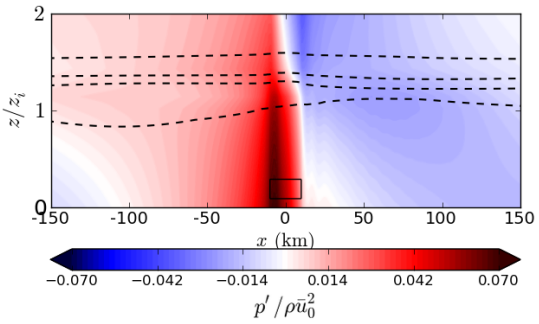

(a)

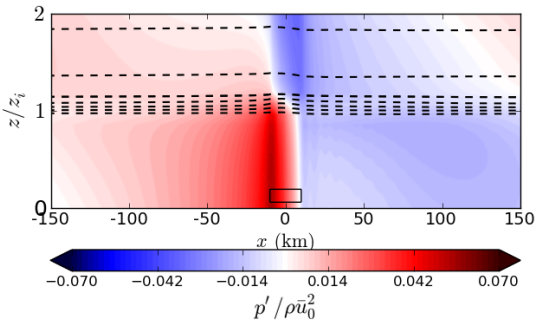

(b)

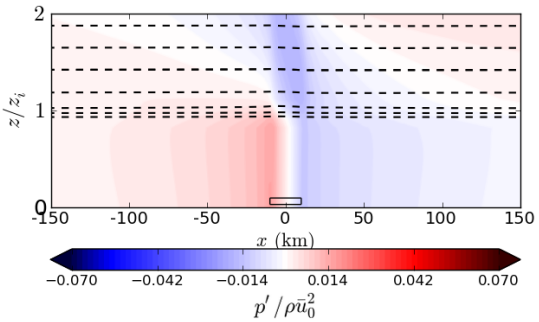

(c)

Figure 4.7: *Pressure perturbation contours are of one of these forms. Simulations with $z_i = 452\,\mathrm{m}$ are of the forms shown in (a). This contour plot represents the $Fr = 1.071$ simulations. When $z_i = 715\,\mathrm{m}$, the pressure perturbations look like (b), which represents the $Fr = 0.8$ run. Finally, simulations with $z_i = 1364\,\mathrm{m}$ have pressure perturbations of the form in (c). This plot shows perturbations from $Fr = 1.07\,\mathrm{m}$. All pressure perturbations are normalised by $\rho\bar{u}_0^2$.*

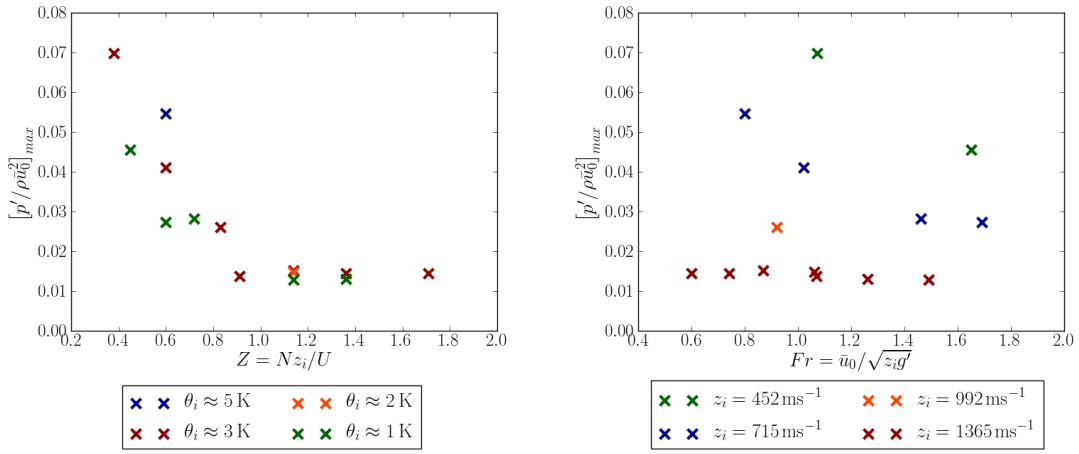

(a) **(b)**

Figure 4.8: *The effect of Z on the maximum wind farm induce pressure perturbation upstream of the wind farm is shown in (a), in addition to the effect of changes to the initialised capping inversion strength θ_i. Figure (b) shows the impact of Fr on the pressure perturbation, this time isolating the effect of changes to z_i.*

Here, X is the total length of the domain. The contour plots of the wind farm pressure perturbations are dependent on z_i. For $z_i = 1364\,\mathrm{m}$, the pressure perturbations both upstream and downstream are uniform throughout the boundary layer, as shown in figure 4.7(c). The uniform nature of the perturbation decreases as z_i decreases. For example, when $z_i = 715\,\mathrm{m}$ the pressure perturbations upstream decrease with height within the boundary layer (figure 4.7(b)). The pressure perturbation downstream of the wind farm is greater (less negative) near the surface compared to the top of the boundary layer. These features become more prominent when $z_i = 452\,\mathrm{m}$ as shown by figure 4.7(a). Upstream of the wind farm there is a decrease in pressure, attributed to the deflections of the isentropes at the top of the boundary layer. These deflections only occur in this simulation and will be discussed in section 4.3.6. The different pressure perturbation regimes are caused by the changes in boundary layer height, and more specifically the ratio with the wind farm hub height. This is brought about by the interaction of the wind farm wake with the boundary layer.

As shown in figure 4.7, the magnitude of the wind farm pressure perturbation differs between simulations. The relationship between the pressure perturbation

and the non-dimensional parameters Z and Fr are shown in figure 4.8. An increase in Z coincides with a decrease in the maximum pressure perturbation upstream of the wind farm. For $Z \geq 0.91$ there is little change in the maximum pressure perturbations. These simulations have $z_i = 1364\,\text{m}$. Changes in θ_i make little difference to $p'/\rho\bar{u}_0^2$ showing that for larger boundary layers the capping inversion strength has little effect on the flow. This idea will be explored in further detail in section 4.3.5. For $Z < 0.91$ there is greater dependency on θ_i, with a greater pressure perturbation being caused by a stronger capping inversion. A stronger capping inversion restricts the boundary layer flow, acting like a rigid lid.

The effect of Fr changes are shown in figure 4.8(b). Once again the simulations behave differently depending on the initialised boundary layer height z_i. For $z_i = 1364\,\text{m}$, there is no dependence on Fr. When $z_i = 715\,\text{m}$, $p'/\rho\bar{u}_0^2$ decreases when Fr increases, a trait that also occurs when $z_i = 452\,\text{m}$. The rate at which $p'/\rho\bar{u}_0^2$ decreases changes for different z_i, although there are insufficient results to quantify this. When Fr is small, the wind farm acts like a blocking mechanism for the flow. This results in a larger pressure perturbation and increases the likelihood of waves propagating upstream along the boundary layer inversion. The independence of $p'/\rho\bar{u}_0^2$ on Fr for $z_i = 1364\,\text{m}$ implies that waves of this nature are unlikely; the perturbations caused by the wind farm decrease sufficiently by the time they reach the top of the boundary layer. When z_i decreases then perturbations caused by the wind farm have a greater effect on the capping inversion and hence upward propagating waves are more likely.

The wind farm induced pressure perturbation is dependent on Z and θ_i, with some dependence on Fr. Low Z values imply that there with be a greater pressure perturbation which is caused by the decrease in z_i. Increasing θ_i has a further increase on the pressure perturbation as the boundary layer flow is constrained by the rigid lid nature of the capping inversion. There is a small effect from Fr, where increases in Fr decrease the pressure perturbation. Larger values of Fr imply that the flow is strong enough to flow through the wind farm at a greater rate, reducing the velocity deficit and hence the pressure perturbations. This is in comparison to smaller Fr flow which has a greater decrease in velocity because of the weaker flow behaviour.

4.3.4 Wind speed on the wind farm wake

Simulations $Fr = 0.6$, 0.74, 0.87 and 1.07 are initialised with $z_i = 1364\,\mathrm{m}$ and $\theta_i = 3.04\,\mathrm{K}$. The geostrophic velocities, U, are 8, 10, 12 and $15\,\mathrm{m\,s^{-1}}$ resulting in $\bar{u}_0 = 7.1$, 8.8 10.4 and $12.7\,\mathrm{m\,s^{-1}}$. The velocity perturbation fields in figure 4.9 show a velocity decrease downstream of the wind farm. There is a further decrease upstream of the wind farm, a result of the upstream pressure increases.

The flow regime changes as $\bar{u}_0$ increases. There is a decrease in the upstream and downstream wakes as $\bar{u}_0$ increases. The velocity changes on the boundary layer interface are also subject to change, with a velocity increase for $\bar{u}_0 = 7.1\,\mathrm{m\,s^{-1}}$ compared to a velocity decrease in $\bar{u}_0 = 10.4\,\mathrm{m\,s^{-1}}$. When $\bar{u}_0 = 12.7\,\mathrm{m\,s^{-1}}$ there is an area of increased velocity within the boundary layer above the wind farm area. This area increases its horizontal extent as $\bar{u}_0$ decreases and increases in relative magnitude. Taking into account mass conservation, the velocity decrease within the wind farm must lead to an increased velocity above it for a fixed boundary layer height. Case $\bar{u}_0 = 7.1\,\mathrm{m\,s^{-1}}$ has the greatest relative velocity decrease at hub height, figure 4.3 , and hence has the greater velocity increase above. An increase in $\bar{u}_0$ causes the velocity decreases upstream and downstream to be reduced compared to the low $\bar{u}_0$ flows. There is a greater vertical extent of the wake, which is initiated at the front of the wind farm. The increase in $\bar{u}_0$ in the supercritical flow, and hence greater hub height velocity, induces a greater vertical velocity at the front edge of the wind farm. This can be seen from the increase in $w/\bar{u}_0$ between figure 4.10(d) and figure 4.10(a). In all simulations in figure 4.10, there is an increase in the vertical velocity at the front of the wind farms and a decrease on the downwind edge of the farm. This pattern occurs irrespective of $\bar{u}_0$ with the only difference being the magnitude of vertical velocity changes. This manifests as an increase in the interaction between the turbine wake and the boundary layer interface causing a larger inversion displacement. From table 4.2 it can be seen that η/z_i increases as $\bar{u}_0$ increases showing that a stronger boundary layer velocity increases the vertical growth of the boundary layer.

In addition to a turbine drag, the wind farm parametrisation increases the turbulent kinetic energy (TKE) within the wind farm area. Figure 4.11 shows the boundary layer TKE as a result of the wind farm, and due to the increase in boundary layer velocity between the cases, is normalised against the surface friction velocity u_*^2, which is calculated from the 1-d run. Within the wind farm area

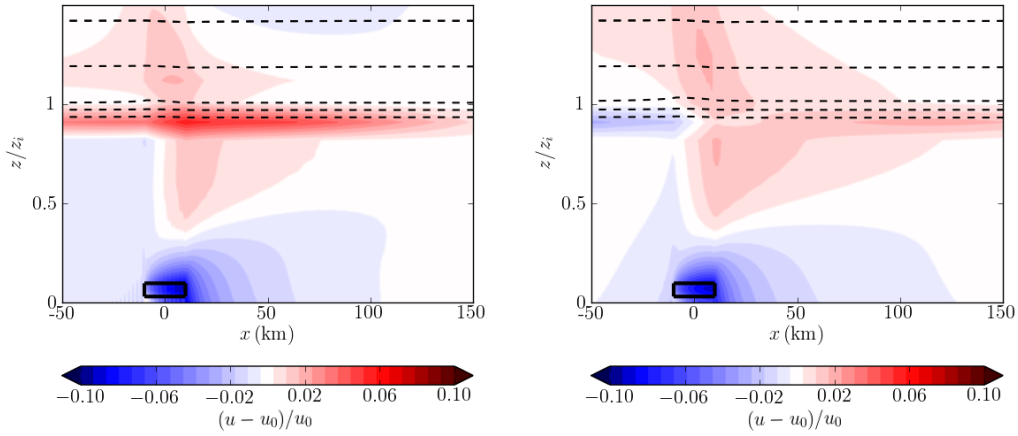

(a) $Fr = 0.6$, $\bar{u}_0 = 7.1\,\mathrm{m\,s^{-1}}$ **(b)** $Fr = 0.74$, $\bar{u}_0 = 8.8\,\mathrm{m\,s^{-1}}$

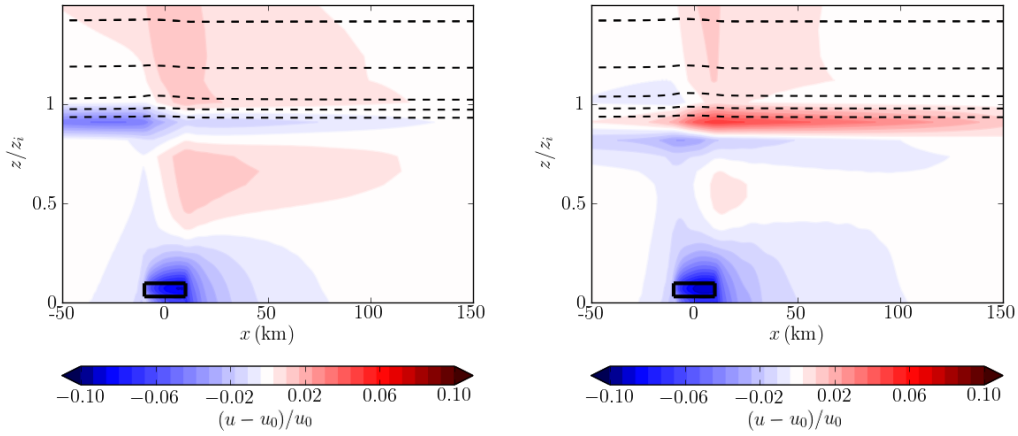

(c) $Fr = 0.87$, $\bar{u}_0 = 10.4\,\mathrm{m\,s^{-1}}$ **(d)** $Fr = 1.07$, $\bar{u}_0 = 12.7\,\mathrm{m\,s^{-1}}$

Figure 4.9: *Coloured contours show the normalised velocity perturbation field within and just above the boundary layer. The dotted lines show constant potential temperature, with* 1 K *between each line. The wind farm rotor area is shown as the black box. The plots are for different simulations,where* $\bar{u}_0 = 7.1,\ 8.8\ 10.4 \,\mathrm{and}\, 12.7\,\mathrm{m\,s^{-1}}$ *for plots (a,b,c and d) respectively.*

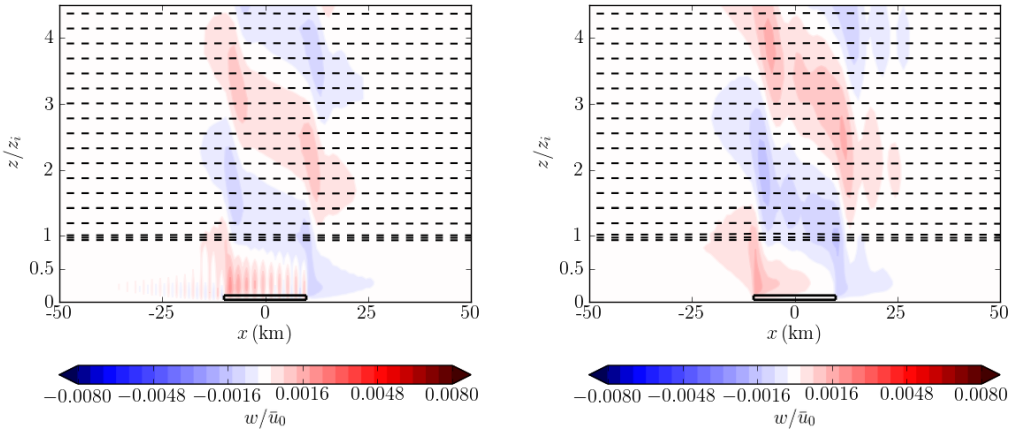

(a) $Fr = 0.6$ **(b)** $Fr = 0.74$

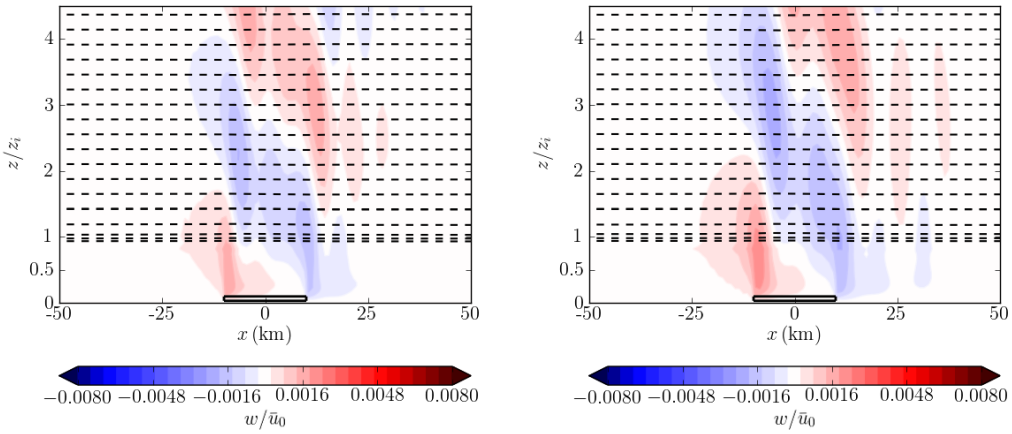

(c) $Fr = 0.87$ **(d)** $Fr = 1.07$

Figure 4.10: *As described in figure 4.9 except showing the vertical velocity w. The velocity is normalised with the boundary layer velocity $\bar{u}_0$. In these plots a greater area of the simulated domain is shown above the boundary layer.*

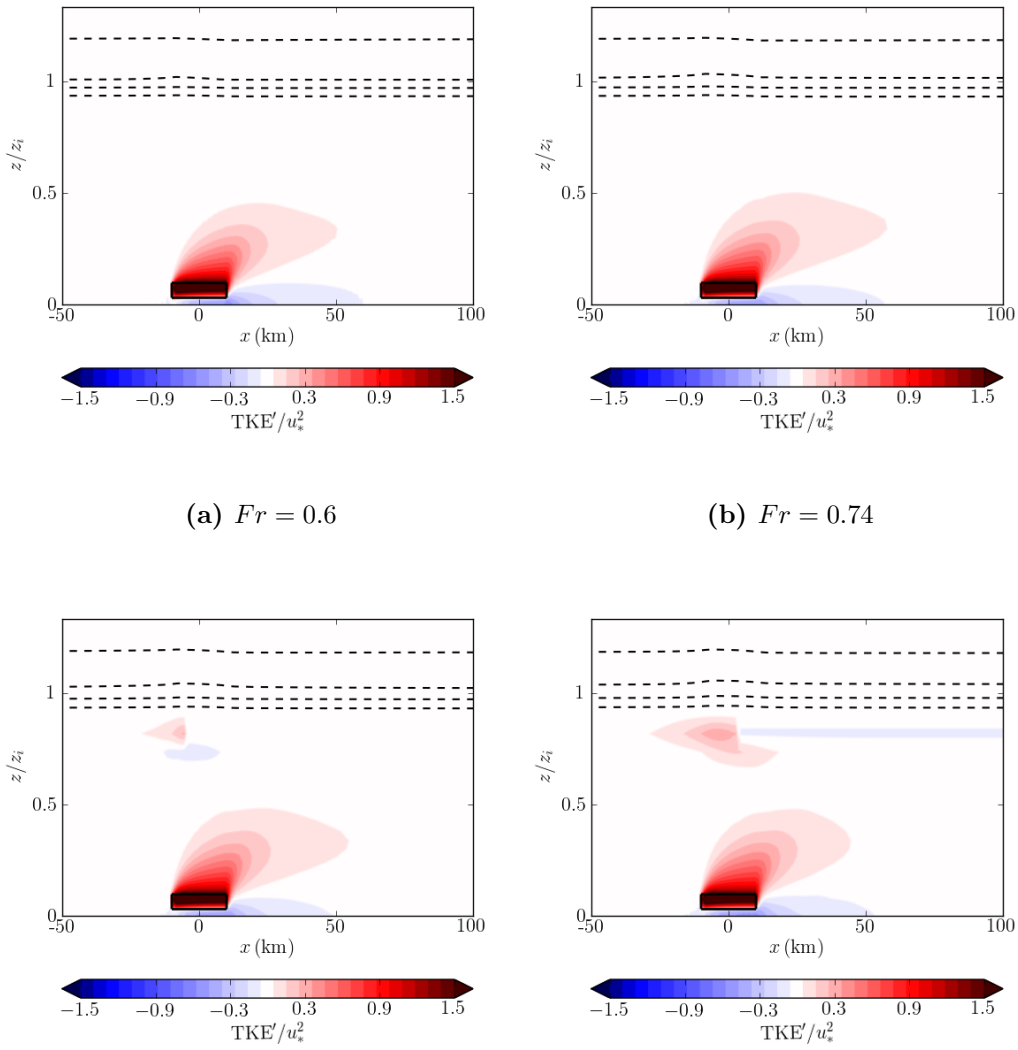

(a) $Fr = 0.6$ **(b)** $Fr = 0.74$

(c) $Fr = 0.87$ **(d)** $Fr = 1.07$

Figure 4.11: *As shown in figure 4.9 but for TKE perturbations normalised with the friction velocity u_*^2.*

and in the upper portion of the wind farm wake, there is an increase in the levels of TKE. The lower portion of the wake shows a decrease in the TKE, a result of the decrease in velocity from the wind farm. The magnitude of the TKE in the wake is constant between the cases, showing that changes to the TKE term are a result of the upstream velocity magnitude. Figure 4.11(d) has an area of increased TKE at the top of the boundary layer, the area where there is the greatest change in velocity.

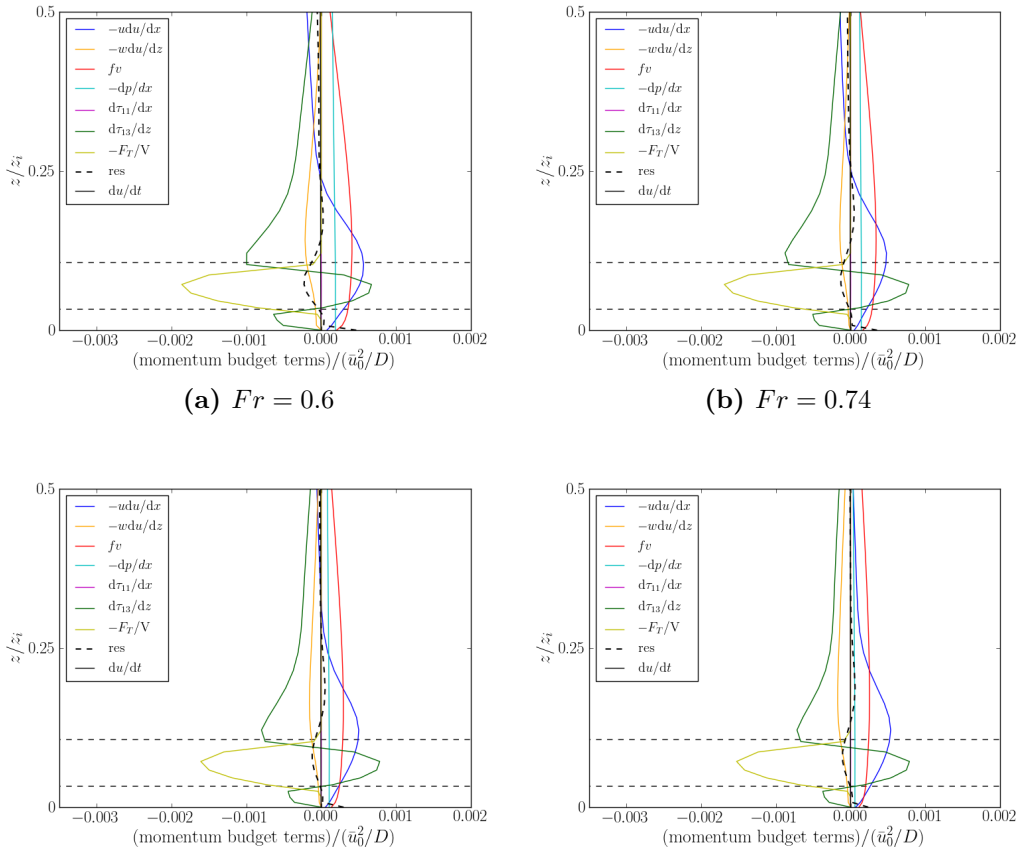

(a) $Fr = 0.6$ **(b)** $Fr = 0.74$

(c) $Fr = 0.87$ **(d)** $Fr = 1.07$

Figure 4.12: *The momentum budget is shown for each simulation at the front edge of the wind farm. The* du/dt *is calculated from the BLASIUS simulations, with 'res' showing the residual from the other momentum terms. Only the lowest part of the boundary layer is shown. The wind farm rotor area is shown as the dotted lines.*

To further understand the dynamics around the wind farm, a momentum budget

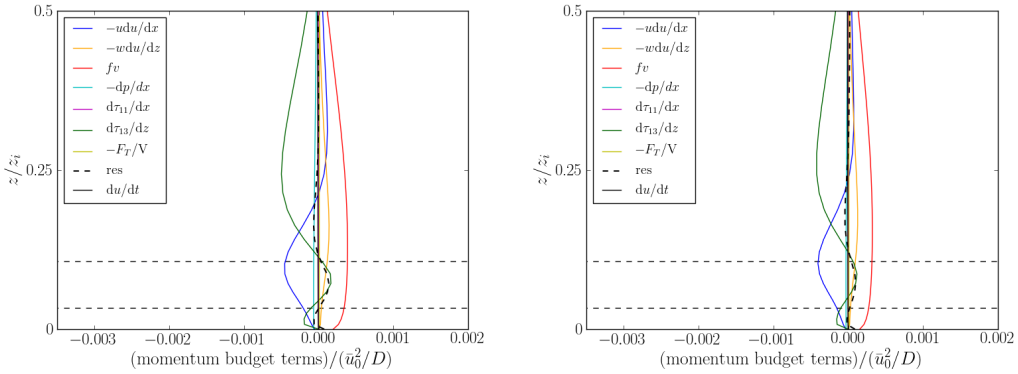

(a) $Fr = 0.6$ **(b)** $Fr = 0.74$

(c) $Fr = 0.87$ **(d)** $Fr = 1.07$

Figure 4.13: *As for 4.12 however showing the momentum budget terms on the downstream edge of the wind farms*

analysis is carried out. The 2-d horizontal momentum equation is

$$\frac{\partial u}{\partial t} = -u\frac{\partial u}{\partial x} - w\frac{\partial u}{\partial z} + fv - \frac{\partial p}{\partial x} + \frac{\partial \tau_{11}}{\partial x} + \frac{\partial \tau_{13}}{\partial z} - F_T. \tag{4.4}$$

The terms of the momentum equations are calculated from the model diagnostics, where velocity and stress terms are interpolated onto the pressure points of the model. This method of calculating the momentum budget, rather than outputting the terms directly from the model, could lead to errors due to different discretisation schemes. This is expected to be most obvious in the advection terms. At the front of the wind farm, figures 4.12, the turbine drag is balanced by the increase in vertical Reynolds stress $\partial\tau_{13}/\partial z$. From figure 4.14 it can be seen that, as was the case with the TKE contours, figure 4.11, below the wind farm rotor area there is a decrease in τ_{13} and an increase in τ_{13} in the upper part of the wind farm wake. The wind farm area is also characterised by an increase in the deceleration $u\partial u/\partial x$, once again from the turbine drag term. The deceleration continues up to a height of $0.25\,z_i$, with the $Fr = 1.07$ case displaying a smaller magnitude of deceleration up to $0.5\,z_i$. Moreover, above the wind farm there is an increase in the vertical advection of horizontal momentum $w\partial u/\partial z$, which increases as $\bar{u}_0$ increases. In all simulations the effect of Coriolis throughout the boundary layer results in an increase in the vertical Reynolds stress, most apparent between $0.25\,z_i$ and $0.5\,z_i$ where the other terms have reduced in magnitude. The momentum budget at the front of the wind farm shows that as the turbine drag acts on the flow, there is an increase in the Reynolds stress throughout the depth of the wind farm. Above the wind farm there is an increase in vertical transport which advects the turbine deceleration throughout the boundary layer. This is greatest in the $Fr = 1.07$ case where the vertical transport extends to a greater height, hence figure 4.9(d) shows the velocity decrease throughout the boundary layer.

On the downstream edge of the wind farm, the flow is dominated by the occurrence of the wind farm wake, figures 4.13. Within the wind farm rotor area the flow is in a state of horizontal acceleration as shown by the negative $-u\partial u/\partial x$ terms. Above the wind farm area there is a constant level of negative vertical advection of the horizontal momentum, implying that flow is being transported down into the wind farm wake. The maximum vertical Reynolds stress occurs at a height of $0.25\,z_i$, before it decreases to zero around $0.5\,z_i$. There are very small differences in the downstream momentum budget between these simulations. This

shows that the balance of terms caused by changing $\bar{u}_0$ remains that same and hence velocity changes do not have a significant impact on the interaction of the wind farm in the boundary layer.

In the upper half of the boundary layer there is a decrease in τ_{13} in the $Fr = 1.07$ case, figure 4.14(d), the same area where there is a large velocity decrease, figure 4.9(d). This can also be seen with $\bar{u}_0 = 10.4\,\mathrm{m\,s^{-1}}$, figure 4.14(c) and in the horizontal advection term plotted in figure 4.15. For $\bar{u}_0 = 7.1\,\mathrm{m\,s^{-1}}$ there is a small area of deceleration at the front of the wind farm, with the flow accelerating along the length of the wind farm in the upper part of the boundary layer. Contrast this with $\bar{u}_0 = 12.7\,\mathrm{m\,s^{-1}}$, where the deceleration extends to the boundary layer top, with the acceleration layer beginning further along the wind farm length. The cases between show a continuous transition from one regime to the other. Downstream of the wind farm there is acceleration within the wind farm wake.

It has been shown that as $\bar{u}_0$ increases, the horizontal extent of the wind farm wake is reduced, however there is an increase in the vertical extent. There is therefore a greater signal from the wind farm wake throughout the boundary layer in the higher velocity cases. The vertical velocity increases at the front of the wind farm and the downward vertical velocity on the downstream edge of the wind farm also increases in magnitude. This increases the vertical mixing of the wake with the air above, reducing the length of the wake.

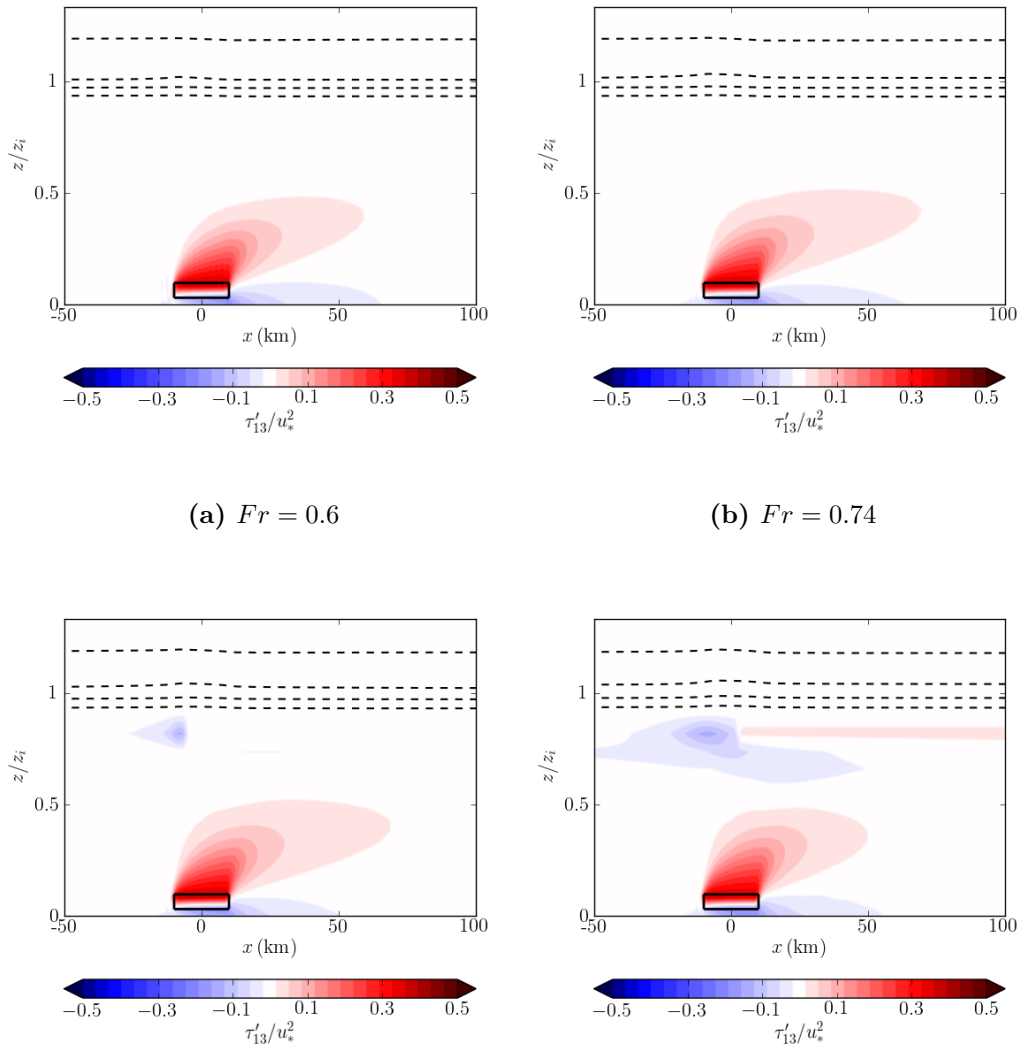

(a) $Fr = 0.6$ **(b)** $Fr = 0.74$

(c) $Fr = 0.87$ **(d)** $Fr = 1.07$

Figure 4.14: *The τ_{13} field is shown for each simulation with different boundary layer velocity. Additional features are the same as on figure 4.9.*

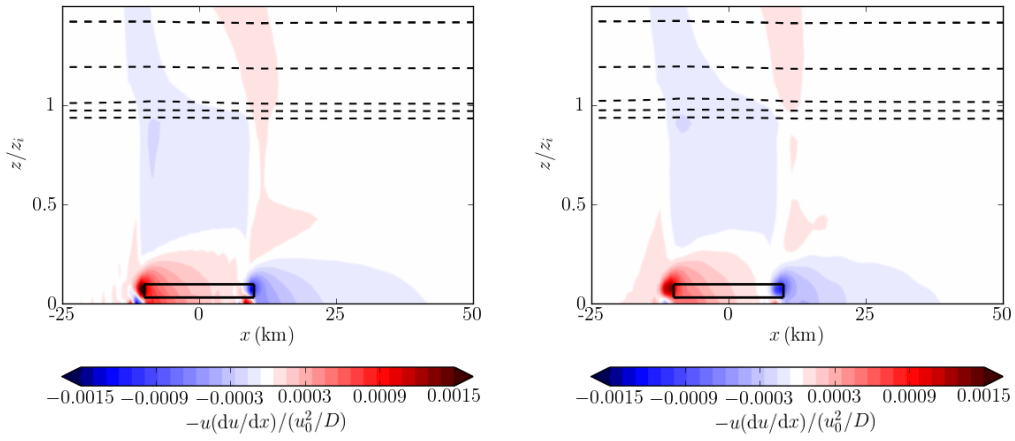

(a) $Fr = 0.6$ **(b)** $Fr = 0.74$

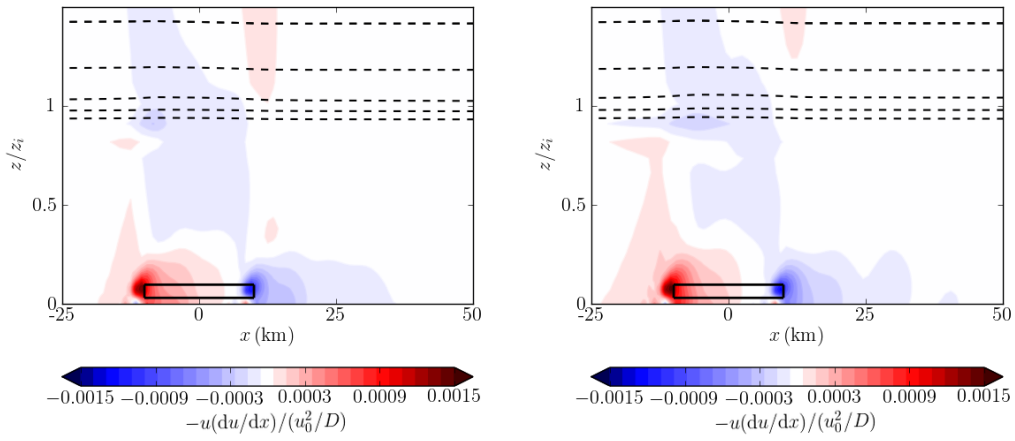

(c) $Fr = 0.87$ **(d)** $Fr = 1.07$

Figure 4.15: *As figure 4.9 showing $u\partial u/\partial x$ normalised with $\bar{u}_0^2/D$.*

4.3.5 The effects of changing the boundary layer capping inversion

To assess the impact of changing θ_i two sets of simulations are considered. The first involves simulations $Fr = 0.8, 1.02$ and 1.69, where $\bar{u}_0 = 8.9\,\mathrm{m\,s^{-1}}$, $z_i = 715\,\mathrm{m}$ and $\theta_i = 5.1\,\mathrm{K}, 3.1\,\mathrm{K}$ and $1.1\,\mathrm{K}$. The second case uses simulations $Fr = 0.87$, 1.06 and 1.49. An increase in U and z_i yields $\bar{u}_0 = 10.4\,\mathrm{m\,s^{-1}}$ and $z_i = 1364\,\mathrm{m}$. The capping inversions are set to $\theta_i = 3\,\mathrm{K}$, $2\,\mathrm{K}$ and $1\,\mathrm{K}$. Although the ranges of $\bar{u}_0$ and θ_i differ between these cases the parameters have been chosen so that the resulting Froude numbers are approximately equal. This enables comparison of both the effect of changes to θ_i and Fr.

The horizontal velocity perturbations are shown in figure 4.16. Firstly, the changes in the wake structure differ between the two cases. With $z_i = 715\,\mathrm{m}$ (figures 4.16(a,b and c)) the wake decreases in length both up and downstream of the wind farm as θ_i decreases. Conversely, figures 4.16(d,e and f) show an increase in the wind farm wake both up and downstream as θ_i decreases. This pattern change is due to the changes in z_i which will be discussed in section 4.3.6.

The vertical velocity in the boundary layer is of the same magnitude between all simulations, figure 4.17, showing that the capping inversion strength does not influence the vertical motion at the front of the wind farm. With $z_i = 715\,\mathrm{m}$ there is an increase in η as θ_i decreases (table 4.2). The stronger capping inversions inhibit boundary layer displacement. The simulation $Fr = 0.8$ has a large decrease in boundary layer height over the wind farm. This contradicts the rigid lid assumption for a large θ_i. One explanation for this is that the changes in boundary layer height over the wind farm are caused by the combination of the turbine drag. The idea being that the velocity decreases upstream of the wind farm in figure 4.16(a) cause a greater vertical extent of the wake for high θ_i, as shown by the more negative $\partial\tau_{13}/\partial z$ in figure 4.19(a). An increase in the wake throughout the boundary layer acts like a blocking mechanism to the flow. Downstream of the wind farm there is then a more negative $\partial\tau_{13}/\partial z$ at $0.5z_i$, a sign that there is an increase in the convergence of turbulent momentum flux, as also seen in figure 4.18(a). This then results in a sudden boundary layer decrease as the flow adjusts to the effects of the turbine drag.

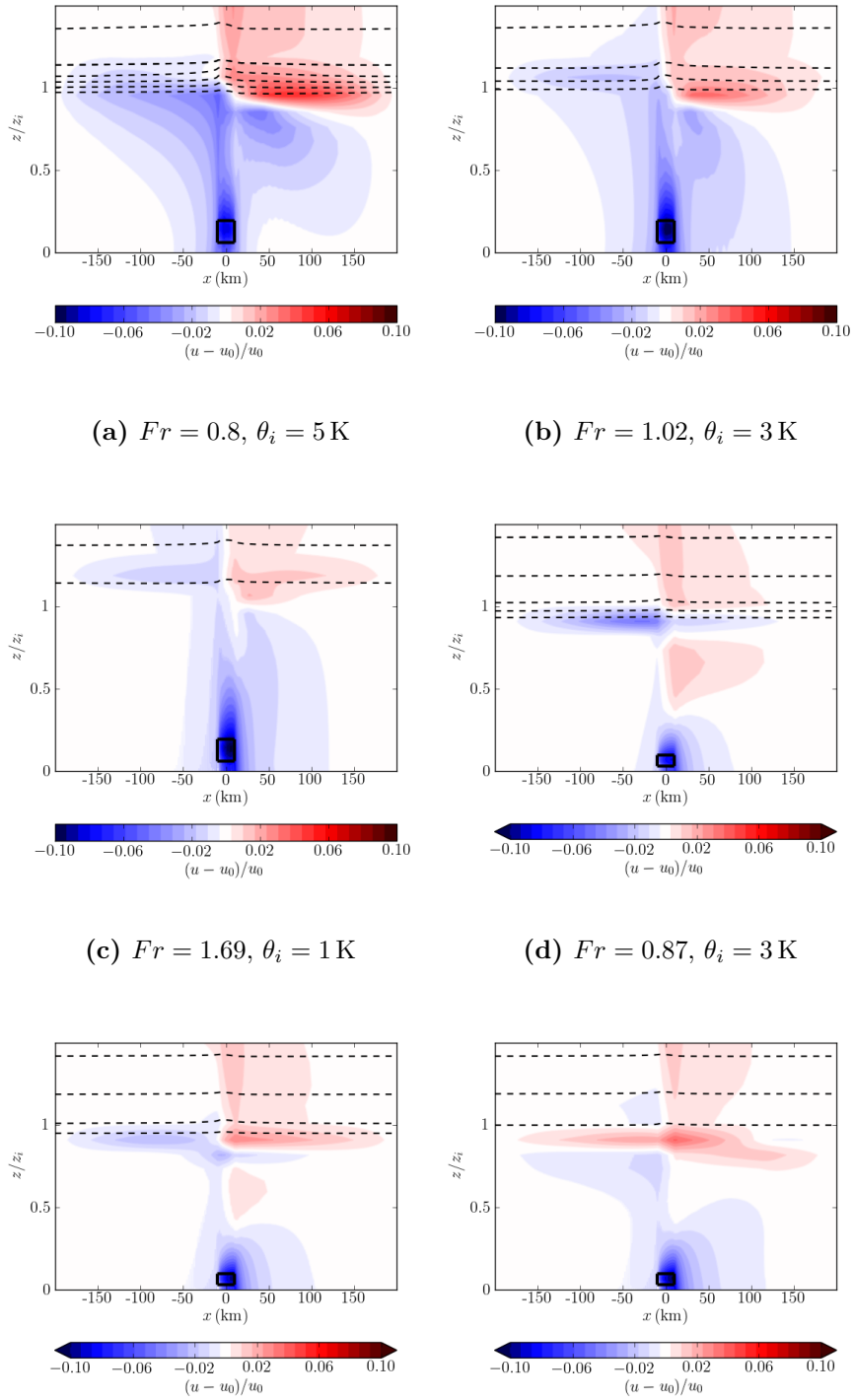

(a) $Fr = 0.8$, $\theta_i = 5\,\mathrm{K}$ **(b)** $Fr = 1.02$, $\theta_i = 3\,\mathrm{K}$

(c) $Fr = 1.69$, $\theta_i = 1\,\mathrm{K}$ **(d)** $Fr = 0.87$, $\theta_i = 3\,\mathrm{K}$

(e) $Fr = 1.06$, $\theta_i = 2\,\mathrm{K}$ **(f)** $Fr = 1.49$, $\theta_i = 1\,\mathrm{K}$

Figure 4.16: *Similar to figure 4.9 for simulations which have a change in inversion strength θ_i. Plots (a), (b), and (c) are for a case with initialised boundary layer depth $z_i = 715\,\mathrm{m}$ and (d), (e) and (f) have an initialised height of $z_i = 1364\,\mathrm{m}$. Increasing θ_i decreases the value of Fr.*

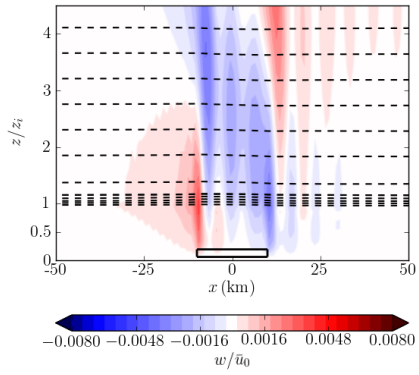

(a) $Fr = 0.8$, $\theta_i = 5\,\mathrm{K}$

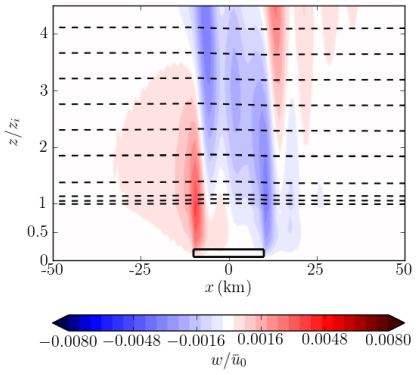

(b) $Fr = 1.02$, $\theta_i = 3\,\mathrm{K}$

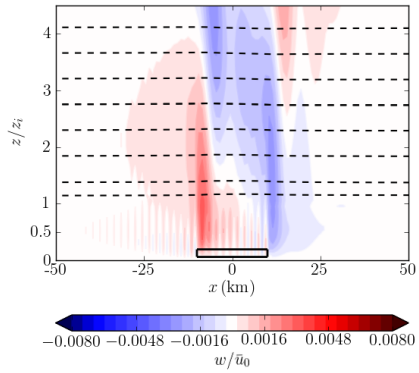

(c) $Fr = 1.69$, $\theta_i = 1\,\mathrm{K}$

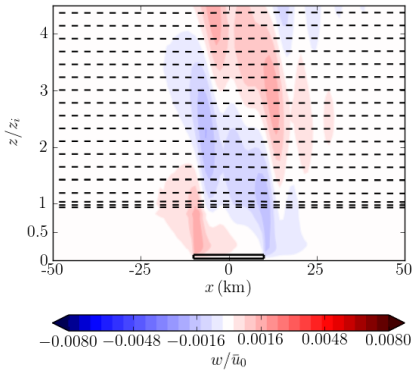

(d) $Fr = 0.87$, $\theta_i = 3\,\mathrm{K}$

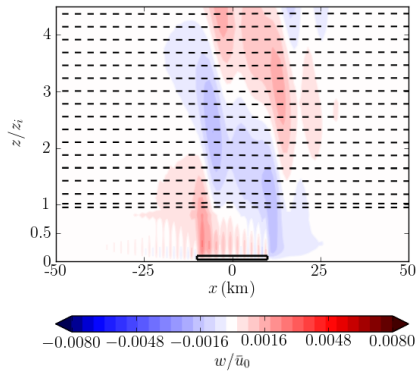

(e) $Fr = 1.06$, $\theta_i = 2\,\mathrm{K}$

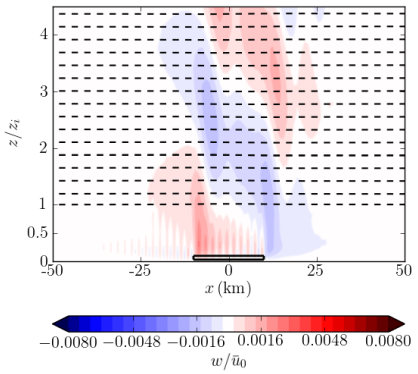

(f) $Fr = 1.49$, $\theta_i = 1\,\mathrm{K}$

Figure 4.17: *As was the case for figure 4.16 with the vertical velocity w.*

For $z_i = 1364\,\mathrm{m}$ there is little change in η between simulations. This difference to the $z_i = 715\,\mathrm{m}$ simulations shows that z_i plays an important role in determining the impact of the wind farm on the boundary layer.

Figures 4.19(a,c,e) show that as θ_i decreases, there is an increase in vertical transport, as represented by the increasing $w\partial u/\partial z$. This is linked with the increased deceleration of momentum $u\partial u/\partial x$. The decrease of momentum in the horizontal direction leads to an increase of momentum in the vertical direction, which in turn increases the boundary layer height over the wind farm.

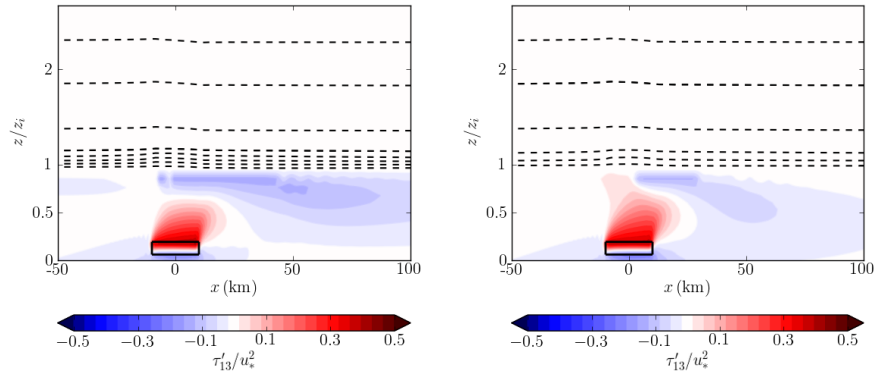

(a) $Fr = 0.8$, $\theta_i = 5\,\mathrm{K}$ **(b)** $Fr = 1.02$, $\theta_i = 3\,\mathrm{K}$

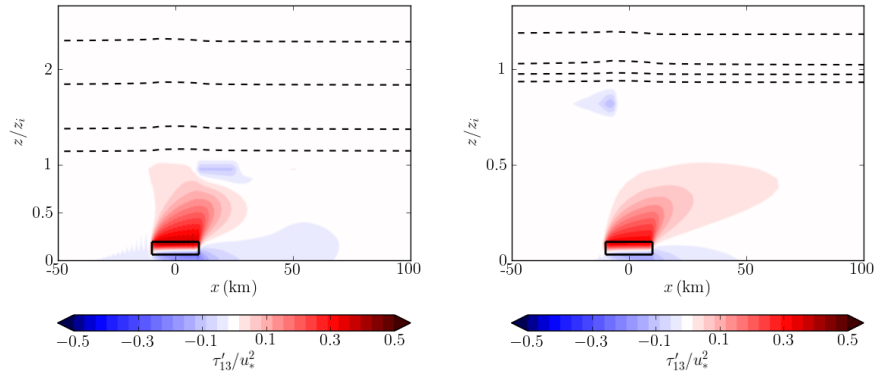

(c) $Fr = 1.69$, $\theta_i = 1\,\mathrm{K}$ **(d)** $Fr = 0.87$, $\theta_i = 3\,\mathrm{K}$

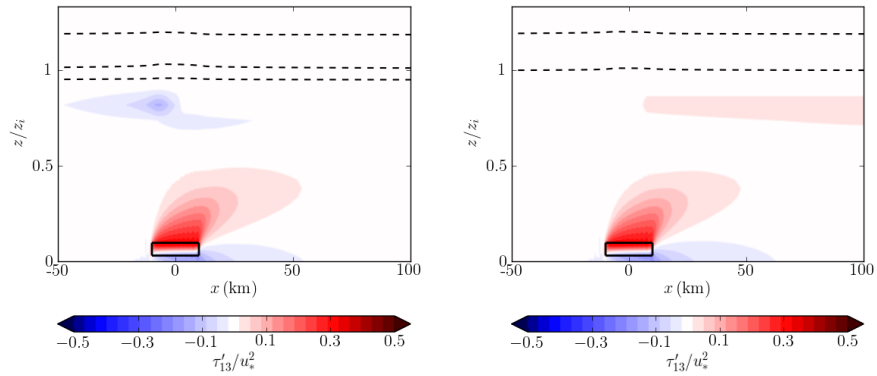

(e) $Fr = 1.06$, $\theta_i = 2\,\mathrm{K}$ **(f)** $Fr = 1.49$, $\theta_i = 1\,\mathrm{K}$

Figure 4.18: *As with figure 4.16 for the* τ_{13} *field.*

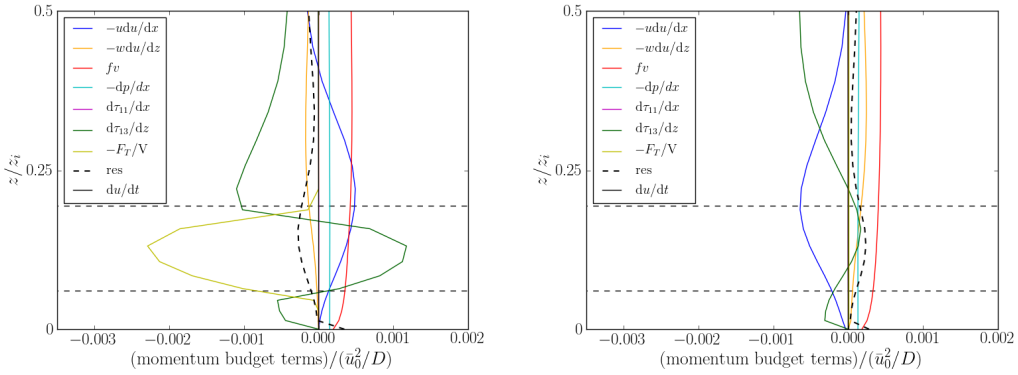

(a) $Fr = 0.8$, $\theta_i = 5\,\mathrm{K}$ **(b)** $Fr = 0.8$, $\theta_i = 5\,\mathrm{K}$

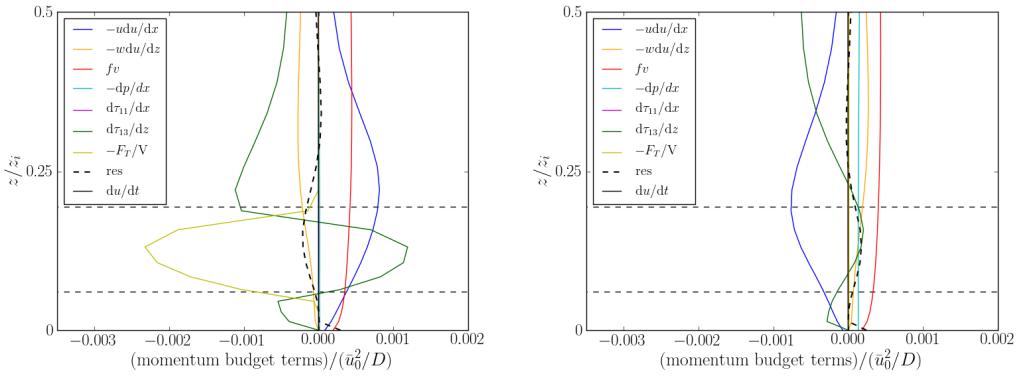

(c) $Fr = 1.02$, $\theta_i = 3\,\mathrm{K}$ **(d)** $Fr = 1.02$, $\theta_i = 3\,\mathrm{K}$

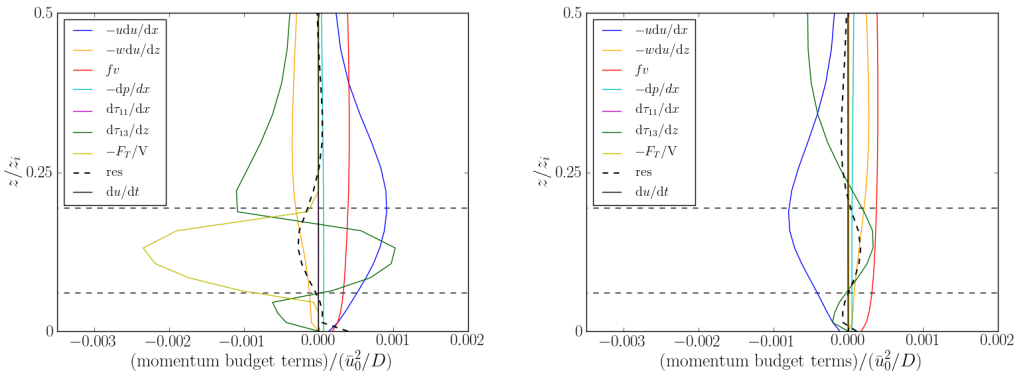

(e) $Fr = 1.69$, $\theta_i = 1\,\mathrm{K}$ **(f)** $Fr = 1.69$, $\theta_i = 1\,\mathrm{K}$

Figure 4.19: *Momentum budget terms for simulations with different θ_i, both on the upstream wind farm edge (left) and downstream wind farm edge (right). These are shown for simulations with an initialised boundary layer of $z_i = 715\,\mathrm{m}$.*

4.3.6 Boundary layer depth impacts

Simulations $Fr = 0.87, 0.92, 1.02$ and 1.071 are initialised with $U = 12\,\mathrm{m\,s^{-1}}$ and have $\theta_i = 3.1\,\mathrm{K}$. The boundary layer depths are initialised at $z_i = 1364\,\mathrm{m}$, $z_i = 725\,\mathrm{m}$, $z_i = 992\,\mathrm{m}$ and $z_i = 452\,\mathrm{m}$. Due to the changes in z_i, the boundary layer velocities are calculated to be $\bar{u}_0 = 10.4$, 9.7, 8.9 and $7.3\,\mathrm{m\,s^{-1}}$. Before any analysis of the effect of changing z_i in these simulations it is worth noting that any observed changes from the wind farm wake may not be entirely forced by z_i changes. This is due to the increase in $\bar{u}_0$ when z_i decreases for a given initialised U. For this reason the simulations cross over with those used in section 4.3.4 where $\bar{u}_0$ was varied. The changes observed in section 4.3.4 will be used to isolate the impact from z_i changes.

Figure 4.20(a) is the same as figure 4.9(c) which was discussed in section 4.3.4. This simulation has an initialised boundary layer depth of $z_i = 1364\,\mathrm{m}$. Decreasing z_i, and thus increasing Fr, there are multiple changes to the velocity perturbation caused by the wind farm. Figures 4.20(b and c) show an increase in the horizontal extent of the wake, with $Fr = 1.02$ showing a small perturbation at 150 km downstream. There are also changes to the upstream velocity perturbation, although there is not a consistent increase or decrease between the simulations. The final simulation, $Fr = 1.071$, displays a small wind farm wake. This could be attributed to the increase in Froude number, however due to the small increases in Fr in these simulations, the change in wind farm wake size is due to the decrease in boundary layer height. With a high boundary layer $z_i \geq 992\,\mathrm{m}$, the wind farm wake remains relatively undisturbed by the capping inversion, figure 4.20(a and b). These plots show a downstream wake that is fully developed, with the upstream velocity perturbation extending the full boundary layer height in $Fr = 0.92$. This is consistent with section 4.3.4 for decreases in $\bar{u}_0$. Decreasing z_i further to 715 m, figure 4.20(c), the downstream wind farm wake extends to the boundary layer top, at which point there is an increase in velocity caused by a decrease in the boundary layer downstream. Upstream the velocity perturbation once again spans the full boundary layer height, with the signal being observed in the air aloft. A further decrease to $z_i = 452\,\mathrm{m}$ shows greater interaction between the wind farm wake and the boundary layer. Figure 4.20(d) shows a large deflection in the isentropes over the wind farm. From table 4.2 we see that $Fr = 1.071$ has an inversion increase of $\eta/\eta_0 = 0.12$ compared to

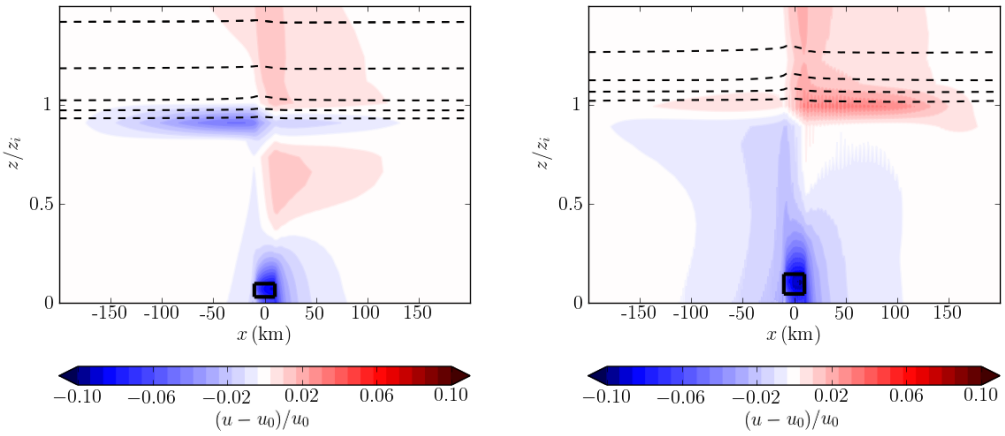

(a) $Fr = 0.87$, $z_i = 1364\,\mathrm{m}$ **(b)** $Fr = 0.92$, $z_i = 992\,\mathrm{m}$

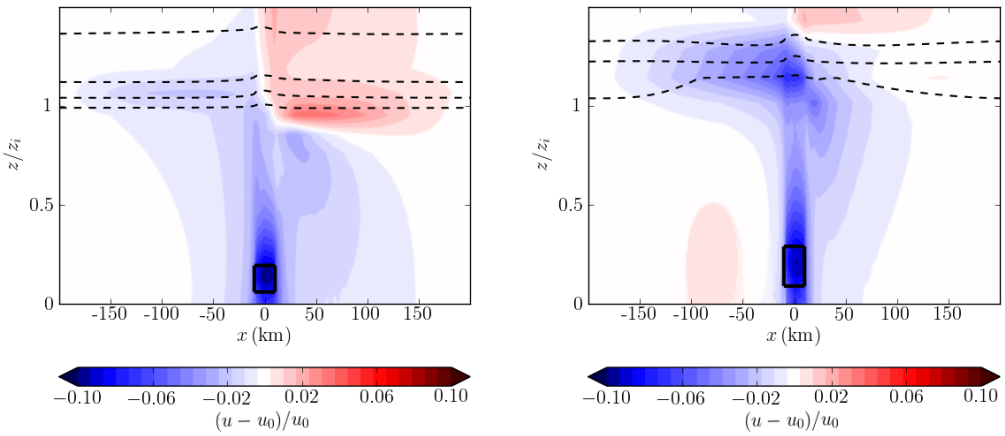

(c) $Fr = 1.02$, $z_i = 715\,\mathrm{m}$ **(d)** $Fr = 1.071$, $z_i = 452\,\mathrm{m}$

Figure 4.20: *Normalised velocity perturbations are plotted for the simulation of different values of z_i. The vertical axis is normalised with the initialised z_i for the respective simulations. The dashed contours represent θ with $1\,\mathrm{K}$ intervals and show the top of the boundary layer. The wind farm rotor areas are given by the black box.*

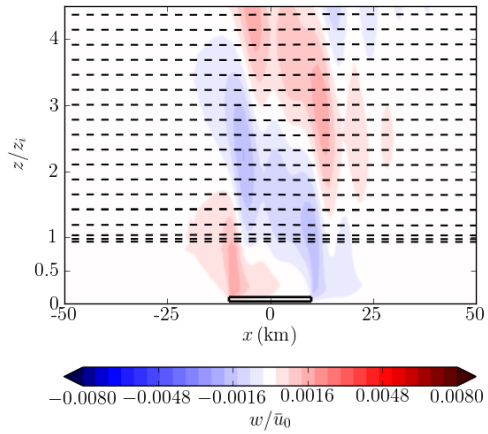

(a) $Fr = 0.87$, $z_i = 1364\,\mathrm{m}$

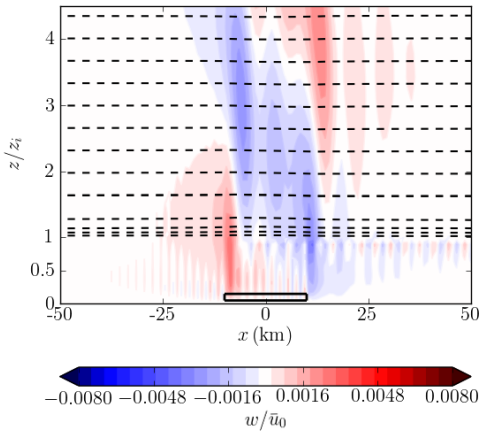

(b) $Fr = 0.92$, $z_i = 992\,\mathrm{m}$

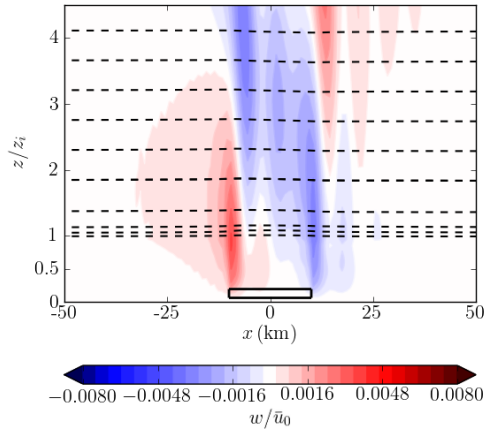

(c) $Fr = 1.02$, $z_i = 715\,\mathrm{m}$

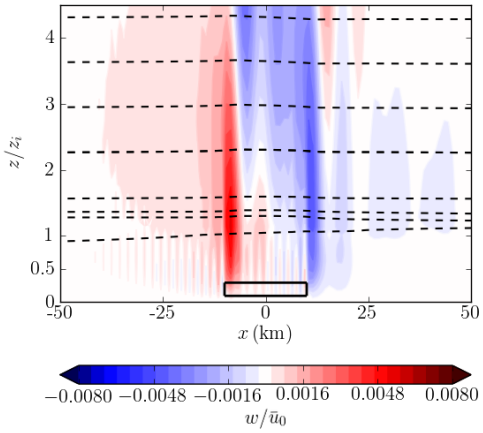

(d) $Fr = 1.071$, $z_i = 452\,\mathrm{m}$

Figure 4.21: *As for figure 4.20, however showing w.*

$Fr = 0.87$ increasing by $\eta/\eta_0 = 0.0062$. This is due to the interaction with the wind farm wake.

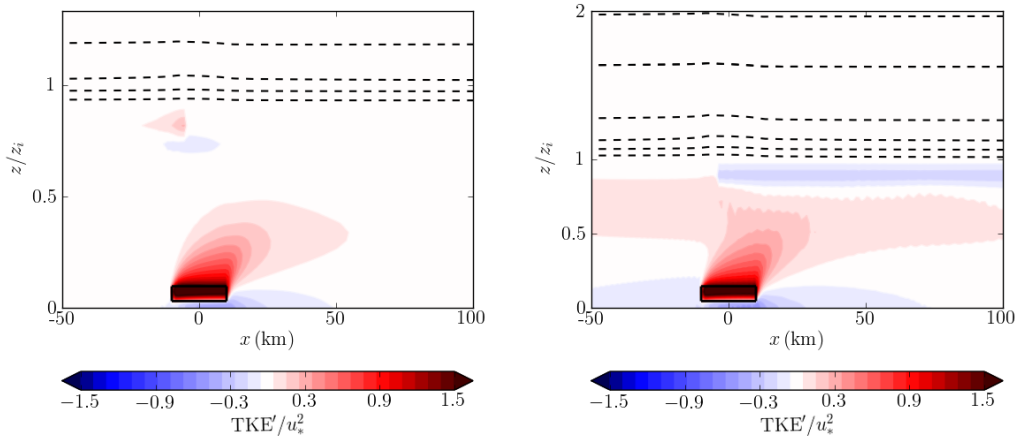

(a) $Fr = 0.87$, $z_i = 1354\,\mathrm{m}$ **(b)** $Fr = 0.92$, $z_i = 992\,\mathrm{m}$

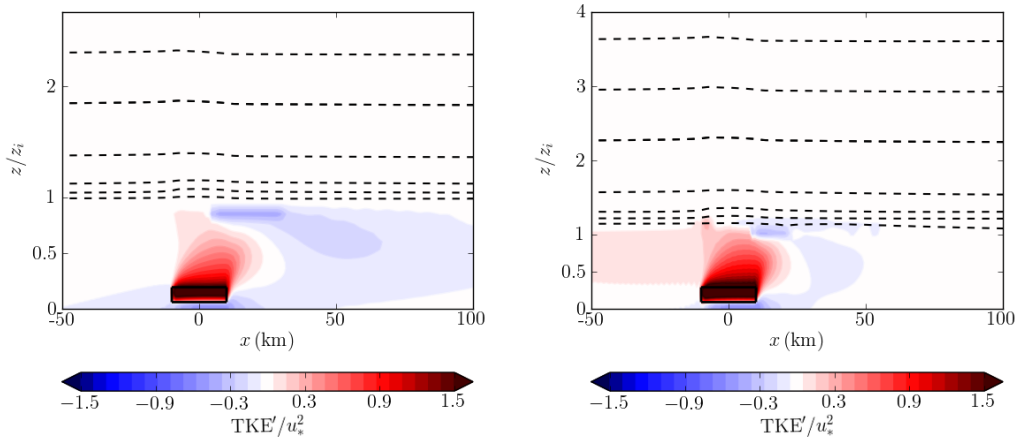

(c) $Fr = 1.02$, $z_i = 715\,\mathrm{m}$ **(d)** $Fr = 1.071$, $z_i = 452\,\mathrm{m}$

Figure 4.22: *The TKE field for simulations with different z_i. Other features are the same as figure 4.20.*

The TKE perturbations in figure 4.22 also show that as z_i decreases, there is greater interaction with the boundary layer inversion. In section 2.5.3 the idea of an asymptotic boundary height was introduced, where boundary layer increases above h_c show no further mixing into the wind farm wake from the air above the

wind farm, based on Csanady (1974). The height h_c is defined as

$$h_c = A\frac{\theta_0}{g\theta_i}u_*^2 \tag{4.5}$$

where $A = 500$ is an empirical constant. For these simulations $u_* \approx 0.5\,\mathrm{m\,s^{-1}}$ and hence the asymptotic height is $h_c \approx 1225\,\mathrm{m}$. These simulations suggest that the boundary layer height at which there is no mixing with the wind farm wake is lower (between 715 m and 992 m), but there are insufficient simulations to definitively show the critical value of z_i.

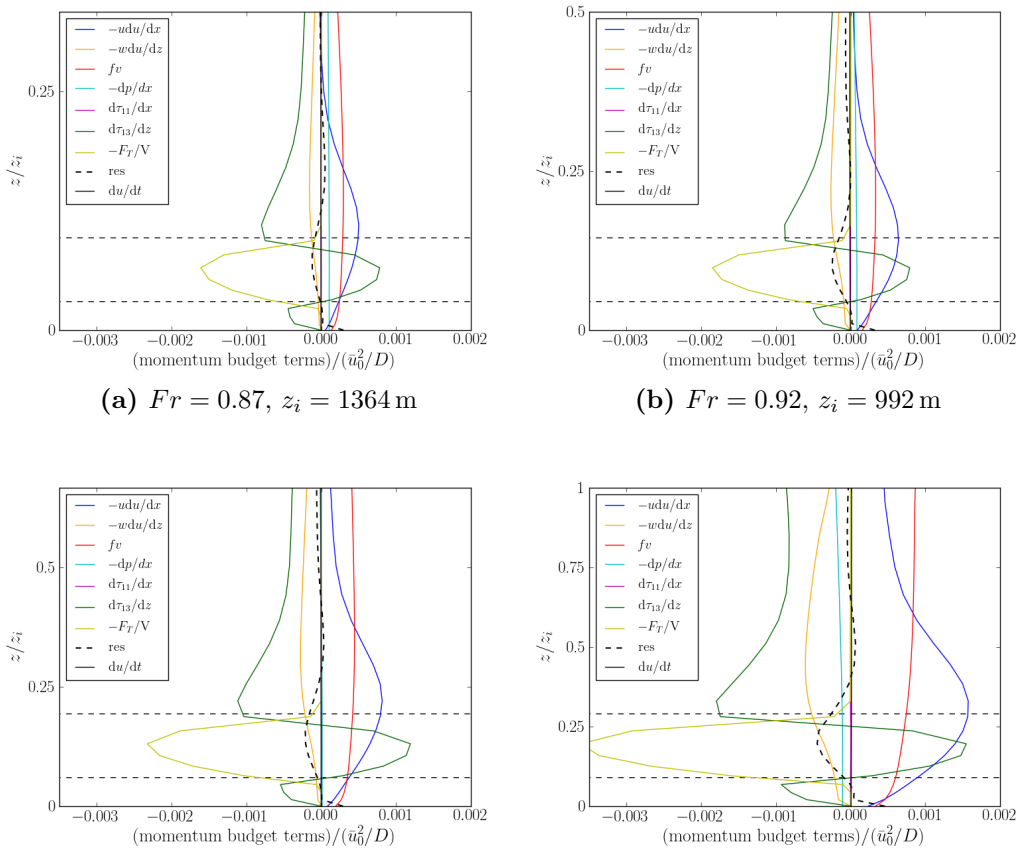

(a) $Fr = 0.87$, $z_i = 1364\,\mathrm{m}$ **(b)** $Fr = 0.92$, $z_i = 992\,\mathrm{m}$

(c) $Fr = 1.02$, $z_i = 715\,\mathrm{m}$ **(d)** $Fr = 1.071$, $z_i = 452\,\mathrm{m}$

Figure 4.23: *Momentum budget terms for change in θ_i simulations on the upstream wind farm edge.*

The momentum budget in figure 4.23 shows that on the upstream edge of the wind farm, although F_T remains equal between simulations and hence $\partial\tau_{13}/\partial z$ is equal within the wind farm rotor area, above the wind farm the lower z_i simulations show a decrease in $\partial\tau_{13}/\partial z$. This, alongside the vertical velocity fields in figure

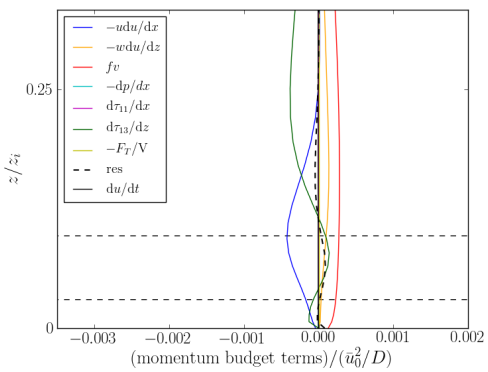

(e) $Fr = 0.87$, $z_i = 1364\,\mathrm{m}$

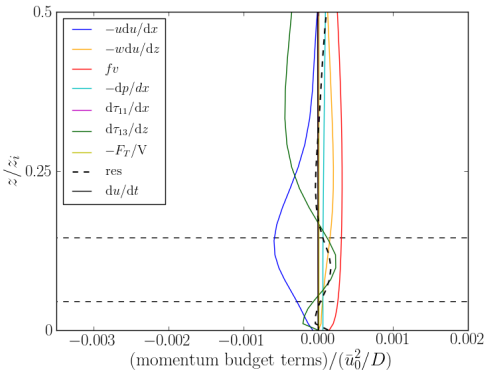

(f) $Fr = 0.92$, $z_i = 992\,\mathrm{m}$

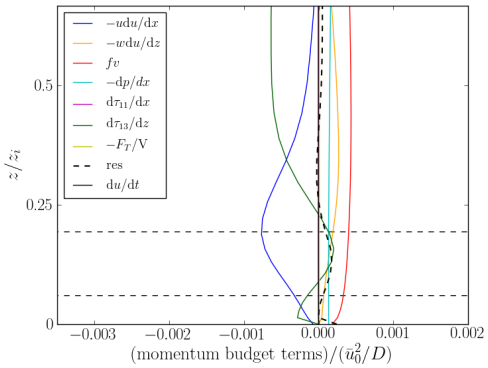

(g) $Fr = 1.02$, $z_i = 715\,\mathrm{m}$

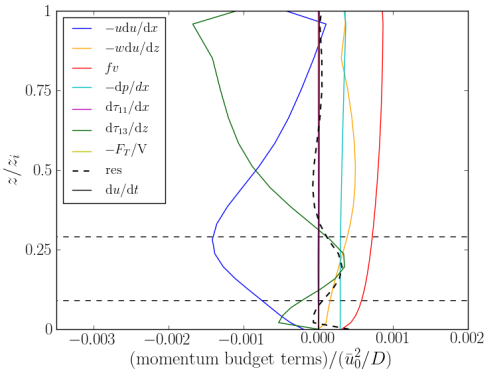

(h) $Fr = 1.071$, $z_i = 452\,\mathrm{m}$

Figure 4.22: *As described in 4.23 however for the downstream wind farm edge.*

4.21, show that there is an increase in the vertical momentum in front of the wind farm for lower z_i. This is caused by the increase in deceleration $u\partial u/\partial x$ for low z_i inducing greater vertical acceleration $w\partial u/\partial z$. The vertical acceleration spans the full boundary layer depth in $Fr = 1.071$ and $Fr = 1.02$. Downstream of the wind farm there is an increase in the mean vertical transport down into the wind farm rotor area from the air above, shown in figure 4.22 by the increase in $w\partial u/\partial z$ for decreasing z_i. Of further interest is that the maximum value of $w\partial u/\partial z$ occurs at the same height within the boundary layer, showing that the wake height is determined by the wind farm and not by the boundary layer dynamics.

The wind farm induced deceleration, figure (4.24), spans up to $0.5z_i$ in $Fr = 0.87$, which is taken to be the undisturbed wake case. The reduction to $z_i = 992\,\mathrm{m}$ increases the deceleration to the top of the boundary layer, although showing little boundary layer disturbance. The same occurs in the $Fr = 1.02$ case where the height of deceleration is therefore matching $Fr = 0.87$. Above the boundary layer there is little deceleration of the flow in these three cases. This suggests that the height at which the wind farm wake interacts with the boundary layer is $715 - 992\,\mathrm{m}$ in these cases. Using this assumption, in $Fr = 0.92$ the residual layer between the wind farm wake and the capping inversion would be of a smaller magnitude than the wind farm wake, with the residual layer reduced as the wake develops.

This simulation case has shown that increasing Fr by decreasing z_i produces differences in the interaction between the wind farm wake and the boundary layer. These simulations model wind turbines with a hub height of 95 m. When the initialised boundary layer height is set at and below $z_i = 715\,\mathrm{m}$, there is the greater impact on the boundary layer height from the wind farm. The undisturbed wind farm wake in figure 4.22(a) shows that for this turbine hub height, the wind farm wake is $0.5z/z_i$, which is approximately 650 m. It is understandable that when the wind farm wake and boundary layer top converge there will be the greater observable change.

Above the height of 715 m, the wind farm can either be fully developed with a residual layer above, $Fr = 0.87$, or fully developed spanning the full boundary layer depth. It is argued that the critical height at which this transition occurs is lower than the asymptotic height h_c proposed by Csanady (1974). The simulation $Fr = 1.071$ shows large changes in the velocity and inversion displacement in this analysis. The analysis here is time averaged, but the time dependent flow shows

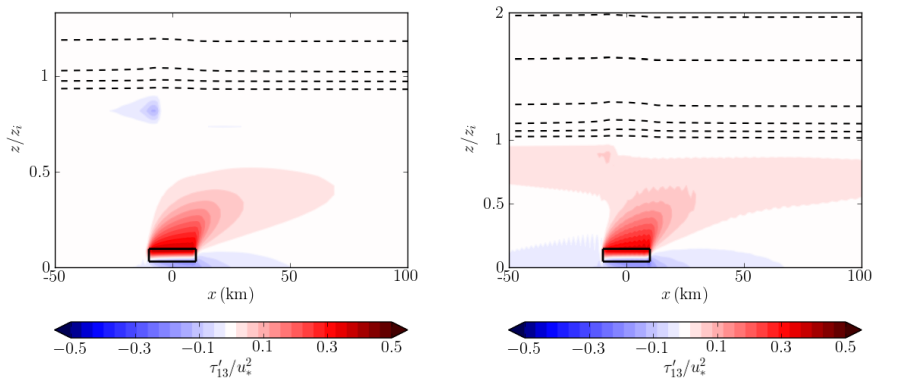

(a) $Fr = 0.87$, $z_i = 1364\,\mathrm{m}$ **(b)** $Fr = 0.92$, $z_i = 992\,\mathrm{m}$

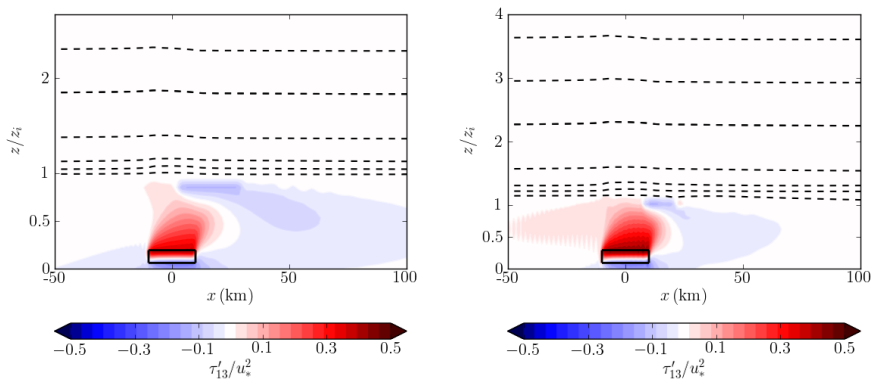

(c) $Fr = 1.02$, $z_i = 715\,\mathrm{m}$ **(d)** $Fr = 1.071$, $z_i = 451\,\mathrm{m}$

Figure 4.23: *Similar to figure 4.9 but showing* τ_{13} *in each simulation.*

large variability over the time in question for $Fr = 1.071$ (figure 4.2(i)). Although this provides challenges in quantifying the effects, it shows that the decrease in z_i to the point where the wake is constrained has large impacts on the flow, much more than other simulations with increased z_i.

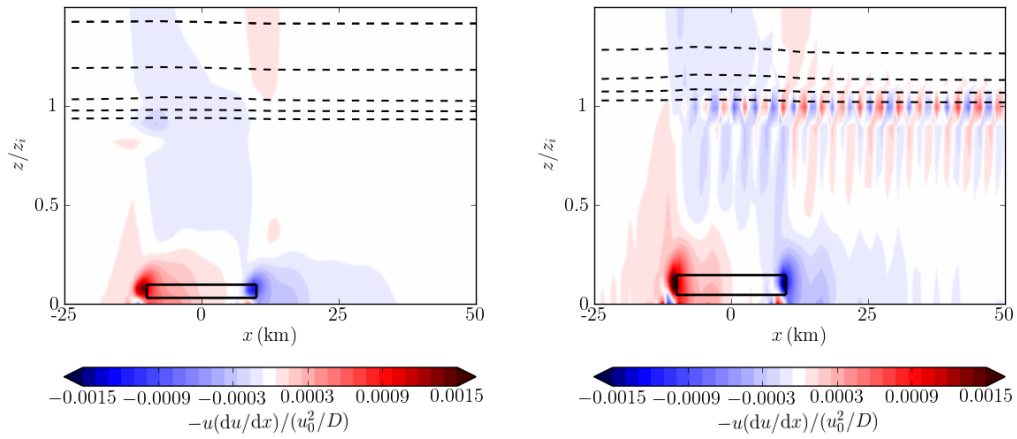

(a) $Fr = 0.87$, $z_i = 1364\,\mathrm{m}$ **(b)** $Fr = 0.92$, $z_i = 992\,\mathrm{m}$

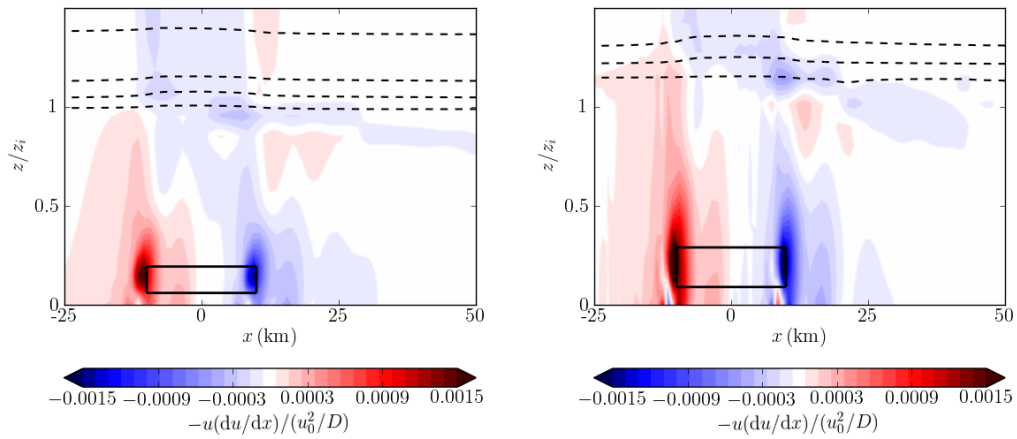

(c) $Fr = 1.02$, $z_i = 715\,\mathrm{m}$ **(d)** $Fr = 1.071$, $z_i = 452\,\mathrm{m}$

Figure 4.24: *The normalised* $u\mathrm{d}u/\mathrm{d}x$ *field for each simulation with different* z_i.

4.4 Modifying the length of the wind farm

The simulations so far have been concerned with a fixed wind farm size, with $W_x = 20$ turbines. This sections looks at the effect of changing the length of the wind farm. Simulations were carried out as described in section 4.2, where the initialised boundary layer has $Fr = 1.02$ (table 4.1). Multiple wind farms were modelled, ranging from $W_x = 2$ to $W_x = 32$ turbines; only 2-d simulations were carried out hence infinitely wide wind farms are modelled.

Increasing the length of the wind farm increases the length of the wind farm wake both upstream and downstream of the wind farm, shown in figure 4.25. The magnitude of the velocity perturbations within the wind farm increase as W_x increases. This is attributed to the total increase in drag from the wind farm. Velocity decreases throughout the boundary layer are observed in all simulations. It was shown in section 4.3.6 that boundary layers with $z_i = 715\,\mathrm{m}$ interact directly with the wind farm wake, and this feature is true for small wind farms with $W_x = 2$ turbines (figure 4.25a). Decreasing the wind farm size does not noticeably change the height of the wind farm wake. The magnitude of any perturbations within the wake, howver, is reduced from modelling a smaller wind farm. The velocity decrease along the inversion upstream of the wind farm is visible for $W_x = 4$ (not shown) and increases with W_x. Along the inversion, the velocity increases represent decreases in the boundary layer height. The boundary layer displacement, η, increases as W_x increases, a sign that the total wind farm drag influences the boundary layer displacement (figure 4.26).

The magnitude of TKE perturbations do not significantly change between simulations. This is true for the decrease in TKE below the rotor area and downstream along the inversion layer. At $W_x = 16$, these two sections converge, see figure 4.27(b). The TKE perturbations extend to the top of the boundary layer for $W_x = 6$, at which point the TKE growth is inhibited by the TKE decrease along the inversion. This decrease in TKE represents a decrease in the boundary layer height (also shown by the increase in velocity perturbations in figure 4.25). At $W_x = 16$, the boundary layer decrease propagates further downstream. This allows the additional TKE from the wind farms to increase in height as there is no longer a blocking from the inversion. As W_x increases there is an elongation of TKE decrease along the inversion (figure 4.27c).

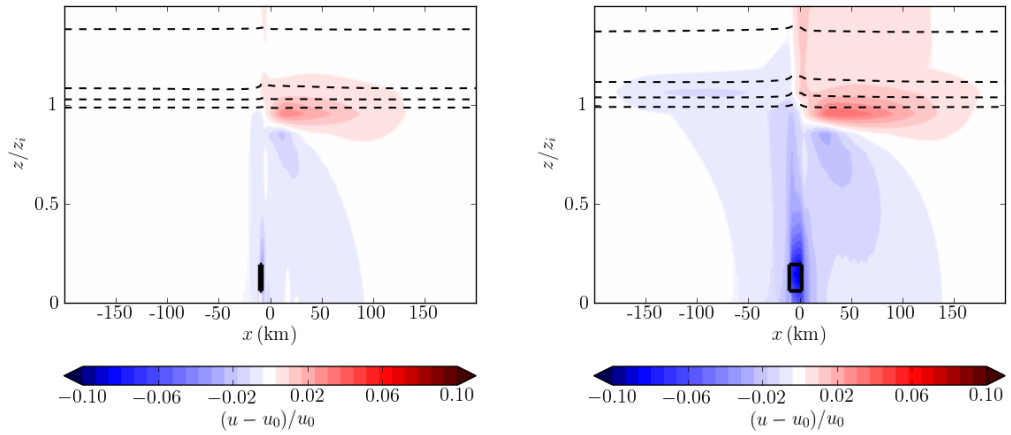

(a) $W_x = 2$ **(b)** $W_x = 12$

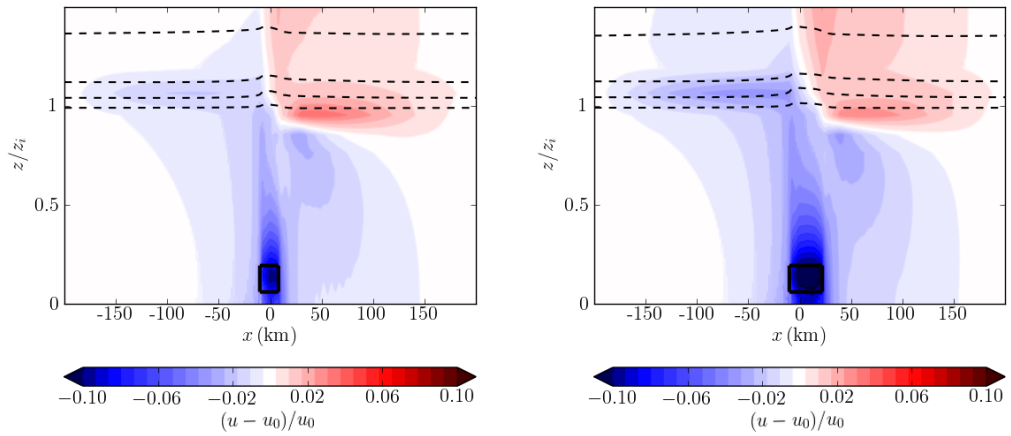

(c) $W_x = 18$ **(d)** $W_x = 32$

Figure 4.25: *Normalised horizontal velocity contours for the* $Fr = 1.02$ *simulation with various wind farm lengths* W_x*. Shown here are a selection of the simulations,* $W_x = 2$*,*$W_x = 12$*,* $W_x = 18$ *and* $W_x = 32$*. In each plot the black box defines the wind farm area.*

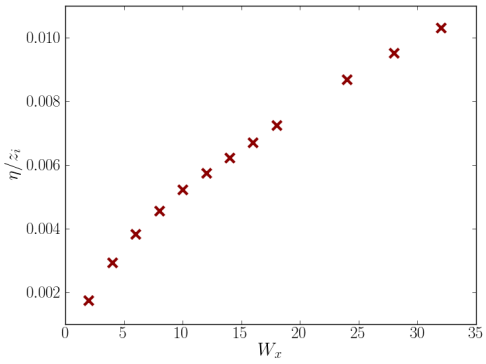

Figure 4.26: *Changes in inversion displacement η for varying wind farm length W_x.*

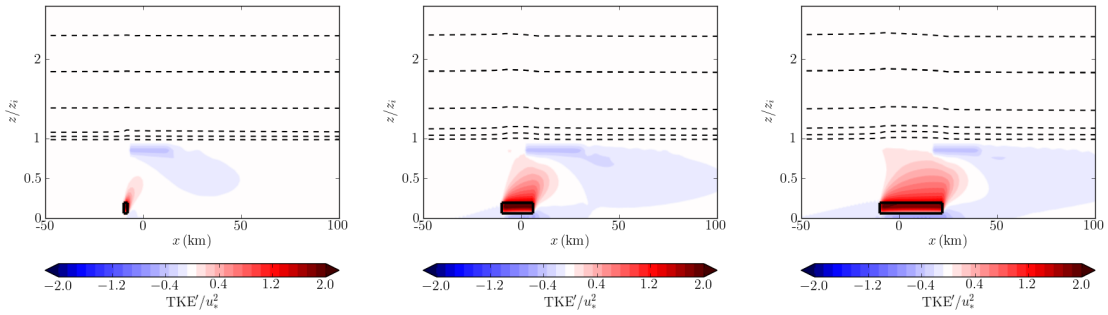

(a) $W_x = 2$ **(b)** $W_x = 16$ **(c)** $W_x = 32$

Figure 4.27: *TKE contour plots for $W_x = 2$,$W_x = 16$ and $W_x = 32$, normalised with u_*^2. In each plot the black box defines the wind farm area.*

Decreases in velocity from the presence of a wind farm begin upstream and continue through the wind farm. Near the end of the wind farm this switches to velocity increases as surrounding air is mixed into the wake. Deceleration of the horizontal momentum, $u\partial u/\partial x$, is shown in figure 4.28 (shown by positive values as $-u\partial u/\partial x$ is plotted). Through the wind farm the momentum deceleration continues, however between $W_x = 18$ and $W_x = 24$ there is no further deceleration of momentum past 0 km. For $W_x \geq 24$, $u\partial u/\partial x = 0$ for some part of the wind farm, meaning no further velocity changes. The flow is then able to stabilise and the boundary layer height can adjust to the velocity deficit caused by the wind farm. The change in boundary layer heights over the extent of the wind farms are shown in table 4.3. The negative values for $W_x \geq 24$ indicate a decrease in boundary layer height, similar to a hydraulic jump as observed in orographic flows

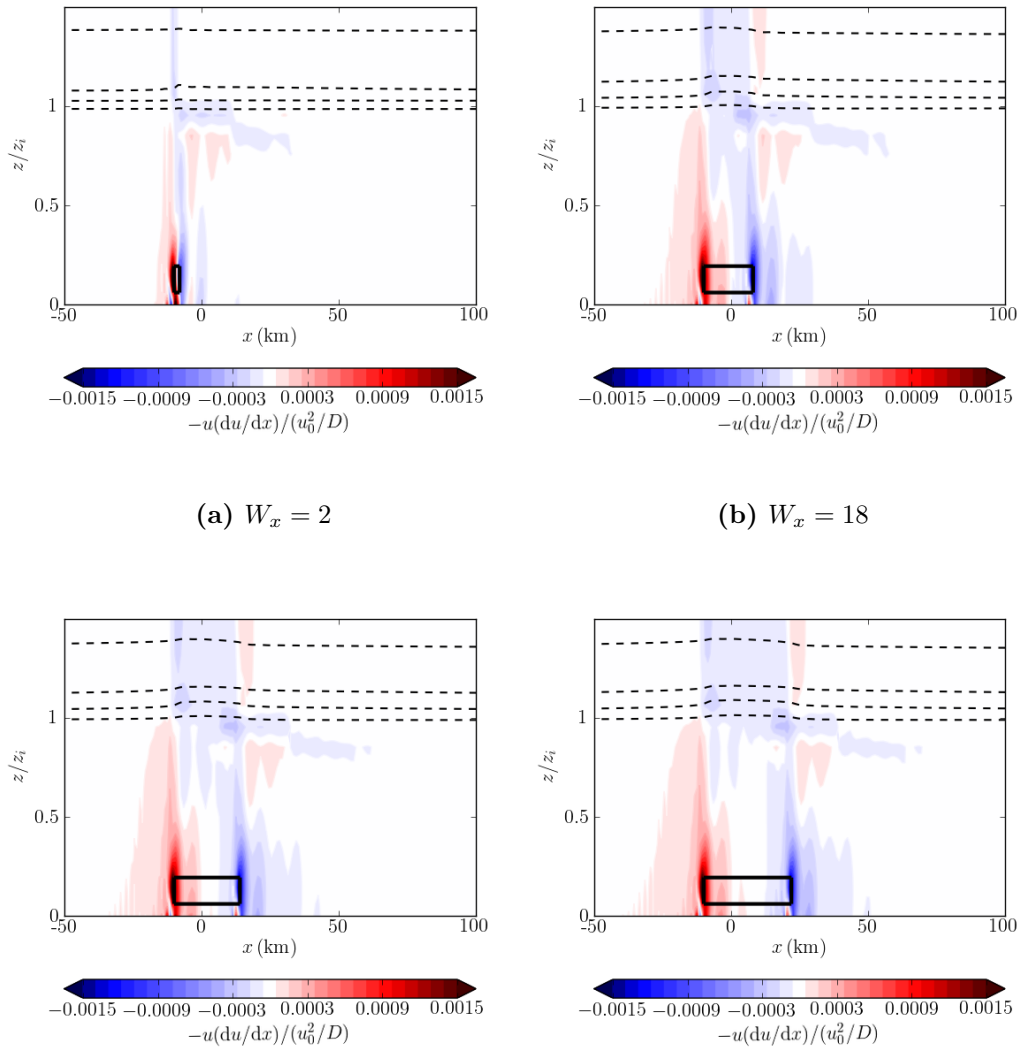

(a) $W_x = 2$ **(b)** $W_x = 18$

(c) $W_x = 24$ **(d)** $W_x = 32$

Figure 4.28: *Contour plots of $-u\partial u/\partial x$ normalised with u_0^2/D. Plots are shown for the simulations with $W_x = 2$,$W_x = 18$,$W_x = 24$ and $W_x = 32$.*

however on a smaller scale. These would occur for $Fr \approx 1$ in a neutral boundary layer capped by an inversion (Stull, 1988, p. 607). These inversion height changes are not a hydraulic jump, however these simulations hint as to why they are not observed. For the smaller wind farms, $W_x < 24$, the flow is either in a state of increasing or decreasing momentum. The sudden change between these two states means that the flow cannot adjust to the wind farm drag. When $W_X \geq 24$ there is a period of adjustment and this translates into a decrease in $z_i^u - z_i^d$ (more negative). If hydraulic jumps are to be generated by a wind farm, then W_x would need to be sufficiently large enough to allow the faster flowing air above the wind farm to form the equivalent of a downslope wind on the downstream edge. The permeable nature of the wind farm may be an additional reason for the lack of hydraulic jumps.

W_x	2	4	6	8	10	12
$\frac{z_i^u - z_i^d}{z_i}$	0.0040	0.0062	0.0071	0.0080	0.0086	0.0081
W_x	14	16	18	24	28	32
$\frac{z_i^u - z_i^d}{z_i}$	0.0076	0.0078	0.0063	−0.0015	−0.0030	−0.0039

Table 4.3: *Changes in inversion height over the length of the wind farm, $z_i^u - z_i^d$ for different wind farm length.*

4.5 Summary

This chapter has looked at the impact of different boundary layer structures on the formation of the wind farm wake. Three parameters were used to control the boundary layer: $\bar{u}_0$, θ_i and z_i. The smallest observed impact was from changes to θ_i. It was shown that a decrease in the capping inversion strength increased the displacement of the boundary layer. To show this, two sets of simulations were used, with different initialised boundary layer depths. It was observed that the impacts on the wind farm wake velocity perturbations were largely due to the boundary layer depth.

To analyse the effect of different boundary layer heights, four simulations with varying depth were used, each with equal capping inversion and geostrophic wind. The simulations with lower z_i showed an increase in interaction between the

inversion and the wind farm wake. This interaction became prominent at $z_i = 715\,\text{m}$, intensifying as z_i decreased further. This shows that the height of the wind farm wake is not dependent on the boundary layer depths, provided the wake is smaller than z_i.

The final set of simulations varying $\bar{u}_0$ showed that an increase in velocity changed the structure of the wake. This case had $z_i = 1364\,\text{m}$ and thus was able to fully develop without direct interaction with the capping inversion. When $\bar{u}_0$ increased, the wake decreased both upstream and downstream of the wind farm. This is caused by an increase in vertical transport which increased the height of the wake and boundary layer depth.

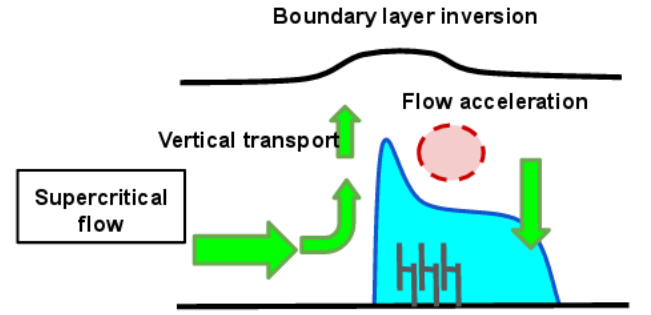

(a)

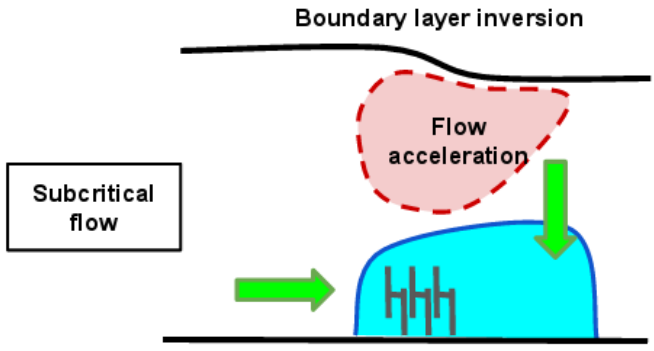

(b)

Figure 4.29: *Overview of how boundary layers with different Froude numbers affect the wind farm effects on the boundary layer.*

To identify the key dynamics which affect the impact of wind farms on the boundary layer, the non-dimensional parameters Fr and Z have been used. Figure 4.29(a) shows a summary of the effects of changing the boundary layer Froude number. When the boundary layer is a supercritical flow, there are increases in

vertical velocity at the front of the wind farm, increasing the height of the wind farm wake at the front edge of the wind farm. This in turn leads to a greater boundary layer displacement, η, above the wind farm. Above the wind farm, there is a small area where the boundary layer is in a state of acceleration. The boundary between this area and the wind farm wake leads to an increase in TKE. When the boundary layer is subcritical, there are differences in the behaviour of the wind farm, summarised in figure 4.29(b). Wind farms in subcritical flow have longer wind farm wakes, but shallower that supercritical flows; the vertical transport at the front of the wind farm is significantly smaller than supercritical flows. There is a larger area where the boundary layer is accelerating above the wind farm. This area extends to the boundary layer inversion top. The boundary layer decreases in height over the wind farm, resulting in an increased velocity along the boundary layer top downstream of the wind farm.

Waves aloft play an important role in the wind farm impacts. Decreases in Z imply that waves aloft have a greater impact on the flow, with increases in the upstream pressure perturbation increasing with decreasing Z. For low Z, the strength of the capping inversion becomes an important feature compared to high Z flows, whereby impacts from the wind farm are inhibited for increasing θ_i.

Increasing the size of wind farms does not significantly alter the interaction with the boundary layer. There is an increase in the velocity deficit from large wind farms due to the increase total drag. Larger wind farms create a greater inversion displacement with the greatest increase rate occurring for small wind farms. This is because the initial impact from the wind farm on the boundary layer does not significantly change as the wind farm size increases. The simulations of varying wind farm size have $z_i = 715\,\mathrm{m}$, and it is known that the wind farm interactions with the boundary layer are greater at this height.

With the exception of low boundary layer simulations, the wind farm's wake behaves in a similar manner, with only subtle changes to the wake length upstream and downstream. Any changes to the velocity that are observed at distances greater than 20 km are less than 1% of the upstream velocity. This implies that any impacts from the velocity reduction that may occur from wind farms will only be on the local meteorology.

The largest change in the wake was from the changes to z_i. A lowering of the boundary layer height towards the top of the wind farm wake increases the changes observed along the boundary layer. When the wind farm wake is allowed to freely develop, without interacting with the boundary layer, changes in the boundary layer are more linked to the flow Froude number. When the boundary layer height decreases towards the wind farm wake height, larger impacts can be noticed. When the distance between the top of the boundary layer and the wind farm wake decreases, an elongation of the wind farm wake occurs. This mean the wind farm wake reaches the top of the boundary layer, higher than the equivalent undisturbed wind farm wake height. A direct interaction between the wind farm wake and boundary layer top creates the greatest changes, with larger decreases in boundary height downstream of the wind farm compared to upstream. All of the simulations in the chapter used wind turbines with the same hub height. Although different wind farm width were modelled, there were no clear differences to the height of the wind farm wake downstream. It is hypothesised that the turbine height and rotor diameter are the controlling features of wind turbine and subsequently wind farm wakes. This is the mechanism by which wind farms will have the greatest impact on the meteorology. Once again the impact from these idealised wind farm simulations is small, and it is unknown how these wakes will behave if additional mesoscale features are introduced.

Chapter 5

Comparing the Met Office BLASIUS model with a linear model

5.1 Introduction

The linear model described in Smith (2010) uses a simplistic parametrisation for the drag associated with a wind farm and indeed the boundary layer. In order to test the limitations of such a simplification, numerical simulations in the boundary layer model BLASIUS have been carried out. The option of using a linear model, and more importantly a model with a shorter running time, enables a full parameter space to be explored. This enables the full impact from wind farms to be explored. The linear model also suggests that stalling can occur in a wind farm, and it is of interest to test this in a more realistic boundary layer model.

In order to maximise computational efficiency, 2-dimensional BLASIUS simulations are carried out, with periodic boundary conditions in both horizontal directions. Although this may be physically unrealistic, the aim of this work is to compare the linear model and BLASIUS, both of which work in 2-d. Limiting the comparison to 2-d means that more simulations can be carried out enabling a more thorough comparison of the two models. This work will therefore neglect

3-d simulations. This means that the effect of flow around the wind farms and the way this is modelled in both the linear model and BLASIUS will not be analysed.

5.2 Numerical model set up

5.2.1 Linear Model

The work of Smith (2010) describes a linear model of boundary layer perturbations caused by a wind farm. The boundary layer is modelled as a well mixed layer, capped by a temperature inversion with a stable layer aloft. The boundary layer is mixed by surface friction, prescribed by the surface friction coefficient C_B. The boundary layer air flow is given by the single velocity term $\mathbf{U}_{BL}(x) = (U_{BL}, V_{BL})$. The boundary layer is set at height z_i, with a capping inversion of θ_i. Above the boundary layer, the flow has velocity $\mathbf{U}(x, z) = (U, V)$, with the exchange of momentum between the two flows given by the transfer coefficient C_T. The linear model uses the Boussinesq momentum equations

$$U_{BL} \cdot \nabla U_{BL} = -\nabla p - C_B U_{BL} + C_T(U - U_{BL}) + F_X \tag{5.1a}$$

$$U \cdot \nabla U = -\nabla p \tag{5.1b}$$

where 5.1a(a) describes the boundary layer flow and 5.1a(b) shows the momentum of the air aloft. The turbine drag is given by F_X. As is often done with boundary layer flows, the velocity is given as perturbations from a mean flow $U_{BL} = \bar{u}_0 + \zeta$. Similarly, the pressure is given by $p = p_0 + \gamma$. Fourier transforms are used to solve these differential equations. This means that the variables in equation 5.1a are represented as

$$\zeta(x) = \Re\left[\hat{\zeta}(k)e^{ikx}\right]. \tag{5.2}$$

Doing the same for other variables, the momentum perturbation equation in Fourier space is

$$\hat{\zeta} ik\bar{u}_0 = -ik\hat{\gamma} - C_B\hat{\zeta} - C_T\hat{\zeta} + \hat{F}_X. \tag{5.3}$$

In order for this equation to be valid, it is assumed that the turbine drag is distributed uniformly throughout the boundary layer height. Smith (2010) states that this limits the model to large wind farms where the vertical mixing is sufficient to homogeneously distribute the turbine drag. Part of the work in this chapter will test this assumption. The velocity decrease caused by the wind farm will induce a displacement to the boundary layer inversion η. By mass conservation this is given by

$$k\bar{u}_0\hat{\eta}_L = -z_i k\hat{\zeta}. \tag{5.4}$$

The inversion is displaced into a stable layer of air with buoyancy frequency $N^2 = (g/\theta)\mathrm{d}\theta/\mathrm{d}z$. There will therefore be propagating waves along the inversion and vertically through the stable layer. This will induce a pressure gradient

$$\hat{\gamma} = \Theta\hat{\eta}_L \quad \text{with} \quad \Theta = \frac{iN^2}{m} + g^{'} \tag{5.5}$$

where $m(k) = N/U$ is the vertical wavenumber. Solving equation (5.3) leads to the inversion displacement and velocity perturbations of

$$\hat{\eta}_L = \frac{iz_i k\hat{F}_X}{S_B k\bar{u}_0 - iz_i\Theta k^2} \tag{5.6}$$

$$\hat{\zeta} = \frac{ik\Theta\hat{\eta}_L + \hat{F}_X}{S_B} \tag{5.7}$$

where $S_B = i\bar{u}_0 + C_B + C_T$. As previously stated, the turbine drag is distributed through the boundary layer within the wind farm horizontal area. For a given wind farm, the turbine density per unit area is given by $n\,(m^{-2})$ and thus the wind farm drag force in the model is

$$F_X = -\frac{nF_T}{\rho z_i}. \tag{5.8}$$

Prior to running the linear model, the input velocities, boundary layer height and strength, along with the desired wind farm must be known. From these, the surface friction coefficient, C_B, can be derived by

$$C_B = \frac{\sqrt{\tau_x^2 + \tau_y^2}}{\rho\bar{u}_0 z_i} \tag{5.9}$$

where τ_x and τ_y are the Reynolds stress tensors. In a similar way to Smith (2010), the transfer coefficient between the boundary layer and the air aloft, C_T, is assumed to be the same as the C_B. The linear model is used to recreate the simulations from BLASIUS, as described in section 4. As a summary, a domain of 400 km with 1 km resolution is used. A wind farm consisting of 20 turbines is positioned in the centre of the domain, with a turbine density of $n = 10^{-6}\,\mathrm{m}^{-2}$.

Using the equations described in this section, the wind turbine linear model has been written. Running the linear model produces perturbation fields of horizontal velocity, pressure and temperature inversion displacement. These fields can be compared with BLASIUS to determine the accuracy of the linear model.

5.2.2 Post-processing BLASIUS data

In the interest of comparing the BLASIUS results to those derived in the linear model, analysis of the maximum velocity perturbation within the wind farm is carried out. A key result from Smith (2010) is that as Fr increases then the velocity within the wind farm has a greater region of deceleration during the wind farm before accelerating again. This is due to the negative pressure gradient through the wind farm with a small Fr. Furthermore, being able to determine the position of the minimum velocity within the wind farm has uses within the wind energy sector. The location of the minimum velocity in the linear model is denoted χ_*, with x_* being the minimum velocity location in BLASIUS. The velocity amplitude in the linear model is $\hat{\zeta} = \zeta(x = 0) - \zeta(\chi_*)$ and in BLASIUS the velocity amplitude is $\hat{u} = \bar{U}(x = 0) - \bar{U}(x_*)$. In both cases $x = 0$ represents the upstream edge of the model domains. The pressure gradient in the linear model is defined as $\nabla\gamma = (\gamma(W_d) - \gamma(W_u))W_X^{-1}$ where W_d and W_u are the downstream and upstream edge of the wind farm. Likewise, the pressure gradient in BLASIUS is $\nabla p = (p(W_d) - p(W_u))W_X^{-1}$. The boundary layer displacements in the linear model and BLASIUS are η_L and η_B. In BLASIUS, these are measured by calculating a streamline at the top of the inversion layer; the point where the boundary layer contacts the air aloft. For the purpose of comparing the linear

model and BLASIUS the following statistics will be used.

$$\delta\, x_* = \chi_* - x_* \tag{5.10a}$$

$$\delta\, \hat{u} = \hat{\zeta} - \hat{u} \tag{5.10b}$$

$$\nabla\, P = \nabla\gamma - \nabla p \tag{5.10c}$$

$$\delta\eta = \eta_L - \eta_B \tag{5.10d}$$

5.3 Differences in the representation of the wind turbine drag terms

The linear model of Smith (2010) uses the depth averaged velocity from the 1-d run, $\bar{u}_0$, in order to calculate the drag associated with each wind turbine

$$F_T = \frac{1}{2}\rho \mathrm{C}_D \bar{u}_0^2 A. \tag{5.11}$$

During initial investigations, limitations to the turbine drag in the linear model were observed. These are split into two distinct areas: the first being the velocity used in the linear model for calculating the turbine drag and secondly is how the linear model distributes the turbine drag within the boundary layer.

5.3.1 Diagnosing the wind turbine drag in the linear model

The numerical simulations carried out in BLASIUS use a non-slip lower boundary condition causing a logarithmic velocity profile through the boundary layer. The linear model uses a single depth-averaged velocity which is diagnosed from the 1-d simulation. This boundary layer velocity is larger than the velocity observed at hub height, which when used in calculating the turbine drag, produces a larger than realistic drag per turbine. For the linear model to be used as an independent tool, a scaled turbine drag term should be used to account for the smaller velocity at hub height compared to the boundary layer depth averaged velocity.

To do this we use the logarithmic wind profile

$$u = \frac{u_*}{\kappa} \ln\left(\frac{z}{z_0}\right) \tag{5.12}$$

where $u_* = \sqrt{\tau/\rho}$ is the surface friction velocity, $\kappa = 0.04$ is the Von-Karman constant and z_0 is the surface roughness length. Combining (5.12) with (5.9), and using $\tau = \sqrt{\tau_x^2 + \tau_y^2}$, gives

$$u = \frac{1}{4\kappa} \left(C_B z_i \bar{u}_0\right)^{\frac{1}{2}} \ln\left(\frac{z}{z_0}\right). \tag{5.13}$$

The logarithmic wind profile is used for near surface winds, where there are greater effects from the surface friction. The wind turbines used in this study have a hub height of $z_h = 95\,\mathrm{m}$, which is representative of an operational wind turbine hub height. Simulations in BLASIUS showed this to be above the near surface and hence a scaling term in added to the logarithmic velocity profile. The hub height velocity (μ) is therefore given by

$$\mu = \frac{B}{\kappa} z_h^m \left(C_B z_i \bar{u}_0\right)^{\frac{1}{2}} \ln\left(\frac{z}{z_0}\right) \tag{5.14}$$

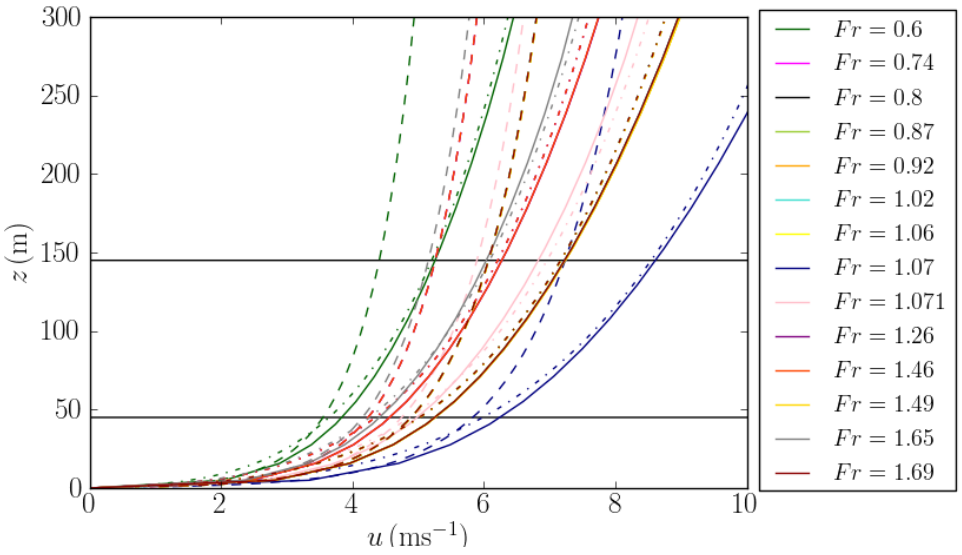

(a)

Figure 5.1: *The vertical profile of the horizontal velocity is shown for the BLASIUS simulations (solid line), the logarithmic profile in equation (5.13) (dashed) and the scale logarithmic profile in equation (5.14) (dotted). The wind farm area in these simulation is shown by the solid black lines.*

with the empirically derived $m = 0.12$ and $B = 0.16$. The velocity profiles of BLASIUS and equations (5.13) and (5.14) are shown in figure 5.1. It can be seen

that near the surface, BLASIUS and equation (5.13) give the same velocities, however for increasing z they diverge. The difference within the wind farm area reaches $1.5\,\mathrm{m\,s^{-1}}$. Using the scaled log profile in equation (5.14) there is greater convergence with the BLASIUS profile through the wind farm area. Using μ to calculate the turbine drag in the linear model is a more appropriate velocity compared to the boundary layer average velocity $\bar{u}_0$.

The linear model has been run with three different drag terms, for comparison with BLASIUS. The first of these calculates the turbine drag from the initialised boundary layer velocity, $F_T(\bar{u}_0)$. This is the method used in Smith (2010). The next method calculates the turbine drag based on the scaled velocity term μ in 5.14. The final method of running the linear model used the same drag term as used in the corresponding BLASIUS simulation. This has been done by calculating the average drag from one turbine in the final $15,000$ seconds of the simulation. The linear model with diagnosed turbine drag from BLASIUS acts as the control simulation.

Figures 5.2, 5.3 and 5.4 show the velocity perturbations in the linear model and BLASIUS for three different initialised conditions. Initial observations show that there are difference between the velocity perturbations in BLASIUS and those from the linear model simulations. The reason for these differences will be discussed in sections 5.4. Of interest in these plots is how changing the turbine drag in the linear model changes the boundary layer perturbations. In figures 5.2(a), 5.3(a) and 5.4(a), there is a large velocity perturbations with the turbine drag is calculated from the average boundary layer velocity $F_T(\bar{u}_0)$, much larger than when the turbine drag is diagnosed from BLASIUS. Running the linear model with the scaled drag term $F_T(\mu)$ yields a similar velocity perturbation to the control simulation. Scaling the velocity when calculating the turbine drag in the linear model improves the velocity perturbation in the linear model.

Moving to the pressure perturbations, a similar trend is observed, with the perturbation from $F_T(\bar{u}_0)$ giving the largest pressure gradient through the wind farm. Both the diagnosed drag and $F_T(\mu)$ produce the same pressure gradient through the wind farm and recovery to the free-stream pressure downstream of the wind farm. The individual features of the velocity and pressure perturbation will be discussed in section 5.4.

Based on this analysis, if the linear model is to be used in isolation, then the scaled velocity should be used to calculate the turbine drag. Using the average boundary layer velocity to calculate the turbine drag, as done in Smith (2010) will produce unrealistically large velocity and pressure perturbations. Adding equation 5.14 to the drag equation 5.11 gives the turbine drag F_{Tmod} which should be used when running the linear model

$$F_{Tmod} = \frac{1}{32\kappa^2}\rho C_D C_B z_h^{2m} z_i \bar{u}_0 A \left[\ln\left(\frac{z}{z_0}\right)\right]^2 . \tag{5.15}$$

For the purposes of these simulations, the drag in the linear model will be diagnosed from the BLASIUS simulation, therefore limiting any difference to the model dynamics and not the representation of the turbine drag.

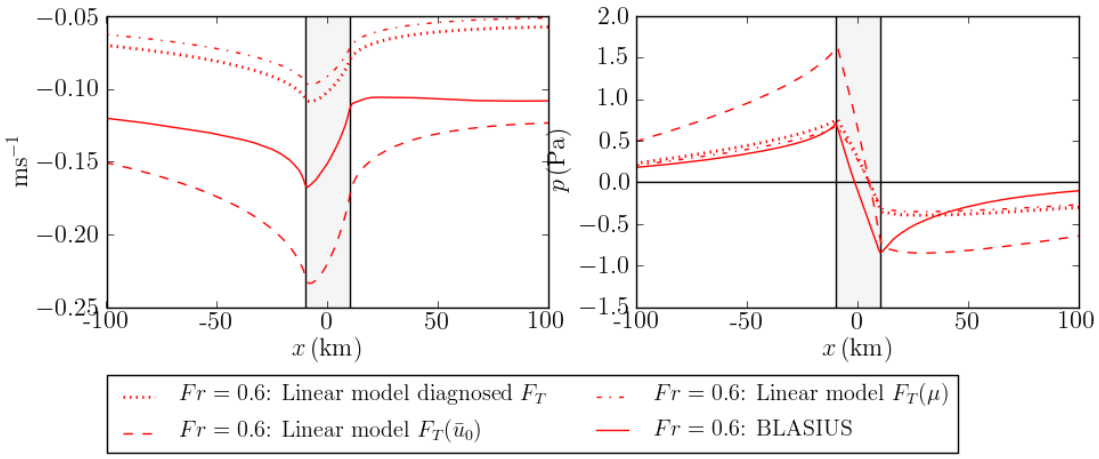

(a)

Figure 5.2: *Boundary layer perturbations for simulations with $Fr = 0.6$. Shown here are the velocity perturbations (a) and the pressure perturbations (b). The solid line shows the boundary layer perturbations from the BLASIUS simulations. The remaining lines show the perturbations from the linear model, with each plot representing a different turbine drag.*

5.3.2 Distribution of the wind turbine drag

A further difference associated with the turbine drag between the linear model and BLASIUS is the distribution of the drag within the boundary layer. BLASIUS confines the drag to the rotor area, however due to the single layer nature of

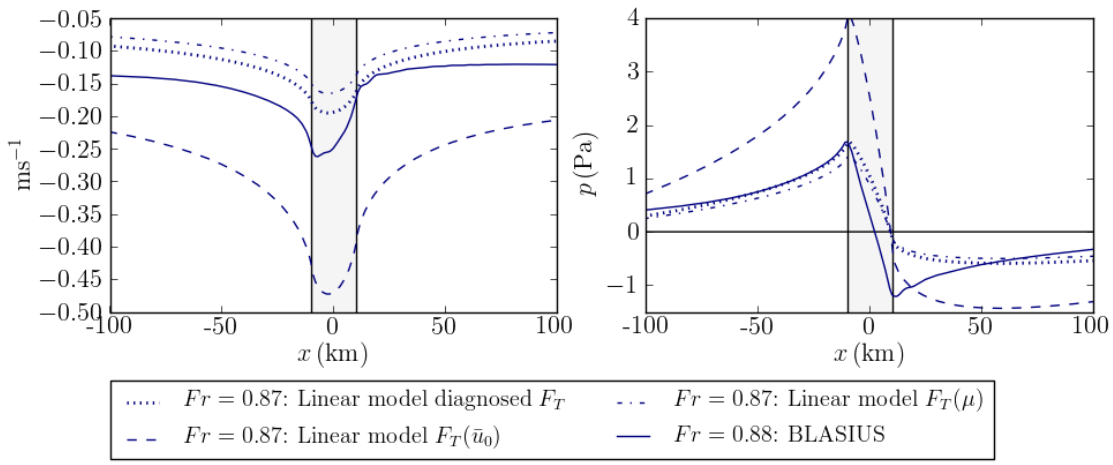

(a)

Figure 5.3: *As described in figure 5.2 but for* $Fr = 0.87$.

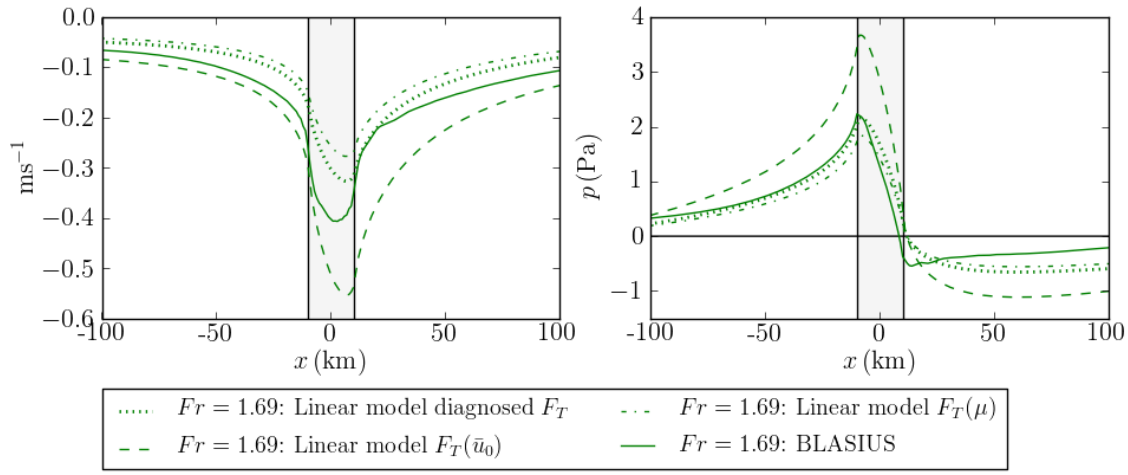

(a)

Figure 5.4: *As described in figure 5.2 but for* $Fr = 1.69$.

the linear model, the turbine drag is distributed uniformly within the depth of the boundary layer. In both models, the horizontal extent of the wind farm is identical. This is a significant limitation to the set up of the linear model, however it is not known how much difference this makes.

It is possible to change the turbine drag distribution within the BLASIUS model so that it replicates the linear model. The total drag from a turbine, F_T, is distributed uniformly so that the drag in each model level is given by $f_T(z)$ as shown in equation (5.16), where Z_T is the top of the turbine distribution height.

$$F_T = \frac{1}{z_i}\int_0^{z_T} f_T(z)\,\mathrm{d}z \tag{5.16}$$

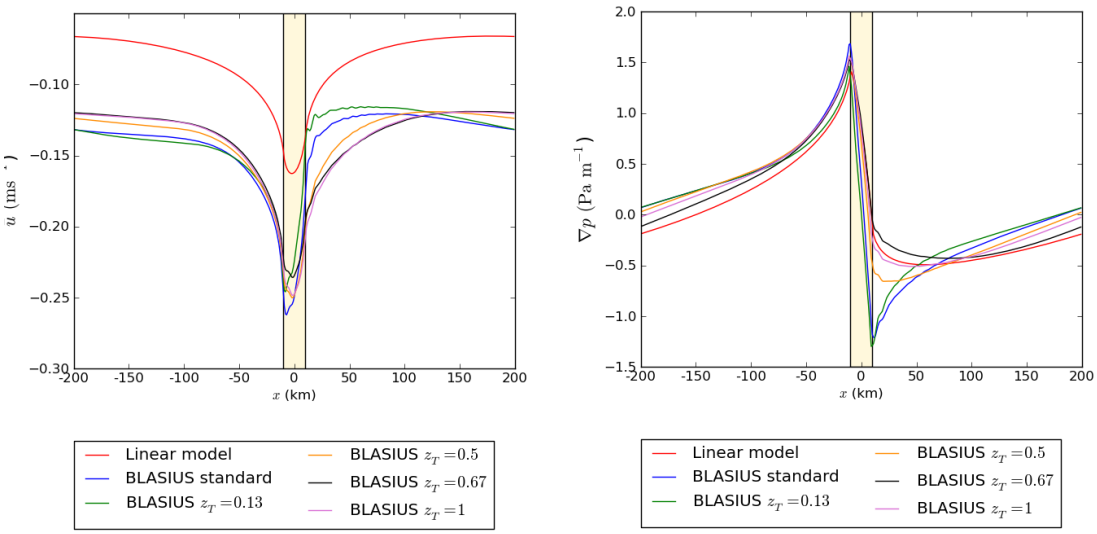

(a) **(b)**

Figure 5.5: *Figure (a) shows the velocity perturbation U for different values of wind turbine distribution height. The pressure gradient in the boundary layer is shown in figure (b). In both plots the vertical lines show the edges of the wind farm.*

Simulations were carried out with $Fr = 0.6$, $Fr = 0.87$ and $Fr = 1.69$ (see table 4.1). The distribution height of the turbine drag was increased up throughout the boundary layer reaching the maximum value of z_i. The difference in position of the minimum point within the wind farm, δx_*, is reduced as z_T increases, shown in figure 5.6(a). The greatest improvement in changing the turbine drag distribution is with the pressure gradient through the wind farm, figure 5.6(b). There is a clear trend of convergence to zero as the height is increased. In the lower drag distribution values there is a sharp pressure gradient through the wind farm however on the downstream edge of the wind farm there is a sudden change from negative to a positive pressure gradient. As the drag distribution height is increased then the pressure gradient within the wind farm becomes smoother downstream and behaves in a similar way to the pressure gradient in the linear model.

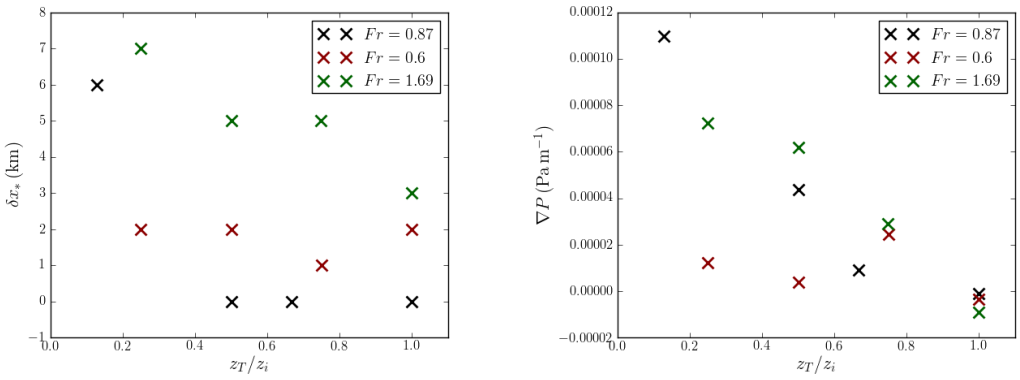

(a) **(b)**

Figure 5.6: *The difference in position of the velocity minimum, δx_* (a) and the pressure gradient ∇P (b) are shown above for simulations with $Fr = 0.6$, $Fr = 0.87$ and $Fr = 1.69$ and the turbine drag distribution increasing up though the boundary layer.*

5.4 Comparison between BLASIUS and linear model

The simulations described in table 4.1 are carried out in BLASIUS with the linear model run for each case, initialised from the corresponding 1-d run. Comparisons between the two models can be made from the velocity minimum using equations (5.10).

5.4.1 Analysis of the point of maximum perturbation

Figure 5.7 shows that as Fr increases then the positions of the minimum velocity, x_* and χ_*, also increase. For the simulations with $Fr = 1.46\,\&\,1.69$ there is an increase in $\bar{u}_0$ causing an increase in Fr, however x_* decreases as Fr increases. This is in contrast to other pairs of BLASIUS simulations. The reason for this decrease is in the $Fr = 1.69$, simulation the velocity reaches its minimum 11 km into the wind farm however maintains a velocity near the minimum velocity for the next 4 km. There is only a 1 km difference in x_* between the $Fr = 1.46\,\&\,1.69$ simulations and this could also be due to the resolution choice of 1 km.

The simulations $Fr = 0.8, 1.02,\,\&\,1.69$, $Fr = 0.74\,\&\,1.26$ and $Fr = 0.87\,\&\,1.06$

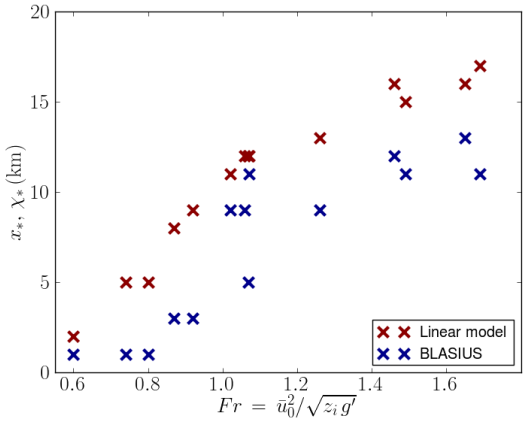

(a)

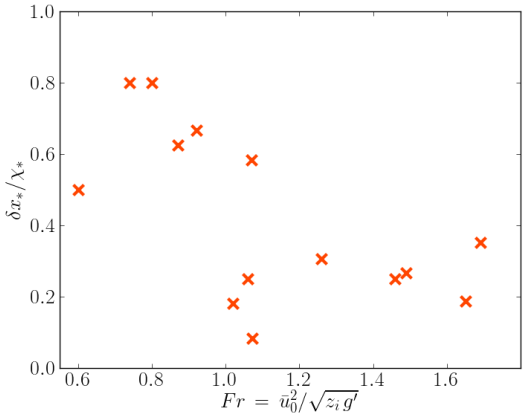

(b)

Figure 5.7: *The position of the velocity minimum in both the linear model and BLASIUS is shown in (a). The normalised difference between the two models is shown in (b).*

have equal $\bar{u}_0$ and z_i yet have different θ_i values. In these cases the increase in Fr caused by decreasing θ_i results in an increase in x_*. These changes in x_* are attributed to the changes in pressure gradient through the wind farm, with the pressure gradient decreasing as Fr increases (figure 5.8a). Larger pressure gradients act by decreasing x_*.

Furthermore, the simulations $Fr = 0.74\,\&\,1.02$ have equal $\bar{u}_0$ and θ_i with an increase in Fr being the result of decreasing z_i. In this case there is also an increase in x_*. However, there are cases when θ_i is increased yet z_i is decreased, as demonstrated by the simulations $Fr = 0.74\,\&\,0.8$ and $Fr = 1.02\,\&\,1.26$, where x_* remains constant. In both these cases the magnitude increase in x_* by halving z_i is equal to the x_* decrease caused by increasing θ_i by ≈ 2 K. Using an appro-

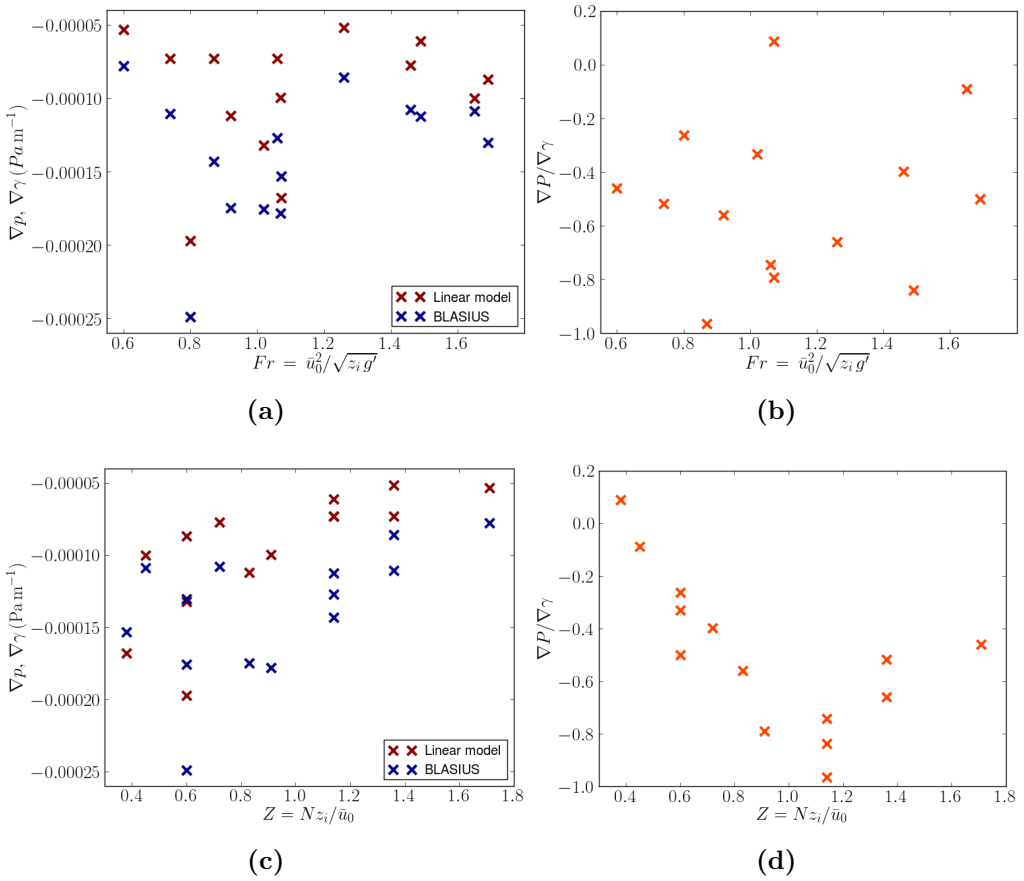

Figure 5.8: *The effect of Fr and Z on the pressure gradient through the wind farm is shown for the linear model and BLASIUS (a). The differences between the two models are shown in (b) and (d).*

priate normalising factor, the linear model and BLASIUS can be compared using the statistics defined in equation (5.10). As Fr increases then there is greater agreement between χ_* and x_* (figure 5.7(b)). It should be observed that χ_* increases with Fr and hence δx_* does not significantly change as Fr increases. On a further note, figure 5.7(a) shows that for all Fr, $\chi_* > x_*$. This is a result of the drag distribution differences as described in section 5.3.1.

In summary, the distribution of drag in the linear model up to the boundary layer top imposes a less dense drag force on the flow. This results in the flow propagating further through the wind farm before the minimum velocity occurs. In contrast, the more dense drag in BLASIUS slows the flow at a greater rate. It should also be noted that in both the linear model and BLASIUS, χ_* and x_* do not occur at the final wind turbine in the array. This shows that the

pressure gradient imposed on the flow as a result of the drag force within the boundary layer counteracts the drag force from the wind turbines. With a lower Fr value there is a weaker flow velocity and hence a smaller combined drag from the turbines is required to reach χ_* and x_*.

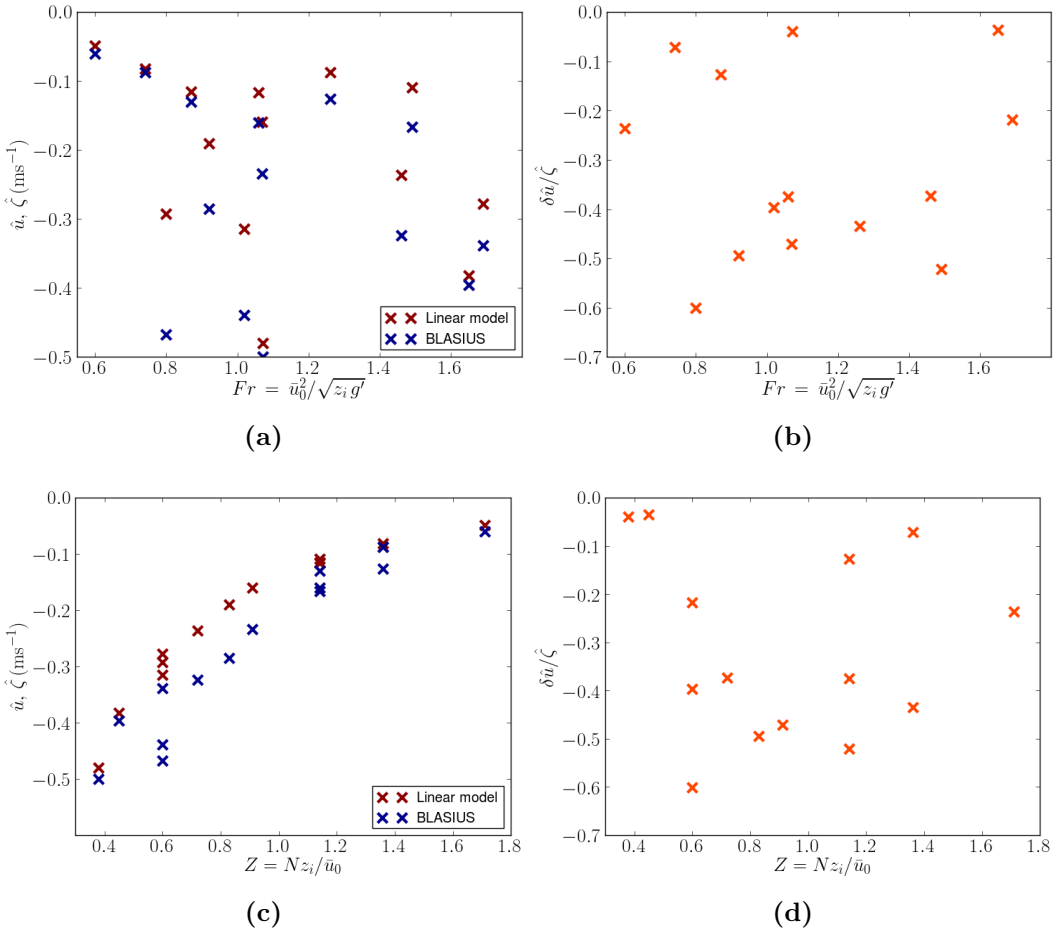

Figure 5.9: *The change in velocity amplitude within the wind farm, $\hat{u}$ and $\hat{\zeta}$, is shown in relation to Fr, figure (a), and Z, figure (c). The differences between the linear model and BLASIUS are in relation to Fr and Z are shown in figs. (b) and (d). The difference in amplitude $\delta\hat{u}$ is normalised against the linear model velocity amplitude $\hat{\zeta}$.*

The changes in velocity amplitude within the wind farm compared to the upstream velocity are shown in figure 5.9. Looking at the BLASIUS simulations with high $Fr > 1.2$ and low $Fr < 0.8$ the amplitude $\hat{u}$ becomes more negative as Fr increases. For $0.8 \leq Fr < 1.1$ there is a large range in amplitudes with no clear trend. This shows that there are changes in the amplitude as the flow

changes from sub-critical to super-critical flow. Although this may highlight errors in calculating Fr from the 1-d run, chapter 4 showed that changes in Fr mainly influence the flow at the front of the wind farm. Changes in boundary layer height z_i have a greater impact on the flow than changes in the Froude number. In figure 5.9(a), simulations $Fr = 0.8$, $Fr = 1.02$ and $Fr = 1.071$ show larger (more negative) $\hat{u}$ and $\hat{\zeta}$ values than simulations of similar Fr. Table 4.1 shows that these simulations have $z_i \leq 715\,\mathrm{m}$. Section 4.3.6 showed that lower z_i increased the interaction between the wind farm wake and the boundary layer capping layer. This interaction changes the velocity amplitude within the wind farm for all simulations with lower boundary layer heights. When $z_i = 1364\,\mathrm{m}$, $\hat{u}$ and $\hat{\zeta}$ increase the magnitude of the velocity amplitude as Fr increases, however the opposite occurs for $z_i = 715\,\mathrm{m}$. Figure 5.9(b) shows that there is a large spread in agreement between the linear model and BLASIUS. Once again by looking at difference z_i cases, it can be seen that $\delta\hat{u}/\hat{\zeta}$ becomes more negative as Fr increases for $z_i = 1364\,\mathrm{m}$, increases for $z_i = 715\,\mathrm{m}$ and remains constant for $z_i = 452\,\mathrm{m}$.

Changes in z_i between simulations are represented better with Z. Figure 5.9(c) shows the velocity amplitude changes systematically with Z. It shows that as Z increases then $\hat{u}$ becomes less negative. The simulations with $Z = 0.72$ and 0.83 and 0.91 all have varying U, z_i and θ_i (as shown in table 4.1) and in turn show a range of $\hat{u}$ values which do not become less negative as Z increases. This shows that although there is a strong trend with all simulations, there are still other factors that determine $\hat{u}$.

A small Z value implies that vertically propagating waves have a greater impact on the flow. The source of vertically propagating waves in these simulations is the displacement of the capping inversion above the boundary layer. The deceleration of the flow through the wind farm causes an increase in the boundary due to mass conservation. Figure 5.10(a) shows how η_B and η_L decrease as Z increases, showing the inversion displacement is the cause of waves in the air aloft. The linear model captures the same changes in the inversion displacement, as shown in figure 5.10(b).

Changes in $\hat{\zeta}$, as is the case with $\hat{u}$, are explained when the simulations are identified according to their Z value. In the linear model $\hat{\zeta}$ also becomes less negative as Z increases, (figure 5.9(c)), a result of η_L increasing as Z decreases (figure 5.10(a)). Figure 5.11 shows that a greater difference in amplitude, $\delta\hat{u}$, then

there is a greater difference in inversion displacement, $\delta\eta$. This is further proof that the velocity amplitude is proportional to the inversion displacement, meaning it is mass conservation which influences the changes to the boundary layer height. It is challenging to see from figure 5.11 which is the cause for these changes, and whether it is due to the simplicity of the linear model. Figure 5.9(d) shows that as Z increases then the difference between the linear model and BLASIUS decreases. Using the Pearson correlation coefficient ($\rho_{X,Y} = \mathrm{cov}(X,Y)/(\sigma_X\sigma_Y)$), Z and $\delta\hat{u}/\hat{\zeta}$ have a value of $p = 0.52$. This shows positive correlation, although given the spread of data in figure 5.9(d) they are weakly correlated.

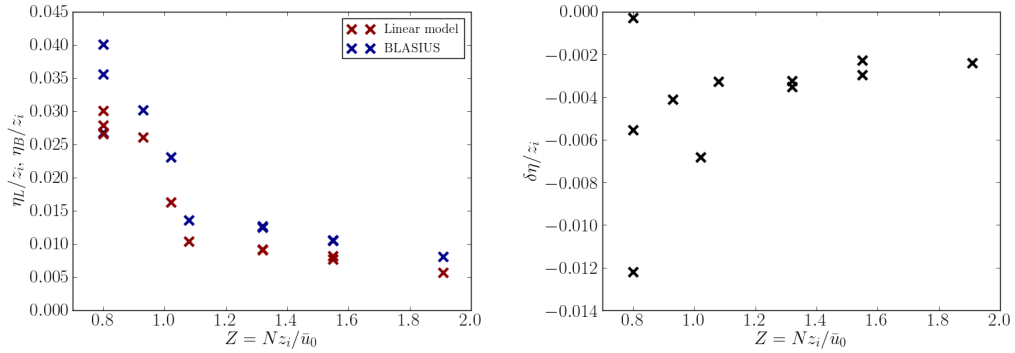

(a) **(b)**

Figure 5.10: *Figure (a) shows the inversion displacements in BLASIUS (η_B) and the linear model (η_L) as a ratio against the respective 1-d run inversion height z_i. The difference $\delta\eta$ between the linear model and BLASIUS is shown in figure (b).*

The effects of Fr and Z on ∇p are shown in figure 5.8. As has been the case for the effect of changing Fr there is ambiguity around $Fr \approx 1$. The error in the two models with Fr shows no direct impact from changing Fr. This, however, has been shown to be due to the distribution of the turbine drag in the linear model (section 5.3) and also due to the changes in z_i. Figure 5.8(c) shows that as Z increases then $|\nabla p|$ decreases, however maintaining a negative pressure gradient in the direction of the flow. This provides evidence of the link between the negative pressure gradient and the velocity amplitude through the wind farm. A small Z implies that there is a more negative ∇p. The pressure gradient is a result of the inversion displacement which causes gravity waves.

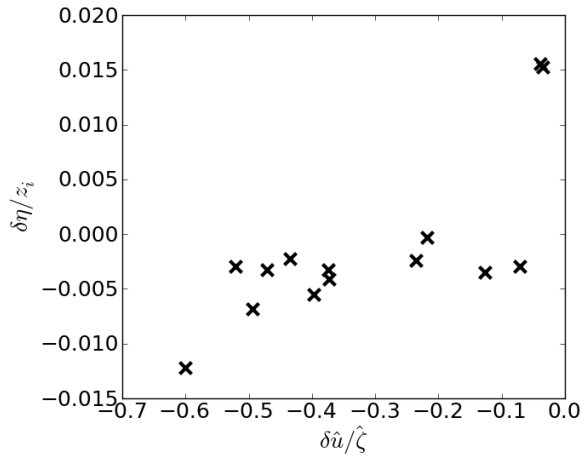

(a)

Figure 5.11: *The differences between the velocity amplitude $\delta\hat{u}$ are compared against the differences in the inversion displacement $\delta\eta$. The inversion displacement is measured as a ratio of the initial boundary layer height z_i and the amplitude is normalised with the linear model amplitude $\hat{\zeta}$.*

The pressure gradient in the linear model shows similar trends to BLASIUS with respect to changing Fr and Z. For all simulations $|\nabla\gamma| \leq |\nabla p|$ hence a weaker force opposing the drag from the wind turbines in the linear model. The reason for $x_* \leq \chi_*$ can also be explained by the changes to pressure gradient. With $\nabla p \leq \nabla\gamma$ there is a greater pressure gradient against the direction of the flow in BLASIUS. The minimum velocity is further forward in BLASIUS due to the greater pressure gradient which occurs. In some simulations $\nabla P/\nabla\gamma \approx 1$, which is a consequence of the drag distribution differences between the two models (shown in figure 5.6(b)).

5.5 Altering the depth of the wind farm

The results in section 5.4.1 only considered wind farms consisting of 20 turbines in the streamwise direction. Another interesting question is how does the wind farm size (W_X) affect firstly the minimum velocity in BLASIUS and secondly the agreement between BLASIUS and the linear model? The linear model represents the boundary layer as a single layer horizontal flow. In order for the wind farm to influence this deep single layer it is assumed that the wind farm must be large

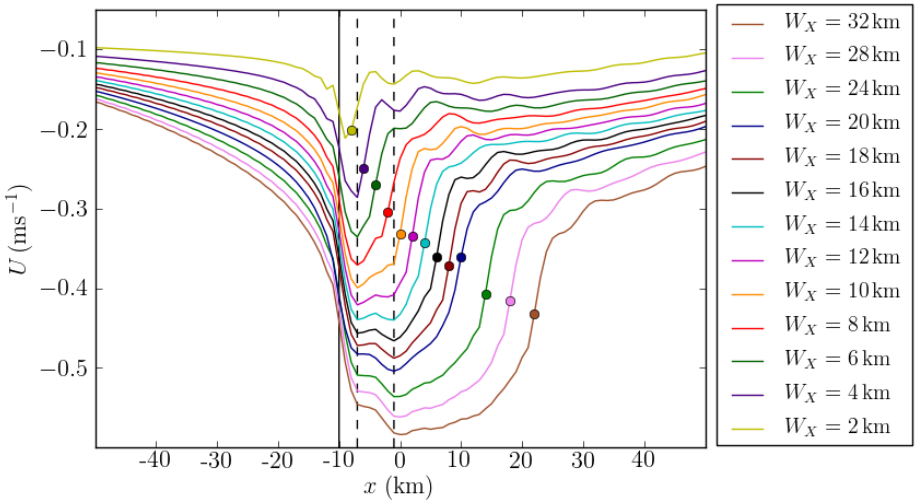

Figure 5.12: *The boundary layer velocity in BLASIUS, U, is shown for each simulation with increasing wind farm depth W_x. The coloured dots show the position of the final wind turbine in each of the simulations, with the front of all wind farms being shown by the solid black line. The dotted black lines show the position of the third and ninth wind turbine in all of the simulations.*

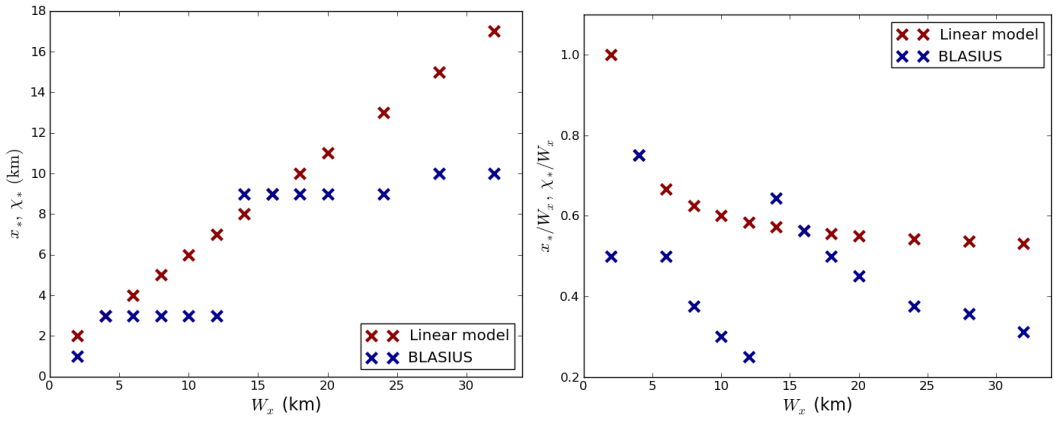

(a) **(b)**

Figure 5.13: *Plot (a) shows the distance within the wind farm of the minimum depth averaged velocity in both the linear model (red) and BLASIUS (blue) when the depth of the wind farm decreases from 20 km deep to 2 km deep. The metric is aligned with the direction of the velocity flow with 0 km being the upstream edge of the wind farm. The ratio of x_* and χ_* with respect to the wind farm depth W_x is shown in figure (b).*

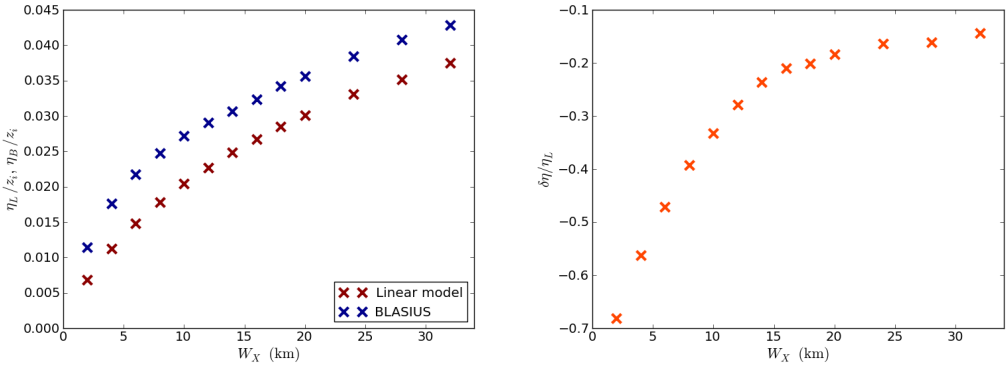

(a) **(b)**

Figure 5.14: *The inversion displacement in the linear model and BLASIUS for changing W_X is shows in figure (a). The difference between the two models normalised with the displacement in the linear model (η_L) is shown in figure (b).*

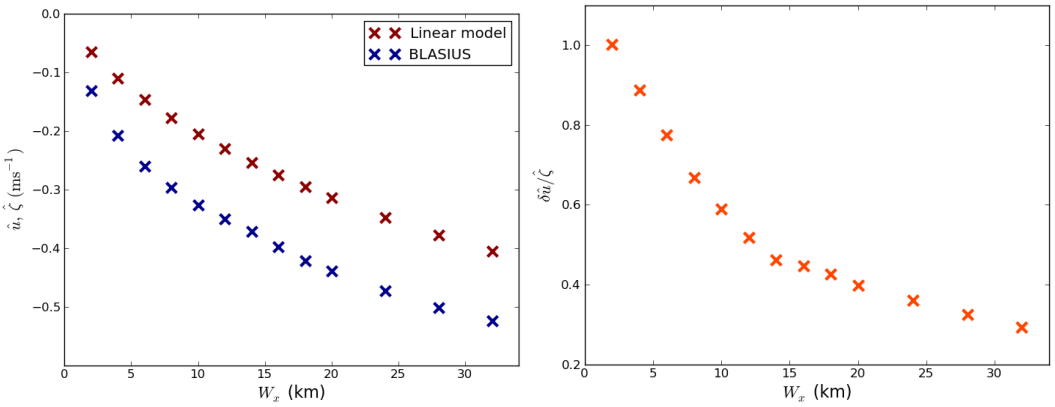

(a) **(b)**

Figure 5.15: *The difference between the amplitude of the velocity perturbation in the linear model (red) and BLASIUS (blue) is shown in figure (a). The amplitude in the linear model is defined as $\hat{\zeta} = \zeta(\chi = 0) - \zeta(\chi_*)$. The amplitude in BLASIUS is defined as $\hat{U} = U(x = 0) - U(x_*)$. Plot (b) shows the normalised difference between the linear model and BLASIUS, where $\delta\hat{u} = \hat{\zeta} - \hat{U}$. As in figure 5.13, the wind farm depth is modified between the simulations.*

with the interaction from multiple wind turbines influencing the boundary layer flow. In this section we test this assumption.

BLASIUS simulations are carried out with constant initial conditions set from the 1-d run. The simulations have $Fr = 1.02$ and $Z = 0.8$. This simulation is chosen

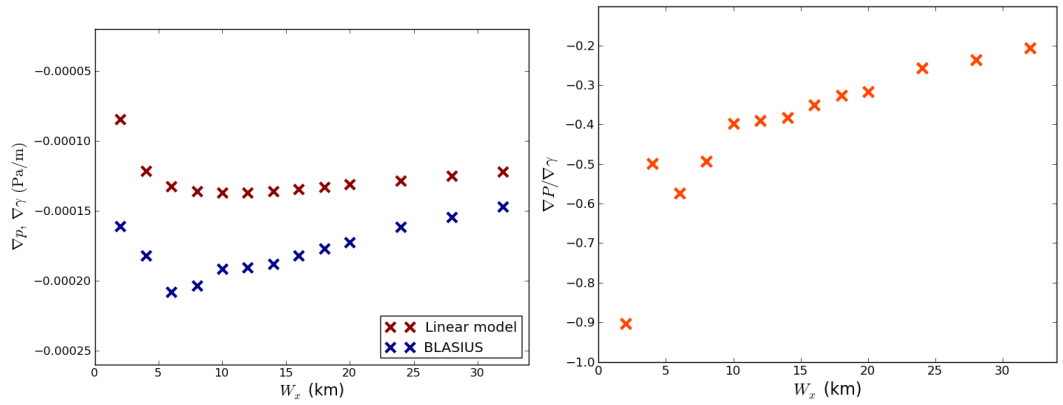

(a) **(b)**

Figure 5.16: *Figure (a) shows how the pressure gradient changes through the wind farm when the depth of the farm is changed in both the linear model and BLASIUS. The difference between the models is shown in (b), normalised with the pressure gradient in the linear model $\nabla\gamma$.*

as firstly it has Fr in the middle of possible ranges and thus testing how δx_* is affected. Secondly, the simulation has the lowest Z and hence is one of the flows affected the most by gravity waves. Considering the gravity waves are generated by the drag imposed from the wind farm it is of interest to see how reducing the cumulative drag from a wind farm impacts on the generation of gravity waves in the linear model.

Firstly, from figure 5.12 it can be seen that as W_X increases then the reduction of the depth averaged velocity U through the wind farm increases. This is a result of the greater total drag from the larger wind farm. Although the total drag in the wind farm increases with W_X, the drag per turbine decreases in the BLASIUS simulations. The drag per turbine in the $W_X = 32\,\text{km}$ case is 14 % smaller than with $W_X = 2\,\text{km}$. In the majority of simulations, troughs in U are observed at $x = -7\,\text{km}$ and $x = -1\,\text{km}$, i.e. at the third and ninth turbines in the arrays. These troughs have an influence on δx_* as explained later. Downstream of the wind farms, stationary waves can be observed, which decay by 50 km. Upstream of the wind farms, there is a decrease in U. This is due to the pressure gradient caused by the gravity waves in the air aloft. The larger the wind farm, then the greater the upstream velocity decrease, a result of the greater $\hat{u}$ causing a greater inversion displacement (figure 5.14).

The changes in both χ_* and x_* are shown in figure 5.13. It should be noted that the differences in the drag in the BLASIUS simualtions are replicated in the linear model, ensuring parity between the models. There is a linear increase in χ_* as W_X increases, with the position of χ_* relative to W_X remaining constant as $W_X \geq 10\,\text{km}$. This shows that there is an adjustment period with χ_* for smaller wind farms. With the BLASIUS simulations, x_* is on or around the two troughs identified in figure 5.12. This oscillatory pattern to U in BLASIUS is not resolved in the linear model.

As previously shown in figure 5.12, both $\hat{u}$ and $\hat{\zeta}$ become more negative as W_X increases. This is due to the increase in total drag from the wind farm and is linked with the inversion displacement, whereby a greater $|\hat{u}|$ and $|\hat{\zeta}|$ values a result of greater η_B and η_L. For all W_X, $|\hat{\zeta}| < |\hat{u}|$. This is the same trend which was shown in section 5.4.1, and thus is a consistent difference between the linear model and BLASIUS. Figure 5.15(b) shows that the difference decreases as W_X increases, but considering $|\hat{\zeta}|$ increases then the difference between the linear model and BLASIUS remains constant for all W_X. For $W_X \geq 10\,\text{km}$ there is a reduction in the gradient of $\delta\hat{u}/\hat{\zeta}$ compared to smaller W_X values. This is the point at which $\delta\hat{u}$ remains constant.

The changes to the pressure gradients are shown in figure 5.16. As W_X increases there is an initial increase in the magnitude of the pressure gradients ∇p and $\nabla\gamma$. For $W_X \geq 5\,\text{km}$, $\nabla\gamma$ remains constant whereas ∇p decreases in magnitude. That is except for $W_X = 20\,\text{km}$ whereby there is a sudden decrease in magnitude of pressure gradient. The ranges of both $\nabla\gamma$ and ∇p are smaller than observed in section 5.4.1 for the different Fr simulations. This implies that for $W_X \geq 10\,\text{km}$ the pressure gradient in the linear model and BLASIUS is determined by the upstream flow conditions, namely Fr. This is to be expected as Fr is an indication of the generation of gravity waves which are the cause of the negative pressure gradient through the wind farm. Smith (2010) implied that the wind farm would need to be large in order for the velocity deficit to cause gravity waves and thus a pressure field in the boundary layer. Figure 5.8 shows that an adequate pressure field is generated by wind farms greater than 5 km in depth. Furthermore, section 4.4 showed that at $W_X = 6\,\text{km}$, the wind farm turbulence extends to the top of the boundary layer. This is the point at which the wind farm wake has evolved to its maximum size, with increases in W_X making no further changes. This is evident in the pressure gradients and explains the adjustment

period for small W_X. Modern wind farms are larger than this and thus a pressure field under these atmospheric conditions is likely to be generated.

5.6 Wind farm stalling

An interesting feature from Smith (2010) is the turbine drag being sufficient to significantly reduce the velocity within the wind farm. A sudden reduction is likely to reduce the velocity to below the cut in speed for downwind turbines. To achieve this we take the limit of $Z \to 0$ with $Fr = 1$ and so $N \to 0$. This then increases the static stability in the air aloft which ensures that the boundary layer inversion acts as a rigid lid. There is therefore no inversion displacement $\eta = 0$. To test this phenomenon, two test cases in BLASIUS are used, shown in table 5.1. These test cases have been chosen as $Fr \approx 1$.

Fr	Z	$\bar{u}_0\,(\mathrm{m\,s^{-1}})$	$z_i\,(\mathrm{m})$	$\theta_i\,(\mathrm{K})$
0.90	0.09	7.7	715	3
0.93	0.09	6.5	452	3

Table 5.1: *Boundary layer profile statistics from the 1-d runs with* $N = 0.001\,\mathrm{s^{-1}}$

The BLASIUS simulations are set up in the same way as described in section 5.2, with the buoyancy frequency changed to $N = 0.001\,\mathrm{s^{-1}}$. Simulations are run for $65,000$ seconds of model time and averaged over the final $10,000$ seconds. This ensures a steady state flow is analysed. As was carried out in section 5.4.1, the minimum velocity point within the wind farm will be compared between BLASIUS and the linear model.

Fr	χ_*	x_*	δx_*	$\hat{\zeta}$	$\hat{u}$	$\delta\hat{u}$
0.90	9 km	10 km	−1 km	$0.36\,\mathrm{m\,s^{-1}}$	$1.14\,\mathrm{m\,s^{-1}}$	−0.79
0.95	8 km	5 km	3 km	$0.21\,\mathrm{m\,s^{-1}}$	$1.15\,\mathrm{m\,s^{-1}}$	−0.94

Table 5.2: *Minimum point analysis for simulations with* $N = 0.001\,\mathrm{s^{-1}}$*. The position of the minimum velocity and its amplitude are shown.*

Table 5.2 shows the minimum velocity point statistics in both the linear model and BLASIUS. Firstly, there is agreement in the position of the minimum velocity in the two cases. Interestingly, $Fr = 0.9$ has a minimum point further through

Fr	$\nabla p_L\,(\mathrm{Pa\,m^{-1}})$	$\nabla p_B\,(\mathrm{Pa\,m^{-1}})$
0.90	-1.4×10^{-4}	-1.2×10^{-4}
0.95	-1.0×10^{-4}	-1.5×10^{-4}

Table 5.3: *Pressure gradients for simulation with $N = 0.001\,\mathrm{s^{-1}}$ in the linear model and BLASIUS.*

the wind farm than the linear model; this is different to all other BLASIUS simulations. These values are not significantly different to the previous simulations with $N = 0.01\,\mathrm{s^{-1}}$. The main difference however is in the amplitude of the wind farm velocity. The linear model displays slightly larger $\hat{\zeta}$ that for the standard stability cases, with the decrease in velocity less than shown in Smith (2010). The BLASIUS simulations do show the choking effect. Both cases show large velocity decreases within the wind farm, shown by the $\hat{u}$ values. Both cases show similar agreement between the linear model and BLASIUS. The pressure gradients are not significantly different between the two models, with any difference no worse that the standard stability simulations.

The choking effect described in Smith (2010) has been shown to occur in BLASIUS simulations with similar Froude number. The velocity decrease is larger in the BLASIUS simulations compared to the linear model. Considering these simulations have $Fr < 1$, this is either due to errors in calculating Fr or due to the wind turbines being in the lower part of the boundary layer. The Froude number is calculated from the 1-d simulation and the boundary layer evolves during the 2-d run, whereas the linear model does not. With these Froude numbers it is not unlikely for the linear model to not show the wind farm choking. Its presence in the BLASIUS simulations shows that such a phenomenon can occur, with maybe less sensitivity to Fr as shown in the linear model. In these BLASIUS simulations, the wind farm velocity does not go below the cut in speed and hence the wind farms remain operational.

5.7 Summary

This work has compared the linear model in Smith (2010) to the Met Office BLASIUS model for flow through a wind farm in a neutral boundary layer capped by

a temperature inversion. This has been done by looking at the minimum velocity within the wind farm, both in terms of its position and velocity amplitude. The pressure gradients through the wind farm have also been examined as a way of comparing both models. Non-dimensional parameters Fr and Z are used to describe the dynamics of the different simulations carried out.

The turbine drag in the linear model is over estimated due to $\bar{u}_0$ being used in the calculation of F_T. Using a modified velocity, as shown in equation (5.14), the turbine drag in the linear model is improved. For more accurate comparison between the linear model and BLASIUS, the turbine drag is best diagnosed directly from BLASIUS. Furthermore, the turbine drag in the linear model is distributed uniformly up to the temperature inversion, whereas in BLASIUS it is in the lower portion of the boundary layer within the wind turbine rotor area. This causes a discrepancy between the two models. Increasing the height at which the turbine drag is distributed, z_T, in BLASIUS decreases δx_* and ∇P.

It has been found that the linear model makes a good prediction of the position of the velocity minimum within the wind farm with respect to changing Fr. As Fr increases, then χ_* and x_* increase with $\delta x' > 0$. This is a result of the drag distribution whereby the lower drag density in the boundary layer in the linear model increases the distance at which the minimum is reached. The amplitude of the velocity perturbation is dependant on Z with a large Z value resulting in $|\hat{\zeta}| \leq |\hat{u}|$. A small value of Z implies that there is a larger inversion displacement in the linear model and BLASIUS which is a result of a greater velocity deficit. A greater amplitude relates to a greater pressure gradient through the wind farm. It is this pressure gradient which causes the velocity to accelerate in the latter part of the wind farm, even though there is the same drag being added from the wind turbine.

The linear model agrees well with BLASIUS for different wind farm sizes. In the linear model, χ_* increases linearly with increasing W_X however BLASIUS displays waves in U through the wind farm resulting it large δx_* for some W_X. The agreement between the linear model and BLASIUS with the velocity amplitude does not significantly change as W_X changes. The magnitude of $\hat{\zeta}$ is less than the magnitude of $\hat{u}$ which is a consistent feature of the linear model. The pressure gradient does not significantly change in the linear model and BLASIUS for $W_X \geq 6\,\text{km}$, showing that flow parameters determine the pressure gradient and not wind farm size.

In conclusion, the linear model in Smith (2010) shows similar flow behaviour as BLASIUS for flow through a neutral boundary layer. The assumption that the linear model is only valid for large wind farms does not appear to be the case, with smaller wind farms showing the same agreement with BLASIUS as their larger counterparts. Prior to using the linear model the non-dimensional parameters Fr and Z must be known in order to be aware of the limitations of the linear model with respect to the flow through the wind farm. Using these results, it is possible to use the linear model to analyse the pressure field and thus gravity waves caused by a wind farm.

Chapter 6

Impact of a wind farm on sea breezes

6.1 Introduction

The sea breeze is a meteorological phenomenon which occurs along coastlines. During the year, land and water bodies increase in temperature at different rates. There are also changes in the daytime temperature between the land and sea, caused by the large thermal mass in the sea. The land becomes warmer in the day, and subsequently cooler in the night. Other features such an clouds, vegetation and synoptic conditions can affect these temperature differences, with this description applying to a calm day with little to no clouds. These temperature differences are the driver for the sea breeze formation.

As the surface heats up, there is an increase in temperature in the air near the surface. Due to convective currents, this temperature increase is distributed within the lowest 1 km to 2 km, (Simpson, 1994). There is a height at which no more temperature increases occur, causing sideways expansion of the column of air over the land. This initiates a pressure difference between the air over the land and the sea. This pressure difference is sufficient to cause a flow from the sea to the land near the surface, with a weaker return flow from land to sea in the air aloft (Simpson, 1987).

A sea breeze is a type of gravity current. Gravity currents occur where two horizontally separated fluids of different density flow past each other. The density

changes in a sea breeze are brought about from the changes in temperature, with temperature changes being inversely proportional to density changes. The air over the sea and land is described as baroclinic. The cooler air from the sea flows inland in the form of a gravity current. When the mean wind on the land opposes the direction of the gravity current, frontogenesis occurs. The cooler, high density air in the gravity current makes contact with the warmer air opposing it, forcing the fluid in an upward direction. This sharp direction change can lead to a turbulent interface between the two layers on the upper edge of the front, with Kelvin - Helmholtz billows being one of the features of the sea breeze front, as shown in figure 6.1.

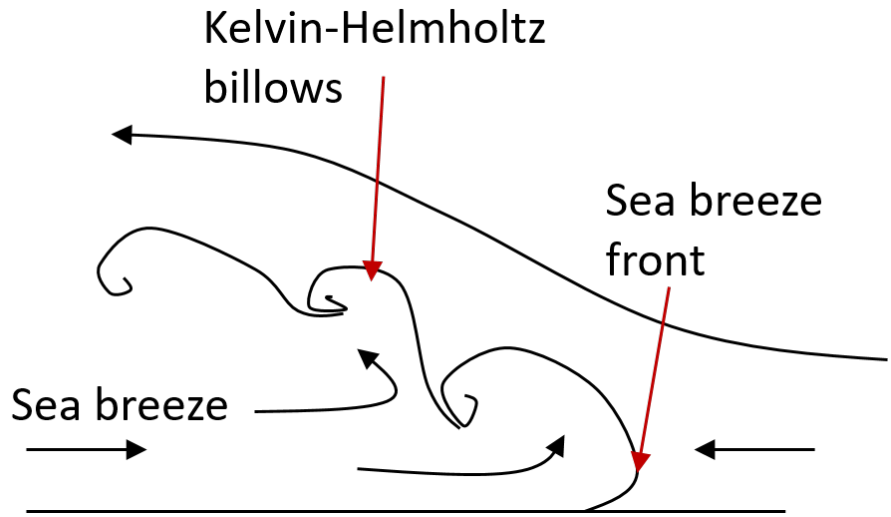

(a)

Figure 6.1: *Sea breeze schematic, reproduced from (Simpson, 1994, fig. 3.1)*

Another feature that can occur in a sea breeze front are internal bores (Simpson, 1987, p. 35). These can occur when a surface feature, such as friction, causes the front of the gravity current to detach itself from the rest of the current. The internal bore propagates with the front, reaching a distance of 10 km ahead of the front, as described in Simpson (1987).

Gravity currents can be altered by the addition of surface obstacles. Laboratory experiments described in Simpson (1987) show the behaviour of a gravity current upon contact with a solid barrier. When the barrier is less that twice the height of the gravity current, upon contact with the barrier, the gravity current increases in height. This sudden increase leads to an instability which subsequently collapses the front resulting in a hydraulic jump which propagates along the top of the

current against the mean flow. There is also a portion of fluid which flows over and past the obstacle. When a solid barrier is replaced with a porous obstacle, as shown in (Simpson, 1987, fig. 11.20), the current increases in height, however then decreases again as the flow continues to flow through the obstacle. There is also a hydraulic jump propagating upstream however weaker than that observed in the solid obstacle case. It is unknown whether a wind turbine has a similar affect on a sea breeze.

The idea of a gravity current being impacted by surface obstacles raises the question as to the impact from wind farms. In the UK, offshore wind farms are expected to be of great importance to meet renewable energy targets (Corbetta *et al.*, 2015), and it is of interest to see how wind farms could impact the sea breeze. Work in this area has been conduction by Steele *et al.* (2013), who looked at the effect of changes in velocity associated with sea breezes in the UK. Sea breezes with different gradient wind directions were used. These were described as a pure sea breeze, where by the opposing gradient wind is perpendicular to the coast, corkscrew where the the gradient wind is parallel to the coast with the coast on the left and backdoor where the wind is parallel with the coast on the right. It was found that the pure sea breeze exhibited the weaker maximim velocity in the sea breeze, 27% slower than the corkscrew case. Although highlighting the issue of sea breezes and wind farms, Steele *et al.* (2013) focused on the impact of the sea breeze on the wind farm. The converse has not been investigated, and this chapter aims to answer whether wind farms could impact a sea breeze gravity current.

6.2 Configuration of the Weather and Research Forecast Model

To investigate the impact from wind farms on a sea breeze, simulations have been carried out in WRF. A general description of WRF can be found in chapter 3, with the following being the set up used in these simulations.

Idealised WRF has been used, with just the 2-dimensional configuration of the model used. This is done to maximise the effect from the wind farm. The periodic boundary conditions in the lateral direction prevent any flow around the sides of

	Albedo	Surface moisture ($m^3\,m^{-3}$)	Surface roughness (m)
Land	0.16	0	0.2
Sea	0.08	0	0.001

Table 6.1: *Land and sea surface properties to simulate a sea breeze.*

the turbines. There is also a computational advantage of running 2-dimensional simulations as higher resolution can be used. It is of interest to look at the greatest potential impact from a wind farm, and the 2-dimensional simulations ensure that the propagating front is perpendicular to the simulated shore line.

The simulations are set up with a 400 km domain width with spacing of $\mathrm{d}\,x = 1$ km. The domain top is set at 10 km with 72 model levels. The lowest level at the beginning of the simulations occurs at approximately 21 m above the surface, with 28 model levels in the lowest 500 m of the domain. The exact height of each model level changes with time as it is calculated from the geopotential height. Within the centre of the domain there is a simulated land patch of 120 km width. There are therefore two sea breeze fronts in the following simulations, both of which propagate to the centre of the domain. For the purpose of analysis, only the left hand side of each simulation will be studied. Due to the opposing sea breeze fronts, there is the possibility of the two fronts converging. The chosen land patch width prevents this from having an impact on the sea breeze evolution and decay.

Differentiation between the simulated land and sea is due to the prescribed land use characteristics in WRF. Custom land use characteristics have been used for both the sea and land. Table 6.1 describes the differences in the land and sea surface properties. The land is simulated with an increase in surface roughness and surface albedo. Notice that in both surface characteristics there is no surface moisture. This is to limit the effect to dynamical differences and not due to the microphysics or thermodynamics which would occur if water vapour were present. The ensure this persists throughout the simulations, the model is initialised with a dry sounding resulting in a dry atmosphere for the duration of all the simulations. This maximises the thermal heating and inhibits latent heat flux at the surface and hence the maximises the sea breeze.

The model is set up with schemes suitable for the investigation of wind farm dynamics. Long wave radiation is provided by the rapid and radiative transfer model RRTM (Miawer *et al.*, 1997). The Mellor –Yamada –Nakanishi –Niino (MYNN) model is used for the planetary boundary physics scheme. This scheme is suitable for use in wind farm parametrisation as it includes buoyancy and pressure covariances in parametrising the mixing length scale. This, when coupled with the 1.5 TKE closure scheme, allows for an enhancement of the wind farm parametrisation, as described in Fitch *et al.* (2012). A 5 layer surface scheme is used, whereby there are 5 soil layers over the land. This is used to provide an element of cooling in the land surface temperature, enabling the development and propagation of the night time land breeze. This phenomenon will be discussed later in the chapter. A 5 km damping laying is enforced at the top of the domain, with a damping coefficient of 0.003. This prevents the reflection of waves that could be generated by the sea breeze front.

The individual wind turbines are parametrised as in Fitch *et al.* (2012), the same scheme described in section 3.3. Each turbine has a hub height of 100 m and a rotor radius equal to 50 m. Steele *et al.* (2013) found that the maximum velocity in an idealised WRF sea breeze is $\approx 4\,\mathrm{m\,s^{-1}}$, which is similar to the cut in speed of most operational wind turbines. To ensure that the wind farms are turned on in these simulations, the cut in speed is set to $1\,\mathrm{m\,s^{-1}}$ with a cut out speed of $25\,\mathrm{m\,s^{-1}}$. The thrust coefficient is set to 0.7 for all wind speeds, with the power generated by the turbines increasing with velocity. Each turbine has a maximum nominal power of 3 MW which is reached at a velocity of $12\,\mathrm{m\,s^{-1}}$.

To directly look at the impact from a wind farm on the sea breeze front, wind farms are positioned on the land/sea boundary. Positioning the wind farm further away from this boundary allows the wind farm wake to disipate before being in contact with the sea breeze. Carrying out simulations with the wind farm on the land/ sea boundary means that the boundary layer on the downstream edge of the wind farm is continually evolving. This may result in changes to the sea breeze front directly from the wind farm, limiting the effect of the upstream boundary layer conditions. Preliminary simulations with a wind farm located 10 km from the land/sea boundary showed that the wind farm wake decreased significantly by the time it reached the land/sea boundary. Furthermore, although large wind farms are being constructed 100 km from the shore, as in the case of the Dogger

Simulation name	WF1	WF2	WF3
Number of wind turbines	10	100	1000
Turbine density	$0.000001\,\mathrm{m}^{-2}$	$0.00001\,\mathrm{m}^{-2}$	$0.0001\,\mathrm{m}^{-2}$
Hub height	100 m	100 m	100 m
Rotor diameter	100 m	100 m	100 m

Table 6.2: *Wind turbine densities used in the wind farm simulations.*

Bank wind farms, some operational wind farms are located much closer to the coast, such as the Teeside wind farm which is only 1.5 km from the shore.

The simulations are initialised with an idealised input sounding. This is a stable atmospheric sounding with an air surface temperature of 300.5 K. As explained previously, there is no water vapour in the input sounding. Both the land and sea are initialised with a surface temperature of 288.5 K, and the land has a lower soil temperature of 280 K. The primary simulations used in this analysis are run after a 96 hour spin up simulation. This simulation begins at 06:00 and is run to achieve a steadily evolving sea breeze, where the impact from any imbalances in the initial conditions are minimised. The spin up simulation has gone through four cycles of a sea breeze followed by a land breeze with both fronts reaching a steady state in their cycles from one day to the next. The primary simulations are then run as a continuation of the spin up simulation.

6.3 The effect of changing the wind turbine density on a sea breeze front

The first simulation used in this study is the control case (CTRL), with no wind farm present. Additional simulations include a wind farm. All simulations have the same wind farm area, from 0 km to 10 km on the westward shore line. The 2-dimensional set up with periodic boundary conditions means that the exact area is 10 km × 1 km wide giving a total wind farm area of $10\,\mathrm{km}^2$. Although the simulations are 2-dimensional, the size of the wind farm will be given in square metres.

Three wind farm simulations will be used, with varying wind turbine densities. The set up of the wind farm simulations is given in table 6.2.

Of these simulations, only WF1 is a realistic set up. Simulations WF2 and WF3 are used to look at extreme scenarios. All four simulations are continued from the spin up simulation and run for 24 hours. This enables a full sea breeze cycle to be investigated along with the evolution of the land breeze.

6.3.1 Differences in the dynamics of the sea breeze gravity current

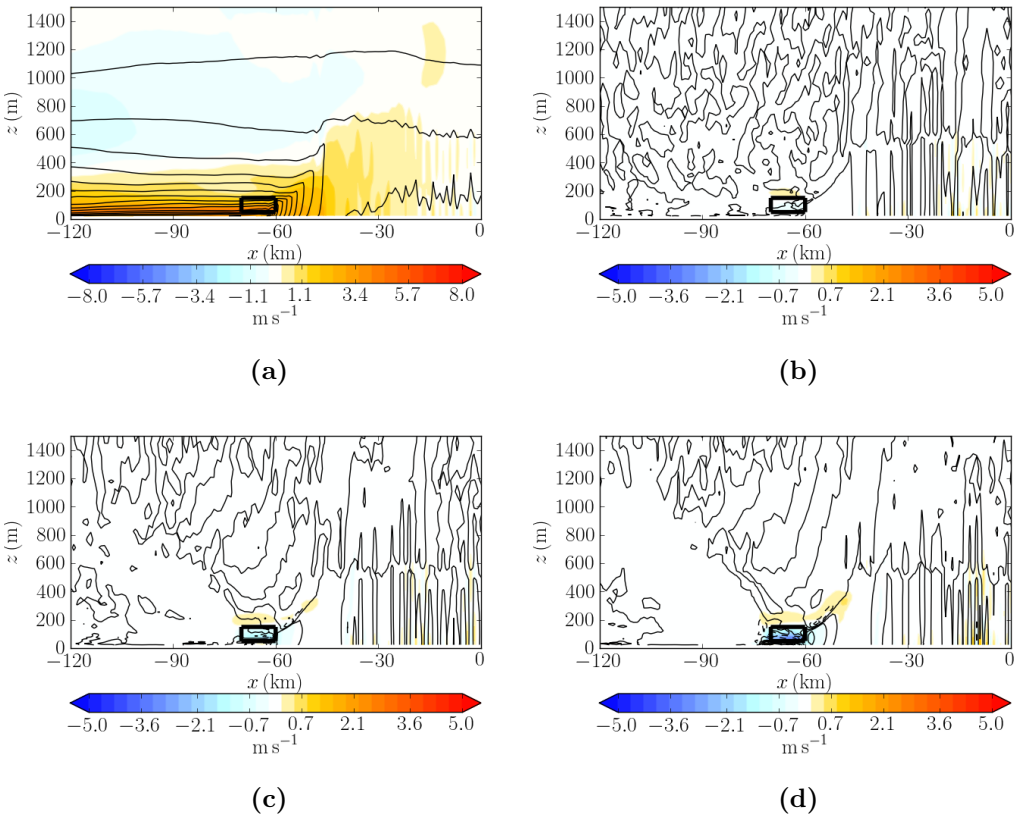

Figure 6.2: *Contour plots at 11:30 simulation time. Figure (a) shows the horizontal velocity contours in the CTRL simulations. Here, the solid black contours represent the potential temperature, at* 1 K *intervals. Figures (b), (c) and (d) show the difference between the WF1, WF2 and WF3 simulations and the CTRL simulation. Shown also are the potential temperature differences, with the solid black contours showing a positive difference and dashed contours denoting a negative difference. For each case, the contours are separated by* 0.25 K. *The wind farm rotor area is shown by the black box. In plot (a) the wind farm rotor area is given as reference; no wind farm is present in this simulation.*

The simulations begin at 06:00. At this time the atmosphere is still, as the previous days sea breeze has decayed as has the night time land breeze. At the beginning of the simulations, the sea temperature is $\theta = 288.5\,\mathrm{K}$ and the land temperature is $\theta = 278\,\mathrm{K}$. Surface heating then starts, and at 09:00 the land temperature is greater than the sea temperature. The surface temperature continues to rise until 17:00 when it has a maximal value of $\theta = 305\,\mathrm{K}$ in the centre of the domain. The surface temperature then decreases again. At 19:00 the temperature of the coast is less than the sea, and then at 20:30 the temperature at the centre of the domain is also less than the sea temperature.

At 11:30, the sea breeze front has developed which can be seen from the area of increased velocity in 6.2(a). Over the land there is an increase in temperature compared to the sea, which is driving the propagation of the front. The black temperature contour lines include a large amount of noise from the convection. This is prevalent in all simulations and will be discussed later on in the chapter. At this time in the simulations the effect of the wind farms can be observed. Figure 6.2(b) shows an area of decreased velocity within the wind farm area, with an increase in velocity above the wind farm. The turbine induced mixing creates a homogeneous patch of air within the wind farm. As can be seen in 6.2(a), there is a greater velocity near the bottom of the wind farm. The mixing within the wind farm area results in a decrease in the lower part of the rotor area and an increase in the upper part. The wind farm wake in 6.2(b) does not extend past the wind farm, and at this time there is little to no affect from the wind farm on the velocity contours.

An increase in wind turbines within the wind farm increases the difference in velocity, both within the wind farm area and in the surrounding part of the atmosphere. Figures 6.2(c) and (d) show an increase in the velocity deficit within the wind farm area. Figure 6.2(d) shows a greater velocity deficit in WF3 although at this time in the simulation, the extent of the wind farm wake is the same as in WF2. Furthermore, it can be seen that there is an area of increased temperature. The mixing within the wind farm wake mixes the warmer air above and to the east of the wake with the cooler air of the front. This increase is greatest in WF3 (fig. 6.2(d)). In figure 6.2(a), (b) and (c) there are fluctuations in velocity over the land. These changes in velocity occur ahead of the sea breeze front and are grid scale noise brought about from the grid scale convection that occurs in these simulations. This affect was observed in preliminary simulations and measures

were undertaken to reduce their effect. It was found that increasing the lowest model level reduced the noise in the convection. This was implemented in these simulations, however with the rotor area ranging from 50 m to 150 m there was a limit to how high the lowest model level could be. It was also noticed that decreasing the resolution to $\mathrm{d}x = 2\,\mathrm{km}$ decreased the noise. Doing this would reduce the noticeable impact from the wind farms on the sea breeze front. Going any coarser than the 1 km used in these simulations would lead to inaccurate velocity deficits in the near wind farm wake.

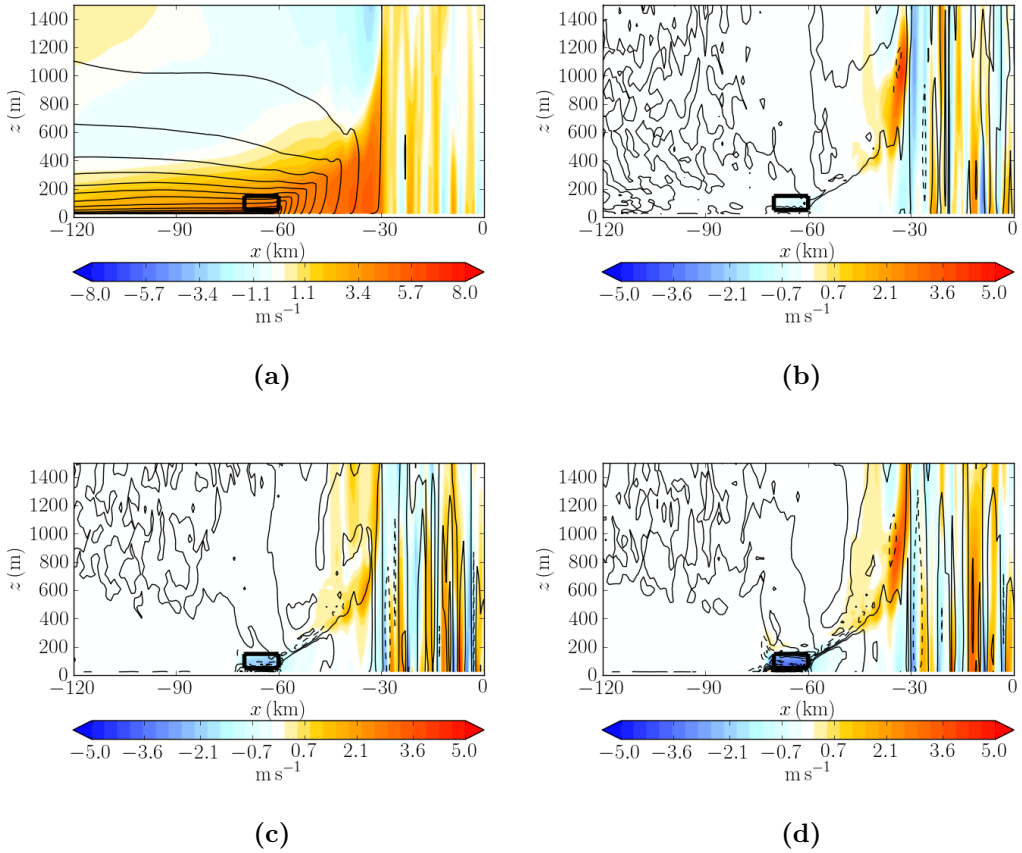

Figure 6.3: *As in figure 6.2 but at 14:30 simulation time.*

As the sea breeze propagates further inland, the velocity deficit caused by the wind farm increases. Figures 6.3 (b), (c), and (d) show a more negative velocity difference around the wind farm area than the respective simulations in figure 6.2. This increased velocity deficit is a direct result of a strengthening of the sea breeze, bringing with it increased velocity within the wind farm area.

The average hub height velocities within the wind farm area in figure 6.4 show an

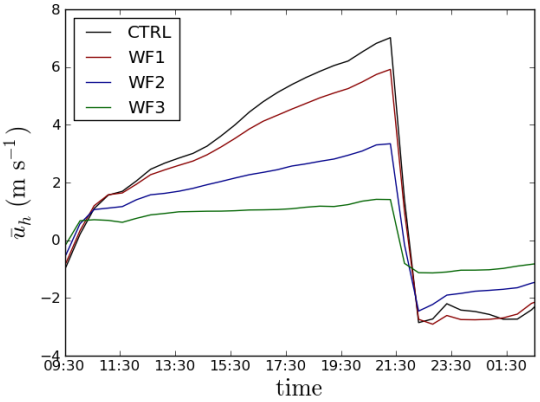

Figure 6.4: *The average hub height velocity within the wind farm for all simulations, or the area that the wind farm would occupy in the case of the CTRL simulations.*

increase with time. The CTRL simulation shows how with no wind farm present there is an increasing velocity for the duration of the surface heating. With the wind farms present there is an expected velocity decrease. WF1 shows little deficit until 12:00, at which point the wind farm drag is sufficient to decrease the average velocity at hub height. The hub height velocity of WF1 continues to increase up to 21:00 at which point the surface heating stops. WF2 also shows increasing hub height velocity throughout the time of surface heating, the difference being a greater velocity deficit compared to WF1. The rate of increase in WF2 is greatly reduced compared to WF1, and WF3 shows a significantly reduced rate of change in the hub height velocity. It is not surprising to see a greater velocity deficit in WF3, after all, the first 1 km of the WF3 is equivalent to 10 times the drag from the WF1 wind farm.

As the simulations progress, the deficit around the wind farm increases, with a greater deficit in WF3, as shown in figure 6.5(d). Although the deficit is greatest in WF3, the wake from this wind farm extends no further than WF1 or WF2. Figure 6.6 shows that at 10 km downstream of the wind farm at 16:00, there is very little velocity deficit (figure 6.6 (a)) and the TKE is the same in all simulations, shown in figure 6.6(b). At this distance, the velocity deficits, as calculated by equation 2.9, are 3.5% in WF1, 5.9% in WF2 and 7% in WF3. Compared to the velocity deficits in section 4.3.1, these are smaller than expected at this distance, attributed to the convective boundary layer which is formed over the land. The effects of this convective boundary layer can be seen in figure 6.6(b) where the

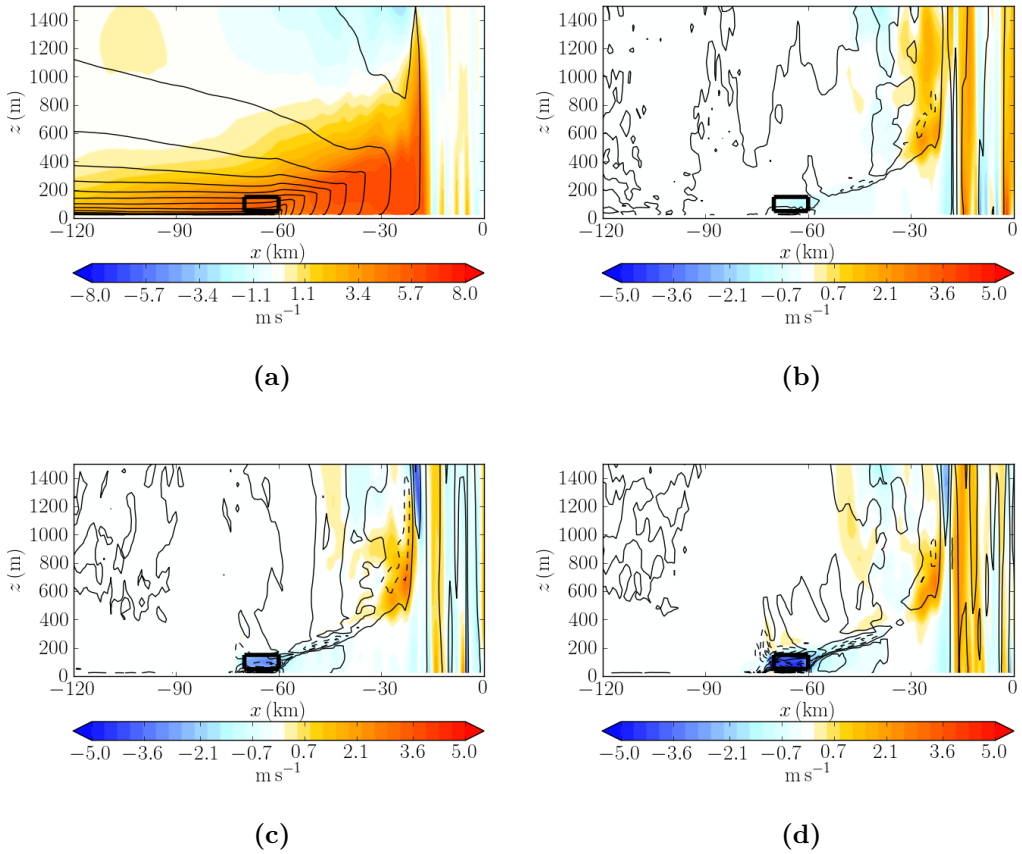

Figure 6.5: *As in figure 6.2 but at 16:00 simulation time.*

TKE profiles are the same in each simulations. This shows that at this distance downstream of the wind farm, the TKE caused by the surface heating is the dominant driver in TKE, and not the addition of TKE from the wind farms. This feature is also seen 5 km downstream of the wind farms at 16:00. Figure 6.7 (a) shows the wind farm wake, and as expected a greater velocity deficit in WF3, but then 6.7 (b) shows similar levels of TKE. Even though the velocity deficit is greater in WF3, by as close as 10 km downstream, the wake has all but been eliminated by the turbulent boundary layer situation of the sea breeze.

At 17:30 simulation time, the sea breeze has reached its maximum extent inland. Recall that there are two opposing sea breeze fronts in these simulations and at this time the two fronts almost collide. The sea breeze front has reached a height of 1400 m, as shown in figure 6.8. In addition to the velocity deficits, there are changes to the potential temperature around the wind farms. At 5 km downstream of the wind farm, there is a -0.32 K difference in θ in the WF3

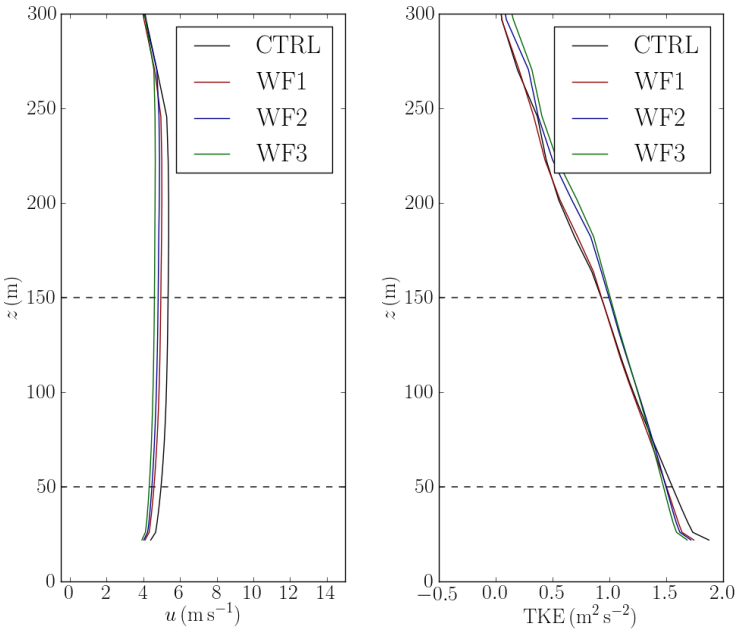

(a) **(b)**

Figure 6.6: *Vertical profiles of u (a) and TKE (b) at 16:00 simulation time for each simulations at a distance of* 10 km *downstream of the wind farm.*

simulations. This is compared to differences of −0.13 K and −0.26 K in WF1 and WF2 respectively. In contrast however, at time 16:00, there are θ differences of 0.08 K, 0.39 K and 0.52 K in the WF1, WF2 and WF3 simulations.

The change in θ imparted on the flow over this period is due to the change in stability over the wind farm area. At 16:00, the wind farm is in the well mixed layer of the sea breeze front. The mixing associated with the wind farm advects warmer air from above into the front, increasing the temperature. This can be seen by the area of increased potential temperature in figure 6.5(d). Conversely, at 17:50, the air below the wind farm begins to cool and hence a stable boundary layer is formed. The wind farm mixing now acts by mixing cooler air from below which decreases the potential temperature perturbation in the wind farm area. Figure 6.8(d) shows that the area of increased potential temperature in the wind farm wake has propagated further inland, displaced by the region of decreased temperature.

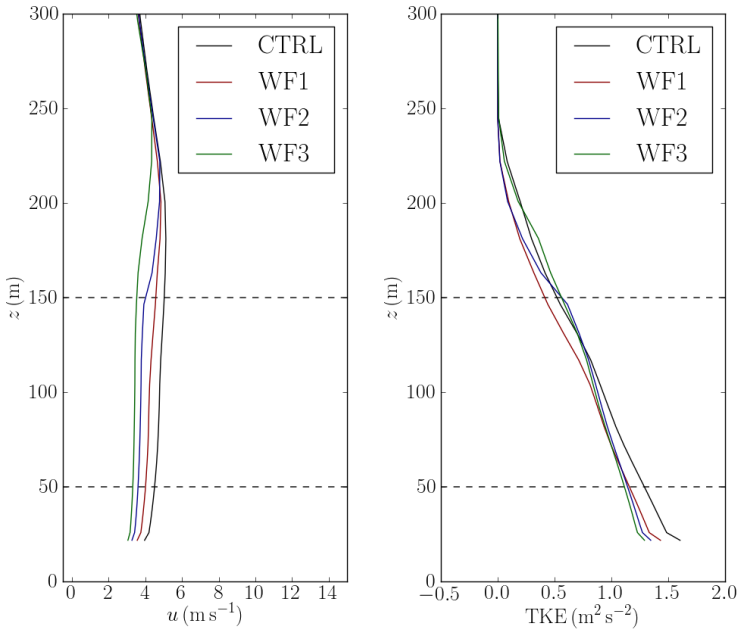

(a) **(b)**

Figure 6.7: *As described in figure 6.6 except at a distance of* 5 km *downstream of the wind farms.*

6.3.2 Propagation of the sea breeze gravity current

Thus far, it has been shown that the wind farms in these simulations make a difference to the boundary layer within the vicinity of the wind farm. It is of interest to identify whether these wind farms impact the propagation of the sea breeze front. To do this, the position of the front and the associated velocity are calculated. This is done by looking at the velocity at hub height through the domain. The front of the sea breeze front is classified at the point where, starting from the most westerly position and moving eastward and the velocity of the sea breeze is at its maximum. This latter condition accounts for the maximum velocity being ahead of the sea breeze front caused by the high levels of convection in these simulations. The position and velocity in all four simulations are then plotted, and can be seen in figure 6.9.

The inclusion of the wind farms, regardless of the wind turbine density, makes little difference to the position of the sea breeze front, as can be seen in figure

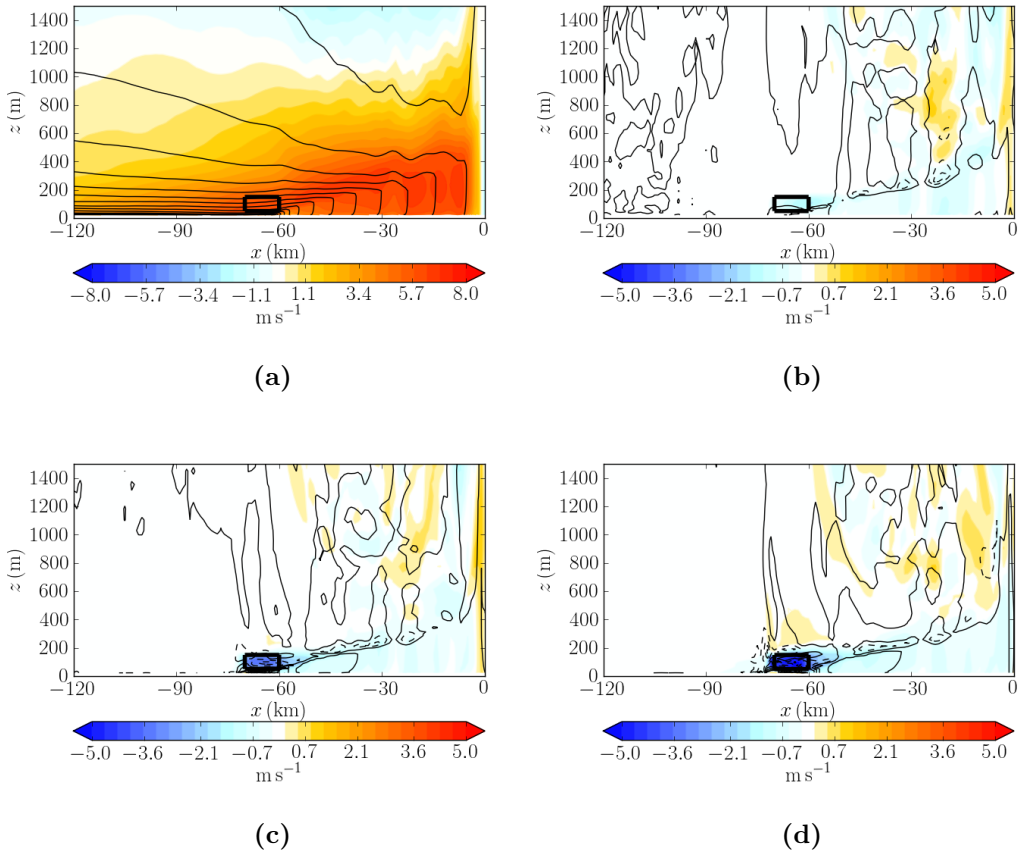

Figure 6.8: *As in figure 6.2 however at 17:30 simulation time.*

6.9(a). At 11:30, the head of the front is more westerly in the wind farm simulations compared to the CTRL simulations. This is the time when the sea breeze starts to propagate over the land, starting from the coast, as shown in figure 6.2. This means that the wind farm wake is having a direct impact on the sea breeze front. This effect is short lived, and as the front propagates further inland, the effect from the wind farm wake is diminished as shown between 12:00 and 14:00 in figure 6.9(a). The effect from the wind farm wake is also visible in figure 6.9(b) at 11:30. Here, there is a decrease in the velocity, with the greatest decrease in WF3. As with figure 6.9(a) the impact is short lived and cannot be seen in the next time frame at 12:00.

Figure 6.9 shows how the sea breeze propagates inland and reaches its maximum distance inland around 17:30. During its propagation inland, there are small changes in both the position and velocity. Between 13:00 and 14:00 there is an increase in the velocity for the wind farm simulations and then a decrease. This

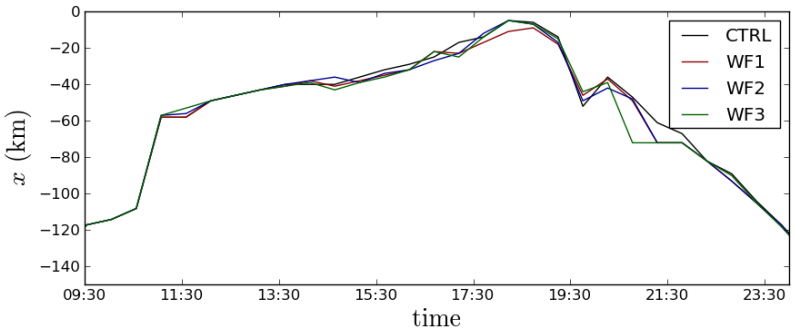

(a)

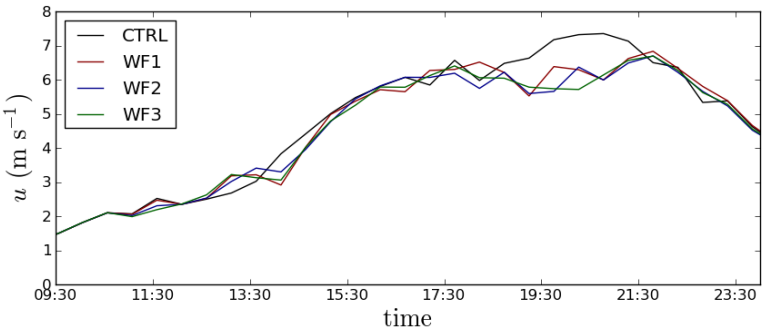

(b)

Figure 6.9: *Plots showing the position of the sea breeze front (a) and the velocity at the front (b). When a land breeze is present, figure (b) shows the velocity to the west of the front and hence is always positive. In figure (a) the position is given in terms of the position on the x-axis, where the centre of the land is at* 0 km *and the edge of the land is at* −60 km*.*

is caused by the interaction of the sea breeze front, convection ahead of the front and the wind farm wake. At 13:00, the velocity at hub height at the head of the sea breeze front is categorised by two peaks. One peak is at −60 km on the coast boundary and the other is approximately 10 km ahead. Both are of the same magnitude with a decrease in velocity between. The inclusion of the wind farms decreases the first peak on the coast as a result of the wind farm wake. This in turn increases the velocity between the two peaks meaning that at the head of the front, the same energy translates into an increased velocity at the front. The front of the sea breeze is on the edge of the wind farm wake, with turbine mixing increasing the velocity. This increase is however small and not sufficient to change the propagation of the front. At 14:00, the sea breeze front has propagated beyond the wind farm wake. The convection ahead of the sea breeze front collides

with the front, but only in the wind farm cases. This explains why there is not consistent change in the velocity decrease at 14:00 between the three wind farm simulations.

As the sea breeze propagates further inland, the velocity at the front shows a more scattered behaviour. At this point, the front is beyond the reach of the wind farm wake and any changes are a result of the changes in convection between the simulations. Between 19:00 and 21:30 there are significant decreases in the velocity of the front. This is linked with the formation of the land breeze and will be discussed in the next section.

6.3.3 Wind farm impact on the land breeze gravity current

At 17:30 simulation, there is no more surface heating and hence the sea breeze begins to decay. At the head of the front, a bore develops due to the sudden decreases in surface temperature at the head of the front. This bore is then a cooler patch of air that propagates from east to west in these simulations, i.e. towards the sea. This is due to the high pressure within the bore and lower pressure towards the coast.

At 19:00, the bore has propagated to -30 km as shown in figure 6.10(a). It can be seen that there is a negative velocity, showing that it is propagating towards the sea and the decrease in temperature reaches 800 m into the remains of the sea breeze current. In figures 6.10(b), (c) and (d) there are consistent areas of velocity deficit associated with this bore. The areas around the wind farm are to be expected, as there is still a positive velocity through the wind farm and hence they are still turned on in the simulations. East of the wind farm is the associated wind farm wake, which is once again more prevalent in WF3 simulations. At -30 km, the velocity deficit at the position of the bore means that the strength of the bore increases with the wind farms in operation. The magnitude of this difference is the same in all simulations, showing that the density of the wind turbines is not the critical factor. The reason for this deficit is the transition from a convective boundary layer to a stable boundary layer meaning there is no more surface heating at this point in the simulations. The wind farm wake does not decay at the same rate as earlier in the simulations and has a greater impact

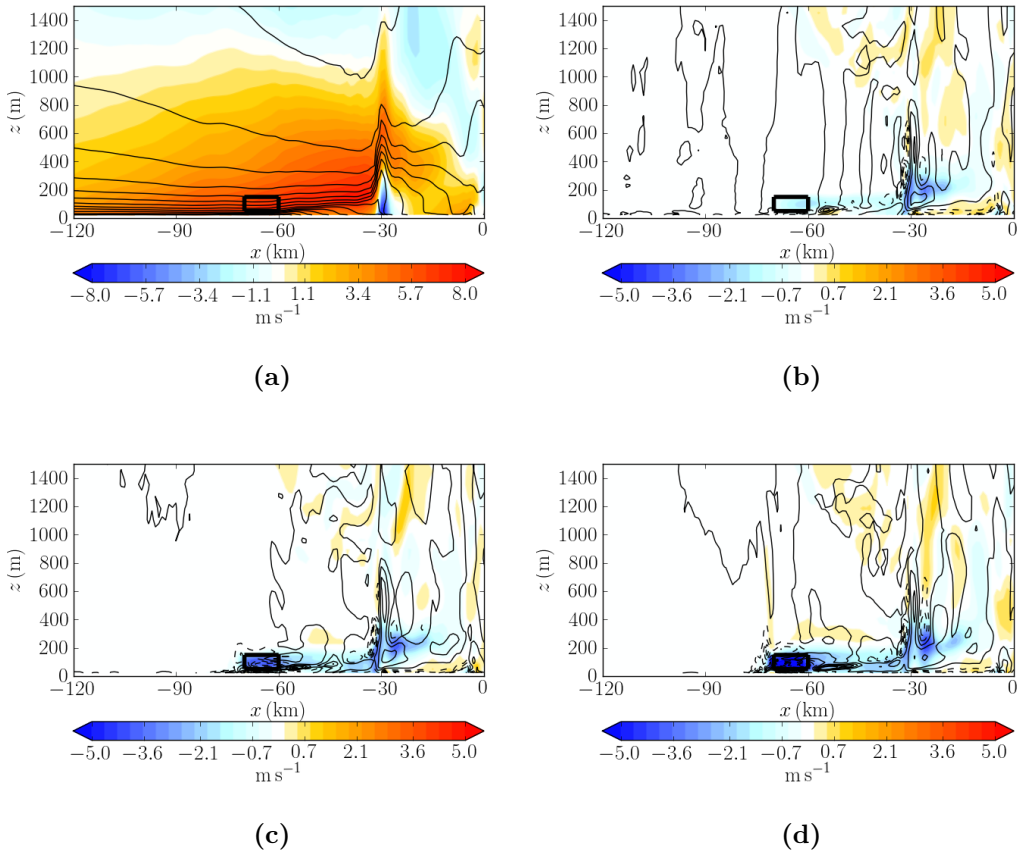

Figure 6.10: *As described in figure 6.2 however at 19:00 simulation time.*

on the boundary layer. The wind farm wake has an increased temperature as the warmer air aloft is mixed into the wake, as shown by the black contours in figures 6.10(b), (c) and (d). The flow between the wind farm and the bore is reduced in the wind farm simulations, also shown in figure 6.10(b), (c) and (d). Figure 6.9(b) at 19:00 shows the positive velocity to the west of the land breeze. The decrease in velocity in figure 6.9(b) at 19:00 shows the impact of the wind farm wake on the land breeze front, where the front is propagating into a weaker opposing current. The pressure changes which are driving this bore are the same in all simulations, however in the wind farm cases there is a velocity reduction in the flow that the bore is propagating into. This increases the velocity within the bore in all wind farm simulations, as shown by the negative difference at $-30\,\mathrm{km}$ in figures 6.10(b), (c) and (d). It should be noted that the velocity is negative and hence the negative difference implies a greater negative velocity in the wind farm simulations.

Within the wind farm area in figure 6.10, decreases in θ can be observed to the west side of the wind farm, i.e. upwind of the wind farm. This is a result of the vertical transport that occurs at the front of the wind farm as described in chapter 4. The vertical transport in these simulations raises the cooler air over the sea surface to the warmer air in front of the wind farms, hence a cooling affect. This effect is most clear now as the velocity within the wind farm has also increased, as shown in figure 6.4, and a greater hub height velocity increases the magnitude of the vertical transport ahead of the wind farm.

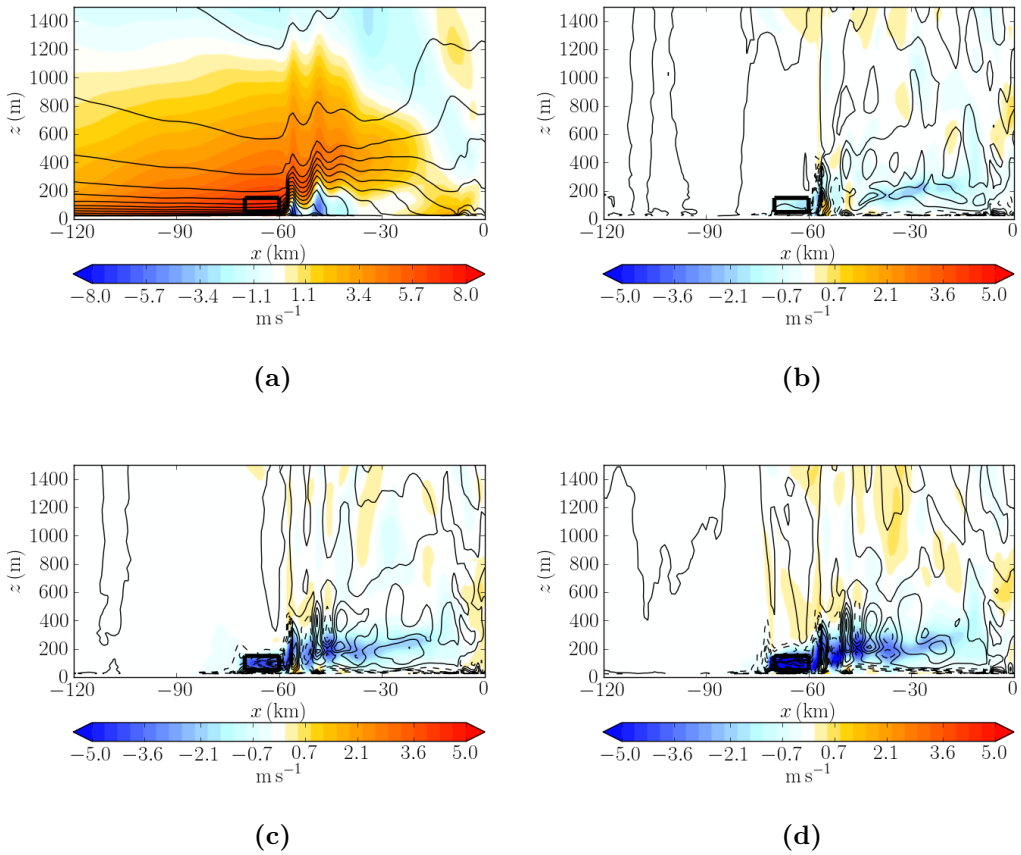

Figure 6.11: *As described in figure 6.2 however at 20:00 simulation time.*

As the bore propagates towards the coast, a second bore forms. This happens ahead of the existing bore at the coast boundary. This can be seen in figure 6.11(a) by the two areas of negative velocity, both with an increase in potential temperature. At this point the bore develops into a recognisable land breeze gravity current.

The wind farm impact is at its greatest at this point in the sea breeze cycle.

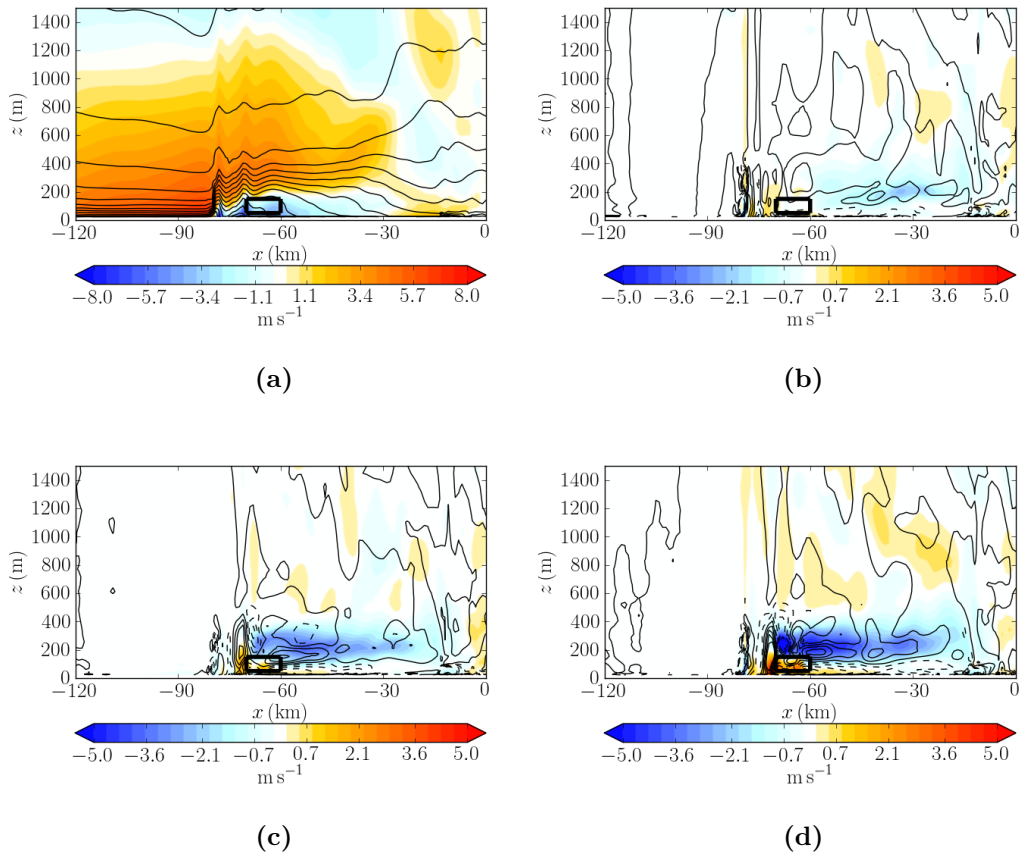

Figure 6.12: *As described in figure 6.2 however at 21:00 simulation time.*

Figures 6.11(b), (c) and (d) show high velocity deficits between $1.1\,\mathrm{m\,s^{-1}}$ and $5.4\,\mathrm{m\,s^{-1}}$ at hub height in the centre of the wind farm. During this time, the flow within the wind farm is travelling west to east, with the average hub height velocity in CTRL being $7.2\,\mathrm{m\,s^{-1}}$. With the flow having this orientation in the wind farm, the wake instantly collides with the head of the land breeze and the bore to the east induces changes to the velocity contours. There is still the increased velocity within the bore and hence the land breeze front at 20:00 as shown in figures 6.11(b), (c) and (d). In these figures, potential temperature changes can be observed east of the wind farms. This is showing that the potential temperature in the bore is reduced in the wind farm simulations. This is a result of the wake mixing the cool air in the bore with the surrounding warmer air. The largest potential temperature differences can be seen in figure 6.11(d) for the WF3 simulation which has the largest velocity deficits and hence the most effective wind farm wake.

Further propagation of the land breeze front brings it through the wind farm. Figure 6.12(a) shows the land breeze at 21:00 having propagated through the wind farm area in the CTRL simulation. Two troughs in temperature within the front can still be seen, one at the westward edge of the would be wind farm and the second further west. The maximum height of the front reaches to 200 m at the land sea boundary. There is a sharp increase in temperature between the land breeze front and the ambient air, however the temperature changes within the wind farm area is of the order of 1 K cooler. The addition of a wind farm to this flow makes multiple changes to the propagation of the land breeze front, which are dependent on the wind turbine density. Figure 6.12(b) shows an increase in velocity at the westward edge of the wind farm in WF1. Due to the orientation of the mean flow through the wind farm, this increase is a velocity deficit within the wind farm wake. At this time, the land breeze is 200 m high as it passes through the wind farm. Above the front there is a sharp temperature gradient, partially constricting the advection of air into the front. The height of the front is smaller than the sea breeze front, which reached a maximum height of 1400 m and was well mixed. The shallower land breeze front will mean that any perturbations from the wind farm will be stronger when the land breeze propagates through the wind farm. East of the wind farm there are further deficits which is the decaying wind farm wake from the west to east flow through the wind farm. There are further changes to the potential temperature profile of the westerly edge of the wind farm. The mixing effects of the wind farm wake have a greater vertical extent than the height of the wind farm, as described in chapter 4. Figure 6.12(a) shows that the top of the land breeze front is of the same height as the wind farm on the west edge, meaning that the wind farm wake will increase mixing at the upper edge of the land breeze front. This homogenisation of the flow mixes the cooler air in the front with the warmer surrounding air, thereby increasing the temperature of the air at the top of the front. This effect can be seen in the θ contours in figure 6.12(a) west of the wind farm.

The increase in turbine density increases this effect. Figures 6.11(b) and (c) show greater areas of positive velocity difference on the west edge of the wind farm. The increase in temperature also becomes more defined as the turbine density increases. The changes in turbine density change the behaviour of the flow upon contact with the wind farm. The increased density of the wind farms in WF2 and WF3 act as a greater obstacle for the flow. This increases the height of the flow

up to 300 m in WF3. The drag effect of the wind farms not only increases the height of the front but also stalls it compared to the CTRL simulation. In WF3, this stalling occurs between 20:00 and 20:30, and at 21:00 the flow propagates through the wind farm. The wind farms in these simulations show the same characteristics as a porous obstacle on a gravity current, as shown in (Simpson, 1987, p. 158). Simpson (1987) also showed that a porous obstacle can produce a hydraulic jump upstream of the obstacle, however this is not observed in the simulations. It is not clear whether this is a result of the enhanced mixing from the wind farms compared to a static obstacle, or whether the resolution in these simulations is too course to capture such an occurrence.

The increase in land breeze height over the wind farm in WF2 and WF3 leads to an increase in temperature above the wind farm. This is caused by the warmer air aloft being mixed with the cooler air in the front, and can be seen in the dotted contours in figures 6.12(c) and (d). The dotted contours above and to the west of the wind farm are a result of the two temperature peaks of the front, as seen in the CTRL simulation, being shifted as a result of the wind farm.

The effects observed at 21:00 are carried with the front as time progresses. The velocity contours at 22:30 are shown in figure 6.13. At this time, the head of the front has propagated 50 km downstream of the wind farm, a distance at which the wind farm wake does not reach, not even in WF3. Between -90 km and -60 km the land breeze gravity current is in a relatively steady state, that is the height of the current is constant and there are only small changes in potential temperature. The top of the current remains at 200 m, with the rate of temperature change decreasing further to the east.

At 22:30, WF1 shows changes to the head of the front, as shown at -110 km in figure 6.13(b). This is the result of the flow through the wind farm, where by the velocity deficit reduces the propagation of the land breeze. The velocity deficit in the wake in WF1 is very small, as at this time the flow through the wind farm is $\approx 1\,\mathrm{m\,s^{-1}}$. The increase in turbine density increases the perturbations at the head of the front, and also increases the visibility of the wind farm wake. Even though the velocity within the wind farm is similar at this time in all simulations, the combined effect of the turbines in WF3 can be observed. Of greatest interest in figure 6.13 is that in figure (b), there is a velocity decrease east of the wind farm with an associated temperature increase. This is a result of the drag from the wind farm, which raises the height of the land breeze upstream of the wind

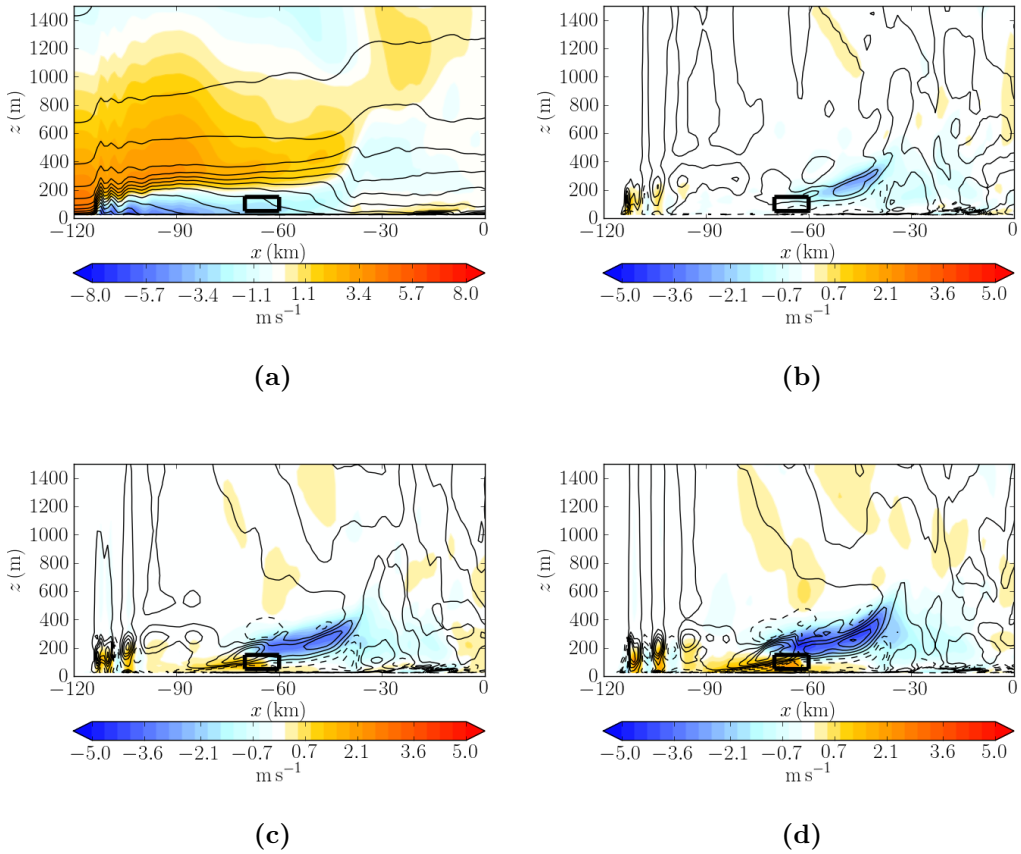

Figure 6.13: *As described in figure 6.2 however at 22:30 simulation time.*

farm, i.e to the east. This is occurring 20 km upstream and occurs even though the downstream impacts of the wind farm are small. As expected, WF2 and WF3 show a more prominent increase in the gravity current height at this point, as shown in figures 6.13(c) and (d).

6.4 Discussion and summary

The previous sections have looked at the impact of a wind farm in a sea breeze cycle. This has included the sea breeze and land breeze fronts. This section aims to bring the previous ideas together and discuss how wind farms could impact a sea breeze.

As the sea breeze evolves, there is an increase in velocity through the wind farm. At 11:30, the velocity within the wind farm is sufficient to produce a velocity

deficit in all wind farm simulations. At this point the sea breeze front is near the coast and hence small changes in the velocity at the front are observed. As the front propagates inland, the surface heating which drives the front also increases. This increase in energy from the solar heat is sufficient to mix the air with the front, negating the impact from the wind farms. This is true in all wind farm simulations, even in WF3 which has the greatest velocity deficit within the wind farm.

By the time the velocity in the wind farm is sufficient to produce an evolved wind farm wake, the front of the sea breeze has propagated inland, past the extent of the wind farm wake. This results in a standard wind farm wake within a convective boundary layer and is not dependent on there being a gravity current.

Changes in the position of the front are difficult to observe. This is due to the high level of grid scale convection which occurs ahead of the front. Efforts were made in the set up of these simulations to minimise this impact but their occurrence was unavoidable. Although a challenging feature in the simulations, the convection does show that the impacts from a wind farm are likely to be limited in a more realistic sea breeze set up.

The land breeze part of the cycle is however affected more by the wind farm. As the land breeze approaches the wind farm, the higher density wind farms cause an increase in the height of the front. There is a stalling of the front as it flows through the wind farm, causing displacement at the head of the front. The height of the land breeze is less than the sea breeze front, with strong temperature gradients occurring above the land breeze front. The shallower land breeze will contribute to the increased effects from the wind farm compared to the sea breeze. These effects propagate within the land breeze front and can be observed at 50 km downstream. There are also increases in the height of the gravity current front in WF1, although they occur later on in the cycle of the land breeze. This is more attributed to the drag from the turbines rather than the increased TKE associated with them. The direct interaction between the wind farm and the land breeze is the reason for the greater wind farm impacts compared to the sea breeze.

These simulations have been set up to enhance the impact of the wind farm in WF1. This was achieved by positioning the wind farm on the coast, where the wake would have the greatest impact without the wind farms being positioned on

the land. Two dimensional simulations were also used, as the periodic boundary conditions result in an infinitely wide wind farm. This results in a greater velocity deficit in the wind farm as there is no flow diversion around the edges of the wind farm. A high surface roughness was used for the land. An increase in friction leads to a slower propagation of the sea breeze front, meaning that the sea breeze front remains within the wind farm wake for a longer period of time. Even though these steps were implemented, the effect of WF1 was negligible in the sea breeze part of the cycle.

It should also be noted that these simulations model dry air, with no water vapour emissions from either the sea or the land. Adding extra physics and micro-physics to these simulations set up as they are could lead to extra difficulties in assessing the impact of wind farms on the sea breeze. There is also no mesoscale activity in these simulations. Any such features will further decrease the effect of the wind farms as the wake will not reach a steady state.

The choice of wind farm simulation shows that an idealised sea breeze is not effected by a wind farm position off the coast. This can be attributed to two factors, the first being the velocity in the front not being high enough to have a large wind farm wake, and secondly the turbulence within the front sufficiently mixes the wake deficit. The wind farm simulations directly impact the land breeze front and this gravity current passes through the wind farm. The turbulence within the front is not able to mix the deficits caused by the wind farm, resulting in more noticeable impacts. That said, changes to the land breeze are not significant. The velocity deficits observed in these simulations would be difficult to detect in real observations. Any mesoscale activity is likely to make these deficits obsolete. Furthermore, these simulations are only 2-dimensional, and it is unknown how a 3-dimensional wind farm will interact with a land breeze. The possibility of flow diverting around the wind farm could potentially reduce the height increases of the front.

Chapter 7

Summary and further work

The aim of this study was to improve the understanding around wind farm impacts on the boundary layer. This can be used to assist in making informed choices about the installation of wind farms and to lead into further research involving more complex boundary layer scenarios.

In order to achieve this objective, a suite of numerical simulations have be carried out. This required implementing a WFP parametrisation in BLASIUS based on Katic *et al.* (1986) and Fitch *et al.* (2012). The WFP parametrisation models each turbine as a sink of kinetic energy and a source of TKE. The drag and power coefficients of a turbine are used within the parametrisation. Sensitivity studies were carried out with the WFP in BLASIUS. It was found that grid scale noise occurs when there are grid cells between turbines which do not contain a wind turbine. Modelling a wind farm with the turbine spacing equal to the model grid spacing results is smoother velocity and TKE contours. Vertical resolution has little impact on the flow around the turbines, however lower resolution may produce inaccurate velocity readings near the top of the boundary layer.

BLASIUS simulations were then carried out to assess the impact of a wind farm on a neutral boundary layer. Of interest was to look at the response from the wind farm in different boundary layer conditions. Changes in the boundary layer capping inversion have little effect on the impact from the wind farms, with the only difference being a smaller displacement for stronger inversions. The height of the boundary layer has a significant impact on the flow. This occurs when the boundary layer capping inversion interacts with the wind farm wake, shown

to be between 715 m and 992 m with a turbine hub height of 95 m. Increases in boundary layer velocity increase the wake both upstream and downstream of the wind farm, with an additional increase in vertical transport.

By looking at non-dimensional parameters associated with the boundary layer, it was shown that the vertical velocity within the wind farm increases as Fr increases. When $Fr < 1$, the inclusion of a wind farm causes a sudden decrease in the boundary layer height over the wind farm, resulting in a longer wind farm wake. When there is a stable free atmosphere above the boundary layer, the boundary layer displacements result in upward propagating waves in the air aloft. The parameter Z was used to quantitatively describe the effect that waves in the air aloft have of the flow. Low Z values result in greater pressure perturbations around the wind farm, with the impact from the waves aloft being smaller for stronger boundary layer inversions.

The effect of the wind farms was not confined to the wind farm area, but instead had an impact 50 km away. The signal at these distances is small and would not be picked up in field observations. The addition of mesoscale features would only make the impact smaller far away from the wind farms. Changes in the boundary layer height were also found to be small and it is unknown whether these could be detected. The response on the boundary layer is smaller in magnitude than that caused by a hill.

Another method used in understanding the dynamics of a wind farm in a boundary layer is to use a linear model, as was done by Smith (2010). This linear model assumes a single layer of flow within the boundary layer, which means the wind farm drag is distributed throughout all of the boundary layer. To test this assumption, comparisons were made with similar BLASIUS simulations. It was found that the linear model makes a good representation of the velocity and pressure perturbations in the boundary layer. There were limitations to the linear model. The drag from each turbine is overestimated, and modifications were suggested to improve this. The assumption of drag being distributed through the height of the boundary layer decreases the pressure perturbation in the wind farm, which affects the flow through the wind farm. Smith (2010) suggested that with a strong stability in the air aloft and $Fr \approx 1$, a sudden decrease in velocity can occur within the wind farm. The velocity could then go below the cut-in speed. Simulations in BLASIUS confirmed that this can occur, with less sensitivity to Fr as previously thought.

With a more general understanding of the impact wind farms have on the boundary layer, more realistic situations involving wind farms were then investigated. Sea breeze simulations in WRF were carried out, with varying turbine density wind farms. With a wind farm on the coast, there was little change to the evolution of the sea breeze. This is brought about because the thermal heating over land leads to convective conditions in front of the sea breeze and increases the mixing with the sea breeze front. The wake from the wind farm decays quickly and does not impact the front of the sea breeze. The turbine density did not change the impact on the sea breeze, even though the drag within the wind farm was unrealistically large. At night, the land breeze is affected by the wind farm. The wind farms decrease the velocity of the land breeze and also increase its height. The interaction of a wind farm with a land breeze is analogous to a porous obstacle in a gravity current.

This study has shown that the impact from a wind farm in the boundary layer can be far reaching, however not sufficient enough to have an impact. Additional boundary layer mechanisms, such as surface heating, decay the wind farm wake meaning that wind farms only impact the boundary layer within the wind farm area.

To further improve our understanding of wind farms in the boundary layer it would be of interest to expand the simulations carried out in this study. Including additional boundary layer physics, such as aerosols and thermodynamics, which could lead to noticeable impacts from the wind farm. From the existing literature, it is known that stable boundary layer conditions lead to greater velocity deficits in the wind farm wakes (Abkar & Porte-Agel, 2015). The mixing from a wind farm in a stable boundary layer increases near surface temperature around the wind farm, as shown in Zhou *et al.* (2012) and Smith *et al.* (2013). Further studies using BLASIUS could be conducted to understand the parameters which control the increases in surface temperatures in a stable boundary layer. This could include turbines with different hub height, shallow boundary layers and changes in the boundary layer potential temperature lapse rates. It is unknown if wind farms produce gravity waves, either in a stable boundary layer or on boundary layer capping inversion. It would be of interest to investigate this with higher resolution models.

Based on the work in this thesis, another area which could be expanded further is the interaction between the boundary layer inversion and the wind farm wake. It

was shown in chapter 4 that as the boundary layer height decreased, then the impact from the wind farm wake in the boundary layer increased. The simulations used in this analysis did not cover boundary layers lower than 452 m. This was due to computational difficulties. A study focussing on changes in boundary layer height could provide further information into the critical height where the boundary layer directly interacts with the wind farm wake. Simulations in BLASIUS would be appropriate for this analysis, however the issue with Rayleigh damping in the horizontal direction would need to be addressed. Doing so will prevent the wrap around effects shown in chapter 4. The ability to run RANS simulations comparable to previous LES studies, such as in Lu & Porte-Agel (2015), would be of interest, not only in comparing results with LES but also to look at the wider scale effects of wind farms in the boundary, a result that can not be derived from LES.

The impact of the wind farm on the land breeze implies that a wind farm could affect a sea breeze if positioned on the land. It would of interest to develop this area, using a more realistic sea breeze to understand the wind farm impact. Enhancing the WRF wind farm sea breeze simulations so that tracers can be modelled would also be of interest. It was shown that the wind farms had a small effect on the local boundary, whereas the domain size limited this analysis to the 1 km average. Running RANS at smaller domain sizes than this for wind farm simulations is not recommended, and hence such simulations should use LES. Development of an LES wind farm model with a gravity current would show the impact on atmospheric tracers, which may have wider implications beyond the meteorology.

This study aimed to identify the large scale impacts of wind farms in the boundary layer. This was motivated by the existing gap in the literature where only LES was used to analyse the impact from wind farms in the boundary layer. Studies involving RANS simulations with wind farms were focussed on the effect of the boundary layer on power output, and not the feedback from the wind farms. The ability to run larger domain sizes in BLASIUS and WRF has shown that the effect from wind farms can be observed up to 50 km from the wind farm. This is under idealised conditions with no mesoscale activity. The scenario in which wind farms have the greatest impact on the boundary layer is when the wind farm wake and boundary layer inversion interact. This interaction caused changes in the boundary layer height which propagate the wind farm effect away from the

wind farm. This study has shown that the direct impact from a wind farm in the boundary layer is small. Velocity perturbations from the wind farm wake can be observed in the numerical models 50 km from the wind farm, however the perturbations are on the order of 0.25% from the unperturbed boundary layer velocity. When the wind farm interacts with another boundary layer feature then the effects can be larger and wider reaching. Although the results in Lu & Porte-Agel (2015) showed that there were changes to the boundary layer height when a wind farm was included in the boundary layer, the larger domain used in this work has shown that the effect can be observed at distances larger than can be shown in LES.

The interaction between wind farms and meteorological features was explored further by looking at the effect of wind farms on the sea breeze. The results in this study show that the inclusion of a wind farm in a sea breeze does not change the formation or evolution of the sea breeze front. Even by modelling unrealistic wind farms, the impact on a sea breeze was minimal.

The motivation behind this study was to further understand the impact of wind farms on the boundary layer. The purpose of this was to understand the impact of installing larger wind farm arrays as a method of meeting renewable energy targets. Through the use of numerical models, the effect of wind farms in the boundary layer has been investigated. Although some impacts have been observed, both in the idealised set up and in a sea breeze simulation, the impacts have been small. It is questionable whether the velocity perturbations shown in this study would be observed in field observations over the same distances as modelled in this study.

The dominant effect from a wind farm on the boundary layer is from the wind farm wake. Stable boundary layers, which decrease the decay of the wind farm wake, may lead to greater impacts from wind farms, meaning that the greatest impact from wind farms are likely to occur at night. It is hypothesised that the greatest effect from wind farms will be on the nocturnal boundary layer, where not only will the stable conditions increase the wind farm wake compared to a convective boundary layer, but the increased near surface temperatures, from the turbine mixing, and shallow boundary layer, could increase the effect from the turbines. A shallow nocturnal boundary layer may lead to gravity waves, an effect more likely to occur as the height of turbines increases. Furthermore, the increased surface temperatures near wind farms in stable boundary layers may

also lead to interesting changes in the local meteorology. In addition, it is not known whether these temperature changes will affect the growth of crops near wind farms. This is potentially an area of high impact and is a priority for future research into the effect of wind farms on the boundary layer.

References

Abkar, M. & Porte-Agel, F. (2015). Influence of atmospheric stability on wind turbine wakes: A large eggy simulation study. *Physics of Fluids*, **27**, 035104.

Aitken, M., Banta, R., Pichugina, Y.L. & Lundquist, J.K. (2014). Quantifying wind turbine wake characterisitics from scanning remote sensor data . *Journal of Atmospheric and Oceanic Technology*, **31**, 765–787.

Allaerts, D. & Meyers, J. (2015). Large eddy simulation of a large wind turbine array in a conventionally neutral atmospheric boundary layer. *Physics of Fluids*, **27**, 065108.

Arwas, P., Charlesworth, D., Clark, D., Clay, R., Craft, G., Donaldson, I., Dunlop, A., Fox, A., Howard, R., Lloyd, C., Lovett, C., Marshall, A. & Wiles, F. (2012). *Offshore wind cost reduction pacthways study*. [Online] The Crown Estate, Available from: www.thecrownestate.co.uk/media/5493/ei-offshore-wind-cost-reduction-pathways-study.pdf.

Baidya Roy, S. (2011). Simulating impacts of wind farms on local hydrometeorology. *Journal of Wind Engineering and Industrial Aerodynamics*, **99**, 491–498.

Baidya Roy, S. & Traiteur, J.J. (2010). Impacts of wind farms on surface air temperatures. *Proceedings of the National Academy of Sciences of the United States of America*, **107**, 17899–17904.

Baidya Roy, S., Pacala, S.W. & Walko, R.L. (2004). Can large wind farms affect local meteorology? *Journal of Geophysical Research: Atmospheres*, **109**, d19101.

Barthelmie, R.J., Hansen, K.S. & Pryor, S.C. (2013). Meteorological Controls on Wind Turbine Wakes. *Proceedings of the IEEE*, **101**, 1010–1019.

Barthemlie, R. & Jensen, L.E. (2010). Evaluation of wind farm efficiency and wind turbine wakes and the nysted offshore wind farm. *Wind Energy*, **13**, 573 –585.

Calaf, M., Meneveau, C. & Meyers, J. (2010). Large eddy simulation study of fully developed wind-turbine array boundary layers. *Physics of Fluids*, **22**, 015110.

Calaf, M., Parlange, M.B. & Meneveau, C. (2011). Large eddy simulation study of scalar transport in fully developed wind turbine array boundary layers. *Physics of Fuids*, **23**, 126603.

Calaf, M., Higgins, C. & Parlange, M.B. (2014). Large wind farms and the scaler flux over an heterogeneously rough land surface. *Boundary Layer Meteorology*, **153**, 471–495.

Cervarich, M.C., Roy, S.B. & Zhou, L. (2013). Spatiotemporal Structure of Wind Farm-atmospheric Boundary Layer Interactions. *Energy Procedia*, **40**, 530–536.

Chamorro, L. & Porte-Agel, F. (2010). Effects of thermal stability and incoming boundary layer flow characteristics on wind turbine wakes: A wind tunnel study. *Boundary Layer Meteorology*, **136**, 515–533.

Chamorro, L.P. & Porté-Agel, F. (2009). A Wind-Tunnel Investigation of Wind-Turbine Wakes: Boundary-Layer Turbulence Effects. *Boundary-Layer Meteorology*, **132**, 129–149.

Chamorro, L.P. & Porté-Agel, F. (2011). Turbulent Flow Inside and Above a Wind Farm: A Wind-Tunnel Study. *Energies*, **4**, 1916–1936.

Chamorro, L.P., Arndt, R.E.a. & Sotiropoulos, F. (2011). Turbulent Flow Properties Around a Staggered Wind Farm. *Boundary-Layer Meteorology*, **141**, 349–367.

Chamorro, L.P., Arndt, R.E.A. & Sotiropoulos, F. (2012). Reynolds number dependence of turbulence statistics in the wake of wind turbines. *wind Energy*, **15**, 733=742.

Christiansen, M.B. & Hasager, C.B. (2005). Wake effects of large offshore wind farms identified from satellite SAR. *Remote Sensing of Environment*, **98**, 251–268.

COMM (2017). Renewable energy progress report. *European Commissions*, **57**, final.

Corbetta, G., A.Ho & Pineda, I. (2015). *Wind energy scenarios for 2030*. European Wind Energy Association.

Crespo, A., Hernandez, J., Fraga, E. & Andreu, C. (1988). Experimental validation of the upm computer code to calculate wind turbine wakes and comparison with other models. *Journal of Wind Engineering and Industrial Aerodynamics*, **27**, 77–88.

Csanady, G.T. (1974). Equilibrium theory of the planetary boundary layer with an inversion lid. *Boundary Layer Meteorology*, **6**, 63–79.

Emeis, S. (2010). Meteorlogical explanation of wake clouds at Horns Rev wind farm. *DEWI Magazin*, **37**, 52–55.

Fiedler, B.H. & Bukovsky, M.S. (2011). The effect of a giant wind farm on precipitation in a regional climate model. *Environmental Research Letters*, **6**, 045101.

Fitch, A.C., Olson, J.B., Lundquist, J.K., Dudhia, J., Gupta, A.K., Michalakes, J. & Barstad, I. (2012). Local and Mesoscale Impacts of Wind Farms as Parameterized in a Mesoscale NWP Model. *Monthly Weather Review*, **140**, 3017–3038.

Fitch, A.C., Lundquist, J.K. & Olson, J.B. (2013). Mesoscale Influences of Wind Farms throughout a Diurnal Cycle. *Monthly Weather Review*, **141**, 2173–2198.

Frandsen, S. (2007). On the wind speed reduction in the centre of large clusters of wind turbines. *Journal of Wind Engineering and Industrial Aerodynamics*, **39**, 251–265.

Hess, G.D. (2004). The neutral, barotropic planetary boundary layer, capped by a low-level inversion. *Boundary Layer Meteorology*, **110**, 319–355.

Iungo, G.V., Wu, Y.T. & Porté-Agel, F. (2013). Field Measurements of Wind Turbine Wakes with Lidars. *Journal of Atmospheric and Oceanic Technology*, **30**, 274–287.

Katic, I., Hojstrup, J. & Jensen, N. (1986). A simple model for cluster efficiency. In *Proceedings from the European Wind Energy Association Conference*, 407–410, Rome.

Lu, H. & Porte-Agel, F. (2015). On the impact of wind farms on a convective atmospheric boundary layer. *Boundary Layer Meteorology*, **157**, 81–96.

Lu, H. & Porte-Agel, F. (2011). Large-eddy simulation of a very large wind farm in a stable atmospheric boundary layer. *Physics of Fluids*, **23**, 065101.

Machefaux, E., Larsen, G.C., Koblitz, T., Troldborg, N., Kelly, M.C., Chougule, A., Hansen, K.S. & Rodrigo, J.S. (2015). An experimental and numerical study of the atmospheric stability impact on wind turbine wakes. *Wind Energy*.

Markfort, C.D., Zhang, W. & Porte-Agel, F. (2012). Turbulent flow and scalar transport thrpough an over aligned and staggered wind farms. *Journal of Turbulence*, **13**.

Miawer, E.J., Taubman, S.J., Brown, P., Iacono, M.J. & Clough, S.A. (1997). Radiative transfer for inhomogeneous atmosphere: RRTM, a validated correlated k-model for longwave. *J. Geophys. Res.*, **102**, 16663 – 16682.

Öko-Institut (2017). *Study on Technical Assistance in Realisation of the 2016 Report on Renewable Energy, in preparation of the Renewable Energy Package for the Period 2020-2030 in the European Union*. European Commission DG Energy.

Rajewski, D.A., Takle, E.S., Lundquist, J.K., Prueger, J.H., Pfeiffer, R.L., Hatfield, J.L., Spoth, K.K. & Doorenbos, R.K. (2014). Changes in fluxes of heat, h2o, and co2 caused by a large wind farm. *Agricultural and Forest Meteorology*, **194**, 175 – 187.

Ross, A.N. & Vosper, S.B. (2005). Neutral turbulent flow over forested hills. *Quarterly Journal of the Royal Meteorological Society*, **131**, 1841–1862.

Sanderse, B., van der Pijl, S. & Koren, B. (2011). Review of computational fluid dynamics for wind turbine wake aerodynamics. *Wind Energy*, **14**, 799–819.

Simpson, J.E. (1987). *Gravity Currents in the Environment and the Laboratory*. University Press, Cambridge, United Kingdon, second edition edn.

Simpson, J.E. (1994). *Sea Breeze and Local Winds*. University Press, Cambridge, United Kingdon.

Skamarock, W., Klemp, J., Dudhia, J., Gill, D., Barker, D., Duda, M., Huand, X., Wang, W. & Powers, J. (2008). A description of the Advanced Research WRF Version 3. *NCAR Tech. Note*, **NCAR/TN-475+STR**, 125 pp.

Smalikho, I.N., Banakh, V.V., Pichugina, Y.L., Brewer, W.A., Banta, R.M., Lundquist, J.K. & Kelley, N.D. (2013). Lidar Investigation of Atmosphere Effect on a Wind Turbine Wake. *Journal of Atmospheric and Oceanic Technology*, **30**, 2554–2570.

Smith, C.M., Barthelmie, R.J. & Pryor, S.C. (2013). In situ observations of the influence of a large onshore wind farm on near-surface temperature, turbulence intensity and wind speed profiles. *Environmental Research Letters*, **8**, 034006.

Smith, R.B. (2010). Gravity wave effects on wind farm effi ciency . *Wind Energy*, **13**, 449–458.

Steele, C., Dorling, S., Von Glasow, R. & Bacon, J. (2013). Idealized wrf model sensitivity simulations of sea breeze types and their effects on offshore windfields. *Atmospheric Chemistry and Physics*, **13**, 443 – 461.

Stull, R.B. (1988). *An Introduction to Boundary Layer Meteorology*. Kluwer Academic Publishers, 4th edn.

Suyker, A.E., Verma, S.B., Burba, G.G., Arkebauer, T.J., Walters, D.T. & Hubbard, K.G. (2004). Growing season carbon dioxide exchange in irrigated and rain fed maize. *Agric. For. Meteorol.*, **124**, 1–13.

The European Wind Energy Association (2014). Wind in Power 2013 European Statistics [Leaflet]. Brussels, EWEA.

Vanderwende, B. & Lundquist, J.K. (2016). Could crop height affect the wind resource at agriculturally productive wind farm sites. *Boundary Layer Meteorology*, **158**, 409–428.

Vautard, R., Thais, F., Tobin, I., Bréon, F.M., de Lavergne, J.G.D., Colette, A., Yiou, P. & Ruti, P.M. (2014). Regional climate model simulations indicate limited climatic impacts by operational and planned European wind farms. *Nature communications*, **5**, 3196.

Vosper, S.B. (2004). Inversion effects on mountain lee waves. *Q.J.R Meteorol. Soc.*, **130**, 1723–1748.

Wagner, R., Pedersen, T.F., Courtney, M., Antoniou, I., Davoust, S. & Rivera, R.L. (2014). Power curve measurements and nacelle mounted lidar. *wind Energy*, **17**, 1441 – 1453.

Wang, H. & Barthelmie, R.J. (2015). Wind turbine wake detection with a single doppler wind lidar. *Journal of Physics: Conference Series*, **625**.

Wood, N. (1995). The onset of separation in neutral, turbulent flow over hills. *Boundary-Layer Meteorology*, **76**, 137–164.

Wood, N. & Mason, P. (1993). The pressure force induced by neutral, turbulent flow over hills. *Quarterly Journal of the Royal Meteorological Society*, **119**, 1233–1267.

Wu, Y.T. & Porte-Agel, F. (2011). Large-eddy simulation of wind turbine wakes: Evaluation of turbine parametrisations. *Boundary Layer Meteorology*, **138**, 345–366.

Wu, Y.T. & Porté-Agel, F. (2012). Atmospheric Turbulence Effects on Wind-Turbine Wakes: An LES Study. *Energies*, **5**, 5340–5362.

Yang, X., Howard, K.B., Guala, M. & Sotiropoulos, F. (2015). Effects of a three-dimensional hill on the wake characteristics of a model wind turbines. *Physics of Fluids*, **27**, 025103.

Zhang, W., Markfort, C.D. & Porté-Agel, F. (2012). Wind-Turbine Wakes in a Convective Boundary Layer: A Wind-Tunnel Study. *Boundary-Layer Meteorology*, **146**, 161–179.

Zhang, W., Markfort, C.D. & Porté-Agel, F. (2013). Experimental study of the impact of large-scale wind farms on landatmosphere exchanges. *Environmental Research Letters*, **8**, 015002.

Zhou, L., Tian, Y., Baidya Roy, S., Thorncroft, C., Bosart, L.F. & Hu, Y. (2012). Impacts of wind farms on land surface temperature. *Nature Climate Change*, **2**, 539–543.